Design of Supported Metal Catalysts for Aqueous-Phase Conversion of Biomass-Derived Oxygenates

By

Jechan Lee

A dissertation submitted in partial fulfillment of

the requirements for the degree of

Doctor of Philosophy

(Chemical Engineering)

at the

UNIVERSITY OF WISCONSIN-MADISON

2015

Date of final oral examination: January 23, 2015

The dissertation is approved by the following members of the Final Oral Committee:

George W. Huber, Professor, Chemical and Biological Engineering
James A. Dumesic, Professor, Chemical and Biological Engineering
Thomas F. Kuech, Professor, Chemical and Biological Engineering
Manos Mavrikakis, Professor, Chemical and Biological Engineering
Ive Hermans, Associate Professor, Chemistry

Design of Supported Metal Catalysts for Aqueous-Phase Conversion of Biomass-Derived Oxygenates

Jechan Lee

Under the supervision of Prof. George W. Huber

at the University of Wisconsin-Madison

Increases in the cost of fossil fuels along with growing concerns for greenhouse gas emissions are prompting the search for renewable sources of liquid fuel and chemicals. Biomass has been considered as the only realistic and sustainable source of renewable organic carbon for the foreseeable future. Heterogeneous catalysis has played an important role in the development of efficient chemical processes to convert biomass to fuels and chemicals. In this respect, the design of inexpensive active and stable heterogeneous catalysts is important to develop new and improved processes for the conversion of biomass.

This dissertation focuses on aqueous-phase hydrodeoxygenation (APHDO) and aqueous-phase hydrogenation (APH) as model reactions to design improved supported metal catalysts for the conversion of biomass-derived feedstocks. Both APHDO and APH are crucial in converting biomass-derived compounds into liquid fuels and chemicals.

In this dissertation, the activity of a number of monometallic and bimetallic catalysts is compared for APH of carbonyl compounds which is an important reaction in APHDO. Bimetallic Pd-Fe is the most active catalyst among the tested catalysts for APH of C=O and C=C bonds. APHDO of sorbitol was performed with the bimetallic Pd-Fe supported on zirconium phosphate

(Zr-P). Zr-P was chosen as the support due to its high Brønsted to Lewis acid ratio and stability in the aqueous phase. The Pd_1Fe_3/Zr-P catalyst is up to 14 times more active than monometallic Pd/Zr-P and Pt/Zr-P catalysts. Moreover, the Pd_1Fe_3/Zr-P catalyst produces more C4-C6 products by promoting the conversion of sorbitan and isosorbide and more C1-C3 products by promoting C-C bond cleavage (dehydrogenation/retro-aldol condensation) of sorbitol.

Another critical issue of designing heterogeneous catalysts for aqueous-phase reactions is stability of the catalysts. A method for stabilizing base-metal particles of a Co/TiO_2 catalyst is developed using atomic layer deposition (ALD) of TiO_2 film onto the surface of the Co/TiO_2 catalyst. The ALD TiO_2 coated Co/TiO_2 catalyst was tested for APH reactions in a continuous flow reactor and characterized using chemisorption, surface area analysis, electron microscopy, X-ray diffraction, and small-angle X-ray scattering. Through these techniques, it is shown that the ALD TiO_2 coating protects the cobalt particles against leaching and sintering under aqueous conditions.

High-temperature treatments of a Co/TiO_2 catalyst cause migration of partially reduced TiO_2 onto cobalt particles caused by strong metal-support interaction (SMSI) between cobalt and TiO_2. The SMSI effect in the Co/TiO_2 catalyst is elucidated using *in situ* Raman spectroscopy and electron microscopy. By the SMSI effect, cobalt particles of the Co/TiO_2 catalyst are decorated by TiO_x ($x < 2$) species. The TiO_x decoration stabilizes the cobalt particles in a similar way to ALD TiO_2 overcoating. The SMSI effect also creates a bifunctional catalytic site in the Co/TiO_2 which facilitates a furanyl ring-opening reaction. The high-temperature treated Co/TiO_2 catalyst had > 95 % yield for APH of carbonyl compounds to their corresponding alcohols. The two methods for stabilizing cobalt catalysts introduced in this dissertation, ALD and SMSI, may enable the

replacement of expensive novel-metal catalysts with inexpensive base-metal catalysts for aqueous-phase conversion of biomass-derived feedstocks.

ACKNOWLEDGEMENTS

I would like to begin by thanking my parents. Thank you so much for giving birth to me. Mom, without your love and support, it would not have been possible for me to complete my graduate studies. Special thanks to all my family in South Korea for all their love and support.

I am deeply indebted to my advisor, Prof. George W. Huber, for his guidance and mentoring throughout all the years. Thank him for choosing me as one of your students! He has motivated me to learn something new every day. I truly appreciate all of his help and care during my graduate life.

I also thank the current and former Huber group members, especially Pranav U. Karanjkar, Insoo Ro, Joseph P. Chada, Daniel McClelland, and Kevin J. Barnett, for all of the assistance and friendship you have given me. It was a great pleasure working alongside such a great group of people day in and day out. I would also like to thank Dr. Ronen Weingarten, Dr. Christopher J. Gilbert, Dr. Aniruddha A. Upadhye, Dr. Hyung Ju Kim, and Dr. Yong Tae Kim for all their help with moving to Madison and setting up the labs in Madison.

Additionally, I am greatly indebted to the members of my thesis committee, Prof. James A. Dumesic, Prof. Thomas F. Kuech, Prof. Manos Mavrikakis, and Prof. Ive Hermans, for their guidance and suggestions in completing my degree. Special thanks to Prof. James A. Dumesic, Prof. Thomas F. Kuech, and Prof. Ive Hermans with whom I was able to collaborate before graduating.

Finally, I would like to thank all the collaborators who made this research possible. They include Prof. Ye Xu, Dr. Hyung Ju Kim, Dr. Yong Tae Kim, Dr. Sara K. Green, Prof. Won Bae Kim, Dr. Brain M. Moreno, Prof. Michael T. Klein, David H. K. Jackson, Dr. Ana C. Alba-Rubio, Dr. Brandon J. O'Neill, Dr. Carlos A. Carrero, and Samuel P. Burt.

The research project presented in Chapter 3 of this dissertation was supported as part of the Catalysis Center for Energy Innovation, an Energy Frontier Research Center funded by the U.S. Department of Energy, Office of Science, Office of Basic Energy Sciences under Award Number DE-SC0001004. The research projects presented in Chapters 4 to 6 of this dissertation were supported as part of the Institute for Atom-efficient Chemical Transformations (IACT), an Energy Frontier Research Center funded by the U.S. Department of Energy, Office of Basic Energy Sciences. I gratefully acknowledge financial support from these funding sources.

TABLE OF CONTENTS

Page

LIST OF TABLES

Page

LIST OF FIGURES

Page

LIST OF SCHEMES

Page

CHAPTER 1

Introduction

Fossil fuels such as crude oil are today's primary energy sources. The worldwide reserves of crude oil is estimated to only last 20 to 80 years.[1] The decrease in fossil fuel reserves along with increasing the cost of petroleum and growing concerns for greenhouse gas emissions has accelerated research on renewable resources of clean energy.

Biomass has received considerable attention as a sustainable alternative for the production of fuels and chemicals.[2-11] Biomass consists of three main polymeric components: Cellulose, hemicellulose, and lignin.[12] Cellulose and hemicellulose are able to be hydrolyzed to their corresponding sugar monomers.[13] Cellulose is mainly composed of glucose (six-carbon sugar), and xylose (five-carbon sugar) is the main building block of hemicellulose. Lignin is a highly polymeric complex containing a large variety of functional groups including phenolic groups. In contrast to other renewable energies, biomass is the only practical renewable source of organic carbon which can be used for the production of liquid hydrocarbon fuels and value-added chemicals.[14-16] For example, biofuels derived from biomass are sustainable resources of liquid fuels.[17]

Heterogeneous catalysis has long contributed to improved processes to produce a wide range of fuels and chemicals from conventional resources (*e.g.*, petroleum and natural gas). A few examples of the contributions include Fischer-Tropsch synthesis to convert carbon monoxide and hydrogen into liquid hydrocarbons using cobalt-based catalysts,[18] fluidized catalytic cracking (FCC) using zeolite to produce petroleum-based products such as gasoline,[19] and synthesis gas production via methane reforming reactions over metal catalysts.[20-22]

Even though heterogeneous catalysis has played a central role in chemical and petrochemical fields, processing of petroleum-based feedstocks differs from processing of biomass-derived feedstocks. Biomass-derived feedstocks have low thermal stability and a high

degree of functionality.[4] Therefore, processing of biomass-derived feedstocks requires unique reaction conditions such as aqueous-phase conditions.[4] In these respects, development of new and improved heterogeneous catalysts is required to make the biomass conversion processes economically viable.

Catalytic aqueous-phase processes are a promising route for the transformation of biomass-derived feedstocks into liquid fuels and chemicals. The processes occur in liquid phase, thereby eliminating the need to vaporize the aqueous feedstocks and improving the overall thermal efficiency of the processes. Hydrogen has been produced via aqueous-phase reforming (APR) of biomass-derived oxygenated hydrocarbons such as ethylene glycol, glycerol, and sorbitol over different monometallic and bimetallic catalysts.[23-28] Aqueous-phase conversion of carbohydrates has been primarily carried out with precious metal catalysts. Dumesic and co-workers produced alkanes from aqueous-phase conversion of carbohydrates using Pt catalysts.[29, 30] Alkanes can also be prepared from cellulose using Ir-Re and Ru catalysts.[31, 32] Ru and Pt catalysts have been used for aqueous-phase hydrogenation of carbohydrates and organic acids.[33-35] Mono-functional organic compounds can be prepared from sugar alcohols using Pt-Re catalysts.[36, 37]

In the aqueous-phase processes, aqueous-phase hydrodeoxygenation (APHDO) is a promising approach to selectively remove oxygen from biomass-derived feedstocks for production of renewable alkanes, alcohols, and polyols.[29] APHDO can be used to process a range of different biomass-derived feedstocks including aqueous carbohydrates,[29, 38, 39] pyrolysis oil,[40] carbohydrates derived from hydrolysis of biomass,[41] and fermentation products. APHDO could also be used for upgrading bio-oil.[42]

Aqueous-phase hydrogenation (APH) is an important fundamental reaction in APHDO, involving hydrogenation of a range of functional groups of biomass-derived feedstocks.[29, 38, 43-45]

Upgrading bio-oil by hydrotreating also involves hydrogenation of a variety of functionalities.[46] Hydrogenation of organic acids is one of the slowest steps in hydrotreating bio-oil.[47]

Figure 1.1 shows a conceptual process for APH and APHDO of biomass-derived feedstocks. In the Reactor 1, carbohydrates, which can be produced through hydrolysis of cellulose,[41] are reacted with hydrogen to produce corresponding sugar alcohols.[33, 48, 49] For example, Gallezot *et al.* achieved 100 % conversion and 99.2 % sorbitol selectivity for glucose hydrogenation over carbon-supported Ru catalyst at 373 K.[33] Hoffer *et al.* also produced sorbitol from glucose with more than 98 % selectivity using Ru/C catalysts at 393 K.[48] The authors also concluded that Ru/C catalysts are better than Raney Ni catalysts for glucose hydrogenation because the Raney Ni catalysts deactivate due to leaching of Ni.[48]

The outlet stream from the Reactor 1 is fed into the Reactor 2 containing a bifunctional catalyst. The outlet stream from the Reactor 2 is sent to a separation system. The separation system separates the gas phase, the liquid phase, and an aqueous stream. The gasoline-range products in the liquid phase can be blended with a petroleum-based feedstock. A part of the gas phase (*e.g.*, hydrogen) is recompressed and fed back into the Reactor 1. Another part of the gaseous stream (*e.g.*, methane) can be combusted to provide process heat or reformed to produce hydrogen. The aqueous stream (*e.g.*, unreacted feedstock) can be recycled back into the Reactor 2 or purged into a waste-water treatment facility.

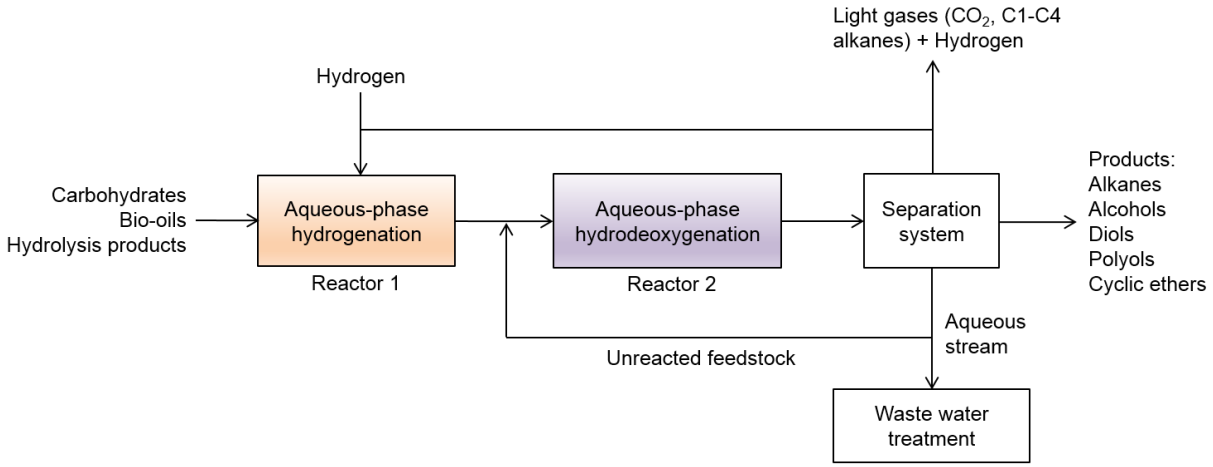

Figure 1.1 Block flow diagram for a conceptual APH and APHDO process. Figure adapted from the reference.[39]

APHDO involves different reactions such as C-C cleavage reactions (*e.g.*, decarbonylation and retro-aldol condensation) along with hydrogenation, dehydrogenation, and water-gas shift reactions and C-O cleavage reactions (*e.g.*, dehydration/hydrogenation).[38] These reactions occur simultaneously or successively, leading to a complex mixture of reactants, products, and intermediates.[50] In the case of APHDO of sorbitol, for example, more than 50 products were identified.[38, 39, 51, 52] Also, according to a reaction network model generated through INGen (Interactive Network Generator), APHDO of sorbitol involves 4804 irreversible reactions.[53] This complicated set of reactions in APHDO makes designing active and selective catalysts hard. The stability of the catalytic materials for APHDO is one of the biggest challenges is in the harsh aqueous-phase conditions.

This dissertation attempts to address some of the challenges highlighted above by experimental approaches to design new classes of supported metal catalyst. The approaches use catalyst characterization techniques, high-throughput screening of a number of catalysts for model APH reactions, and test and evaluation of the screened catalysts in a continuous flow reactor for a

more complicated APHDO reaction. Figure 1.2 shows elements of the supported metal catalysts tested in this dissertation.

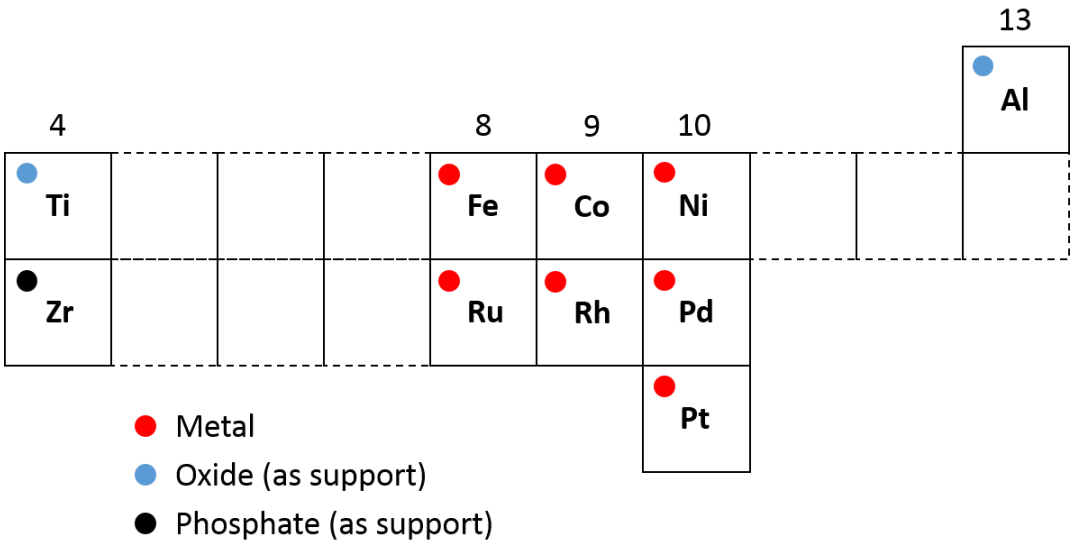

Figure 1.2 Overview of elements tested as supported metal catalysts in this dissertation.

There are important achievements in this dissertation. First, an active bimetallic Pd-Fe catalyst is designed for APH of carbonyl compounds and APHDO of sorbitol. Second, stable cobalt catalysts are designed using atomic layer deposition (ALD) and strong metal-support interaction (SMSI). Cobalt is orders of magnitude less expensive than precious metals such as Pt and Pd.[54] The cobalt particles are covered by an ALD TiO_2 film (ALD approach) or a layer of partially reduced TiO_2 (SMSI approach), thereby stabilizing against irreversible deactivation such as leaching and sintering in the aqueous phase. Finally, a stable cobalt catalyst prepared using the SMSI effect selectively cleaves C-O-C bond in furan ring. Also, the cobalt catalyst has near 100 % yield for APH of carbonyl compounds.

Chapters 3 and 4 introduce systematic studies of a number of monometallic and bimetallic catalysts for APH of different functional groups which is important reactions in APHDO of

sorbitol. The most active catalyst was then tested for the APHDO of sorbitol in a continuous flow reactor, which is more realistic system for biomass conversion.

Chapter 5 describes the use of ALD stabilizing a classic cobalt catalyst. The application of an ALD TiO_2 coating onto the surface of the cobalt catalyst eliminates leaching and sintering of cobalt during APH reactions. Chemisorption, physisorption, X-ray diffraction, electron microscopy, and small-angle X-ray scattering are used to characterize the ALD coated cobalt catalyst.

In Chapter 6, the role of high-temperature treatments of a conventional titanium dioxide supported cobalt catalyst in the catalyst stability will be discussed. The high-temperature treatments cause migration of partially reduced TiO_2 onto cobalt particles by SMSI effect. The SMSI effect is investigated by utilizing chemisorption, physisorption, electron microscopy, and *in situ* Raman spectroscopy. The SMSI effect creates bifunctionality which facilitates selective C-O-C bond cleavage in furan ring. The SMSI cobalt catalyst also selective for hydrogenation of C=O bond to C-OH bond.

The overall results from this dissertation will be used to design more effective catalysts for the conversion of biomass-derived compounds in the future that will ultimately allow us to use our biomass resources more economically.

CHAPTER 2

Experimental Techniques

2.1 Catalyst Preparation

2.1.1 Gamma-alumina (γ-Al_2O_3) supported metal catalysts

A γ-Al_2O_3 (surface area = 142 m^2 g^{-1}) was formed by calcination of Boehmite (Catapal® A Alumina, Sasol North America Inc.) at 873 K (20 K min^{-1}) for 4 hours in static air. A 5 wt% Rh/Al_2O_3 catalyst was purchased from Strem Chemicals. Monometallic Pd, Pt, Ru, Ni, and Co catalysts having different metal loadings were prepared by incipient wetness impregnation with solutions of the following metal precursors.

Noble metals: Pd (tetraamine palldium (II) nitrate), Pt (tetraamine platinum (II) nitrate), and Ru (ruthenium (III) nitrosyl nitrate)

Base metals: Ni (nickel (II) nitrate hexahydrate), Co (cobalt (II) nitrate hexahydrate), and Fe (Iron (III) nitrate nonahydrate)

Multiple impregnations were required for some catalysts to achieve the desired metal loading. After the impregnation, the metal salt solution-support mixture was dried at 373 K for 12 hours. The dried Pd and Pt catalysts were calcined at 523 K (20 K min^{-1}) for 4 hours in static air. The dried Ru catalysts were not calcined to avoid the loss of Ru species from volatilization of Ru oxides. The dried Ni and Co catalysts were calcined at 823 K (20 K min^{-1}) for 4 hours in static air.

To prepare bimetallic catalysts, the base metal precursors above were added to the prepared 3 wt% Pd/γ-Al_2O_3, Ru/γ-Al_2O_3, and Pt/γ-Al_2O_3 catalysts by incipient wetness impregnation at a noble metal to base metal molar ratio of (1:3) and (1:1). Multiple impregnations were required for some catalysts to achieve the desired loading of the second metal. After incipient wetness impregnation, the base metal salt solution-noble metal catalyst mixture was dried at 373 K for 12 hours. Pd- and Pt-bimetallic catalysts were then calcined at 523 K (20 K min^{-1}) for 4 hours in static air.

2.1.2 Zirconium phosphate (Zr-P) supported metal catalysts

A Zr-P (surface area = 361 m^2 g^{-1}) was prepared by co-precipitation using 1.0 mol L^{-1} aqueous solutions of $ZrOCl_2$ $8H_2O$ and $NH_4H_2PO_4$ at a molar ratio of P/Zr = 2, as described by Kamiya *et al.*[55] The precipitate was aged at room temperature for 30 minutes, filtered, washed with deionized water until the pH was 5, dried at 373 K for 12 hours, and then calcined at 673 K (20 K min^{-1}) for 4 hours in static air. A 3 wt% Pd/Zr-P catalyst was prepared by incipient wetness impregnation with an aqueous solution of $Pd(NH_3)_4(NO_3)_2$. The Pd/Zr-P catalyst was calcined at 523 K (20 K min^{-1}) for 3 hours in static air. A Pd-Fe/Zr-P bimetallic catalyst with a Fe to Pd molar ratio of 3:1 (Pd_1Fe_3/Zr-P) was prepared by sequentially impregnating the 3 wt% Pd/Zr-P catalyst dried at 373 K with an aqueous solution of $Fe(NO_3)_3$ $9H_2O$. The Pd-Fe/Zr-P catalyst was calcined at 523 K (20 K min^{-1}) for 3 hours in static air.

2.1.3 Titania (TiO_2) supported cobalt catalyst

A commercial P25 TiO_2 purchased from Aldrich (surface area = 51 m^2 g^{-1}) was calcined at 1023 K (4 K min^{-1}) for 4 hours. The calcined TiO_2 (surface area = 10.2 m^2 g^{-1}) was used as the support. An aqueous solution of $Co(NO_3)_2$ $6H_2O$ was added to the TiO_2 support using incipient wetness impregnation to prepare a 5 wt% Co/TiO_2 catalyst. After impregnation, the catalyst was dried at 373 K for 12 hours. The prepared Co/TiO_2 catalyst was calcined at 573 K (1 K min^{-1}) for 2 hour in static air.

2.1.4 Atomic layer deposition (ALD)

ALD TiO_2 films were deposited in a fluidized bed reactor described elsewhere.[56] Argon was used as a carrier gas at a flow of 30 sccm, with the reactor pressure varying between 5.3 ± 0.5 Torr during depositions. An ALD precursor, $TiCl_4$, was held in a cylinder at room temperature and fed through a metering valve to give a partial pressure of ~0.8 Torr. DI water was held in a cooling bath at 285 K. The TiO_2 depositions were performed at the reactor temperature of 423 K, using 30 cycles consisting of the pulse sequence of $TiCl_4$ – Purge – H_2O – Purge. Purges were fixed at 10 minutes, and pulse lengths were determined by using a quadrupole mass spectrometer monitoring reaction byproducts in the reactor effluent. A typical deposition used about 1 g of catalyst (*i.e.*, Co/TiO_2) as a substrate.

2.2 Catalyst Characterization

2.2.1 Hydrogen chemisorption

To obtain hydrogen uptake of the catalysts, static hydrogen chemisorption was carried out using a Quantachrome Autosorb iQ Automated Gas Sorption system (Chapters 3 and 4) or a Micromeritics ASAP 2020 (Chapters 5 and 6). Prior to hydrogen chemisorption, samples were reduced *in situ* under hydrogen flow at 573 K (1 K min^{-1}) for noble meal catalysts and bimetallic catalysts and at 723 K (1 K min^{-1}) for base metal catalysts for 2 hours. After reduction, the catalysts were purged with helium for 2 hours, evacuated for 140 minutes, and cooled down to room temperature. Hydrogen was dosed on the catalyst until the equilibrium pressure was 560 mmHg. The hydrogen in the cell was then evacuated at room temperature, and again hydrogen was dosed on the catalyst to determine the amount of weakly adsorbed hydrogen. The amount of strongly adsorbed hydrogen was determined by subtracting the second isotherm from the first one.

2.2.2 Carbon monoxide (CO) chemisorption

Pulse CO chemisorption was conducted in a Micromeritics AutoChem II 2920 unit equipped with a thermal conductivity detector (TCD) to measure the consumption of CO. Prior to CO chemisorption, samples were reduced *in situ* under hydrogen flow at 573 K (1 K min^{-1}) for noble meal catalysts and bimetallic catalysts and at 723 K (1 K min^{-1}) for base metal catalysts for 2 hours, and cooled down to room temperature. The chemisorption was carried out at 300 K in a 50 mL min^{-1} stream of helium using a pulse chemisorption technique, in which 500 mL pulses of 10 % CO/helium were utilized.

2.2.3 Temperature-programmed reduction (TPR)

TPR was performed using a Micromeritics AutoChem II 2920 unit. Prior to TPR, samples were pretreated in helium at 423 K for 30 minutes. A TPR run was carried out in a flow of 10 % hydrogen/argon mixture gas at a flow rate of 50 mL min^{-1} with a temperature ramp of 10 K min^{-1}. A dry ice/acetone cooling bath removed moisture from the TPR effluent stream at 195 K before the stream entering a TCD. The consumption of hydrogen was monitored using the TCD and quantified based on hydrogen consumption of an AgO TPR standard (Micromeritics).

2.2.4 Brunauer-Emmett-Teller (BET) surface area

BET surface area of catalysts was measured from nitrogen adsorption data at 77 K obtained using a Micromeritics ASAP 2020 system. Prior to BET analysis, samples were degassed under vacuum at 523 K.

2.2.5 X-ray diffraction (XRD)

In Chapter 4, the bulk crystalline structure of the Pd/Zr-P and Pd-Fe/Zr-P catalysts was determined by XRD. XRD patterns were obtained with a Scintag Pad V using Cu Ka radiation (k = 0.15406 nm), operated at 45 kV and 40 mA (2.0 kW) at a scan rate of 0.2° (2θ) s^{-1}. Each sample was reduced at 573 K for 2 hours in hydrogen and passivated prior to XRD experiments. The assignment of the crystalline phases was carried out using JADE 9.0 software package (Rigaku) for the ICDD database. In Chapter 5, XRD was performed by synchrotron radiation at Argonne National Laboratory on the Advanced Photon Source (APS), beamline 11-BM using a 12-analyzer Si detector with X-ray energy of 30 keV. In Chapter 6, XRD patterns were obtained using a Rigaku D/Max Rapid II diffractometer with a Mo K_α source in the scan range from 0 to 45 °at a scan rate of 0.02 °min^{-1}. Peak identification was carried out using Jade 9.0 software. Prior to XRD, the samples were passivated in 10 % oxygen after reduction.

2.2.6 Inductively coupled plasma atomic emission spectroscopy (ICP-AES)

ICP-AES analysis was performed using a Perkin-Elmer Plasma 400 ICP Emission Spectrometer. Cobalt standards for the ICP-AES analysis were prepared from a cobalt ICP standard (Fluka, 1000 ± 2 mg L^{-1}). In Chapter 5, the amount of cobalt in liquid samples collected during reactions were analyzed. Samples were prepared by being dissolved in 10 % hydrochloric acid (Fisher). In Chapter 6, the cobalt loading of catalysts before and after reaction was analyzed. A catalyst (10 mg) was digested with a mixture of 1 mL nitric acid (Fisher, 69.2 wt%), 3 mL hydrochloric acid (Fisher, 37.4 wt%), and 5 mL hydrofluoric acid (Acros Organics, 48-51 %) in a Teflon beaker at 383 K for 24 hours.

2.2.7 Transmission electron microscopy (TEM)

TEM was perfumed to obtain particle size distribution of cobalt catalysts. In Chapter 5, a Tecnai TF-30 transmission electron microscope operated at 300 keV was used for TEM imaging. The as-deposited and annealed samples were suspended in analytical grade methanol and then collected on a 300 mesh carbon holey support film. In Chapter 6, a Tecnai T12 TEM at 120 kV was used for TEM imaging. Prior to TEM imaging, samples were passivated in 10 % oxygen after reduction.

2.2.8 Small-angle X-ray Scattering (SAXS)

For ALD catalysts, SAXS experiments were performed at 12-ID-B station with X-ray energy of 12 keV at the Advanced Photon Source of the Argonne National Laboratory. The two-dimensional images were radially averaged to produce 1-D plots of scattered intensity $I(q)$ versus q, where $q = 4\pi (\sin\theta) / \lambda$. θ is scattering angle and λ is wavelength. A Pilatus 2M detector (Dectris Ltd.) was used to acquire scattering data with typical exposure times in a range of 0.1 - 1.0 seconds.

2.2.9 Scanning transmission electron microscopy (STEM)

For SMSI Co/TiO_2 catalysts, STEM was carried out using a C_s-corrected FEI Titan microscope operated at 200 kV. HAADF STEM images were collected with a 24.5 mrad probe semiangle and ~25 pA probe current. To prepare the samples for STEM, samples were suspended in ethanol, ultrasonicated for 5 minutes and then deposited on a carbon-coated copper grid. STEM samples were plasma cleaned for 20 minutes before loading into the microscope. Prior to STEM imaging, samples were passivated in 10 % oxygen after reduction.

2.2.10 Raman spectroscopy

For SMSI Co/TiO_2 catalysts, Raman experiments were carried out with a high-performance Renishaw InVia Raman Spectrometer with a 514 nm laser. This is a Modu-Laser Stellar-REN with an output of 50 mW and an approximate power of 15-20 mW at the sample. All measurements used a 2400 l mm^{-1} grating with an efficiency of approximately 30 % at 514 nm. *In situ* Raman studies used an Olympus LMPlanFL N objective with 50x magnification and a working distance of 10.6 mm. Scattered light was filtered into a UV enhanced (lumogen coated) deep depleted array detector (Renishaw). The laser line was calibrated with a neon calibration lamp under the Full Calibration technique to match the calibration wavenumbers and intensities to the collected values. In addition to calibrating the laser, the Raman spectrograph was calibrated to an internal Si standard at 520.7 cm^{-1}. Raman measurements were taken with a range of 100-1200 cm^{-1} and a dispersion of 1.36565 cm^{-1} $pixel^{-1}$. *In situ* measurements were taken with a fully open aperture and a 10 seconds exposure time. Approximately 10 mg of sample was used for each *in situ* trial. Experiments were performed in a high-temperature cell (Linkam CCR1000) designed for temperatures up to 1273 K. This setup used a quartz window and water-cooled O-rings. The temperature was controlled by a Linkam T95-HT system. Gas flows during *in situ* experiments were controlled by mass flow controllers (Bronkhorst EL-Flow) with maximum flow rates of 50, 100, and 40 mL min^{-1} for hydrogen, helium, and oxygen, respectively. The mass flow controllers were directed by a digital readout system (Bronkhorst series E-7000) capable of mixing gases with variable flow rates. A flow rate of 10 mL min^{-1} hydrogen (Airgas, Ultra High Purity) was used for all reductions, and 20 mL min^{-1} of a 20 % oxygen/helium (Airgas, Ultra High Purity) mixture was used for all calcinations. Heating ramps for *in situ* reductions and calcinations were kept at 1 and 5 K min^{-1}, respectively, as was the case in reactivity treatments. Once the desired temperature was

reached, it was held there for two hours. The sample was cooled to room temperature after calcination and reduced with a 1 K min^{-1} heating ramp for spectra that required calcination prior to reduction. Spectra used in this study were taken at room temperature under 16 mL min^{-1} helium flow after the calcination and/or reduction was complete.

2.3 Reaction Studies and Analysis

2.3.1 High-throughput studies

A high-throughput reactor (HTR) manufactured by HEL Group (Model # CAT24) was used to test various catalysts for hydrogenation and hydrogenolysis reactions. This reactor consisted of 24 batch-wells machined into a cylindrical chamber (Figure 2.1a). The bottom section (Figure 2.1a) is the glass tube holder on which the top plate is placed. The top plate (Figure 2.1b) has an integrated condenser head. There are two barb connections to connect to a chiller. Cooling tips are positioned into the wells. On top is the clamp fitting over the top plate and screwing down onto the bottom chamber where an O-ring positioned. The HTR has a central manifold fitting with two ball valves for gas flowing and pressurizing the reactor, a thermocouple, a pressure gauge, and an emergency pressure relief valve. The system temperature, pressure, gas flow rate, and stirring speed were controlled and monitored through WinIso E670 system software.

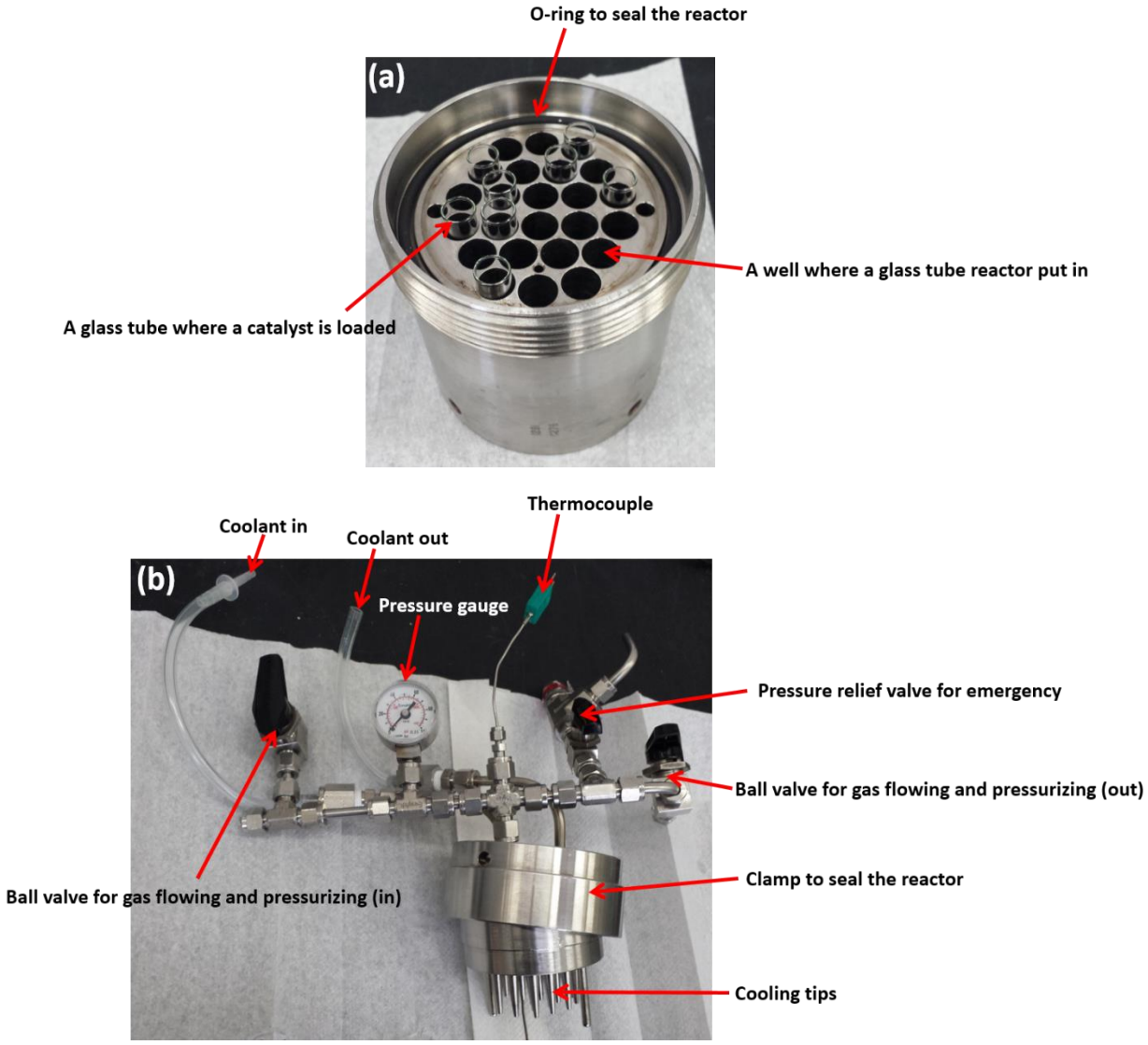

Figure 2.1 (a) Bottom section of the high-throughput reactor (HTR) and (b) Top plate of the HTR.

Aqueous-phase hydrogenation (APH) and hydrogenolysis reactions were performed in the HTR. As the feedstocks, 5 wt% aqueous solution of acetaldehyde (Sigma-Aldrich, ≥ 99 %), 5 wt% aqueous solution of propanal (Sigma-Aldrich, ≥ 97 %), 5 wt% aqueous solution of acetone (Fisher, ≥ 99.5 %), 4.8 wt% aqueous solution of furfural (Sigma-Aldrich, 99 %), 4.8 wt% aqueous solution of furfuryl alcohol (Sigma-Aldrich, ≥ 98 %), 5 wt% aqueous solution of tetrahydrofurfuryl alcohol (Sigma-Aldrich, 99 %), and 5 wt% aqueous solution of xylitol (Acros Organics, 99 %) were used.

Prior to a reaction, catalysts (10 to 15 mg) were loaded into glass tubes and placed in the HTR. A catalyst was typically put into two random wells to insure consistency between the wells. The whole HTR unit was then placed on a heating/stirring mantle. The catalysts were reduced by introducing hydrogen at 573 K (1 K min^{-1}) for noble meal catalysts and bimetallic catalysts and at 723 K (1 K min^{-1}) for base metal catalysts for 2 hours. After reduction of the catalysts, the reactor was held at the temperatures while helium was passed through the reactor for 30 minutes to remove hydrogen. The reactor was then cooled to room temperature in flowing helium and sealed under helium for transport to a glove box. Inside the glove box, the top plate were removed under a helium atmosphere. Magnetic stir bars were then placed into each of the glass tubes and 2 mL of an aqueous feedstock solution was added to each of the glass tubes with a micropipette. The HTR was sealed again in the glove box and transported to put on the heating/stirring mantle, connected to the control system and the HTR was pressurized to 4.38 MPa with hydrogen. Next, the HTR was heated to the reaction temperature at a rate of 20 K min^{-1}. More hydrogen was introduced to maintain the final pressure at 5.41 MPa. Once a reaction set finished, the HTR was removed from the heater and cooled down in an ice bath at a rate of around 14 K min^{-1}. After reaching room temperature, the HTR was depressurized to atmospheric pressure, and samples in each well were taken by a 3 mL syringe and filtered by a 0.2 μm syringe filter (Whatman). A stirring speed of 800 rpm was used during a reaction. Experiments with the stirring speed of 500 rpm and 800 rpm showed no change in activity of catalyst. This indicates there was no external mass transfer limitation at a stirring speed of 800 rpm.

2.3.2 Continuous flow reaction studies

APHDO and APH reactions were performed in a stainless-steel tubular reactor (6.35 mm outer diameter and 5.46 mm inner diameter). For APHDO reactions, 20 wt% aqueous solution of sorbitol (Fisher) was used as the feedstock. For APH reactions, 2 wt% aqueous solution of furfuryl alcohol (Sigma-Aldrich, ≥ 98 %), 2 wt% aqueous solution of furfural (Sigma-Aldrich, 99 %), and 2 wt% aqueous solution of xylose (Acros Organics, 99+ %) were used as the feedstocks. The reactor was heated by a furnace (Lindberg). A uniform temperature profile along the catalyst bed was achieved using aluminum filler inserted in the void between the furnace and the tubular reactor. Blank reactions without catalyst were run to confirm that there is no homogeneous reaction and no effect of the reactor materials. For catalyst testing, a catalyst (3.3 g for Pd/Zr-P and Pd_1Fe_3/Zr-P; 0.5 g for ALD and SMSI cobalt catalysts) without diluents was loaded into the reactor with quartz wool and cylindrical quartz beads packed on both sides. Prior to a reaction, the Pd/Zr-P and Pd_1Fe_3/Zr-P catalysts were reduced *in situ* under hydrogen flow (128 mL min^{-1}) in situ at 573 K (1 K min^{-1}) for 2 hours. ALD and SMSI cobalt catalysts were calcined under air flow (100 mL min^{-1}) and then reduced under hydrogen flow (100 mL min^{-1}) *in situ* at the temperatures mentioned in Chapters 5 and 6 respectively. After the reduction was complete, the furnace was cooled to the desired reaction temperature and the reactor system was pressurized to target pressure using a back-pressure regulator. An aqueous feedstock solution was then fed to the reactor using a high-performance liquid chromatograph (HPLC) pump (Varian ProStar), co-fed with hydrogen (Airgas, Ultra High Purity) of 40 mL min^{-1}. The feedstock solution was fed upwardly to precisely control liquid feed residence time by filling the catalyst bed uniformly. Aqueous solutions of feedstocks included 20 wt% sorbitol for APHDO reactions and 2 wt% furfuryl alcohol, 2 wt% furfural, and 2 wt% xylose for APH reactions. A 150 mL gas-liquid separator was used to

accumulate liquid products at the top of the reactor. Gaseous products continued to flow to the back-pressure regulator to maintain the reaction pressure. Both an excess flow shut-off valve and a pressure relief valve were installed in the reactor system to ensure safe operation. The Mears' criterion and the Weisz-Prater criterion indicated the system was free of external and internal mass transfer limitations.[57, 58]

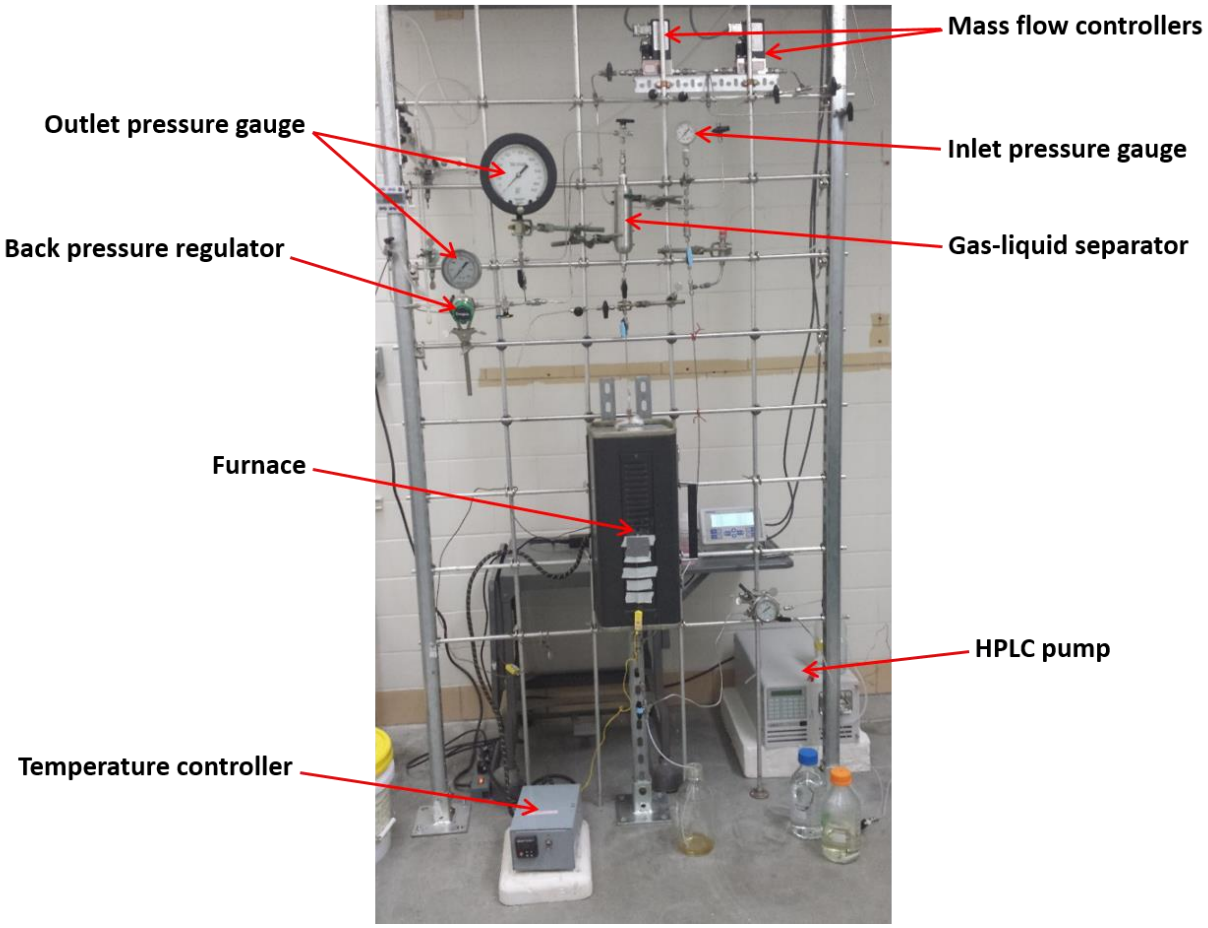

Figure 2.2 Continuous flow reactor system.

2.3.3 Analytical methods

The liquid samples collected after reactions in the HTR were analyzed by a gas chromatograph (GC; Agilent 7890A) with a flame ionization detector (FID) fitted with a Rtx®-

VMS capillary column (Restek). A HPLC (Shimadzu LC-20AT) with and a refractive index detector (RID) fitted with an Aminex® HPX-87H column (Bio-Rad) was used to analyze sugars such as xylose and xylitol. The gaseous products from the continuous flow reactor were analyzed using an online GC (Shimadzu GC-2014) with a FID fitted with a Rt®-Q-Bond capillary column (Resteck) and a TCD fitted with a GS-CarbonPLOT column (Agilent). A liquid sample accumulated in the gas-liquid separator was drained periodically into a collecting container, followed by being filtered through a 0.2 μm syringe filter. For APHDO of sorbitol, the liquid sample accumulated in the gas-liquid separator was drained periodically into a collecting container in which 20 mL of cyclohexane (Acros Organics, 99+ %) was preloaded to extract organic phase and to decrease the carbon loss from vaporization of some of the products. The liquid products were analyzed using a GC (Shimadzu GC-2010) with a FID fitted with a Rtx®-VMS capillary column (Restek) and a HPLC (Shimadzu LC-20AT) with a RID fitted with an Aminex® HPX-87H column (Bio-Rad). Total organic carbon (TOC) measurements were performed using a Shimadzu TOC-VCPH Analyzer for the liquid samples obtained from the reaction to measure the overall carbon balance. TOC calibrations were performed with carbon standards (SpectroPure).

CHAPTER 3

Aqueous-Phase Hydrogenation and Hydrogenolysis of Biomass-Derived Oxygenates over Monometallic Catalysts: Comparative Study

J. Lee, Y. Xu and G. W. Huber, High-Throughput Screening of Monometallic Catalysts for Aqueous-Phase Hydrogenation of Biomass-Derived Oxygenates, *Applied Catalysis B: Environmental*, 2013, **140-141**, 98-107.

3.1 Background

Aqueous-phase hydrogenation (APH) reactions are commonly used for conversion of biomass into different fuels and chemicals. APH is a critical part of aqueous-phase conversion of sugars into alkanes[5, 29, 30] including the production of hexane from sorbitol[29] and the conversion of glucose into C9, C12, and C15 alkanes.[30] There are several types of functionalities that are hydrogenated during biomass conversion, including the hydrogenation of C=O, C=C, and C-O-C bonds. APH of C=O, C=C, and C-O-C bonds are critical for aqueous-phase alkane production from sugar alcohols.[43]

There have been many studies on the hydrogenation of oxygenated compounds over heterogeneous monometallic catalysts. Olcay *et al.* studied APH of acetic acid over a series of different metal catalysts, concluding that Ru is the most active metal for the conversion of acetic acid and the most selective toward ethanol production.[59] The rate of catalyst activity decreased as Ru > Rh ~ Pt > Pd ~ Ir > Ni > Cu.[59] Narayanan *et al.* tested alumina supported Ni, Co, and Fe catalysts for the vapor phase hydrogenation of acetone, and concluded that the activity decreased as Ni > Co > Fe.[60] A study compared five different metal catalysts (Pt, Ir, Ru, Ni, and Co) for the vapor phase hydrogenation of acrolein, concluding that Pt and Ru had faster reaction rates for acrolein hydrogenation under vapor phase than Ir, Ni, and Co.[61]

As shown in Table 3.1, eight molecules, including acetaldehyde, propanal, acetone, xylose, furfural, furfuryl alcohol, tetrahydrofurfuryl alcohol (THFA), and xylitol, were chosen as biomass-derived model compounds for aqueous-phase hydrogenation and hydrogenolysis. These molecules have the same functionalities that are present in the aqueous fractions of biomass-derived feedstocks like pyrolysis oil and hydrolysis solutions. Polyols such as xylitol and sorbitol can be produced from lignocellulosic biomass.[62, 63] A large variety of alcohols, aldehydes, ketones, and

furans are commonly found in bio-oil produced from fast pyrolysis of biomass.[14] Alcohols, ketones, and tetrahydrofurans (THFs) can also be produced from hydrodeoxygenation of sugar alcohols.[39]

Table 3.1 List of feedstocks used as biomass-derived model compounds.

Feedstock		Reaction
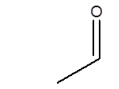	acetaldehyde	C=O bond hydrogenation
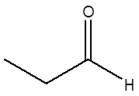	propanal	C=O bond hydrogenation
	acetone	C=O bond hydrogenation
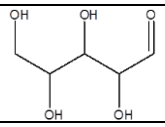	xylose	C=O bond hydrogenation
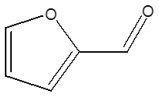	furfural	C=O bond hydrogenation
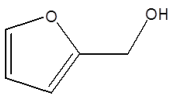	furfuryl alcohol	C=C bond hydrogenation
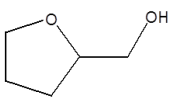	tetrahydrofurfuryl alcohol	C-O-C bond cleavage
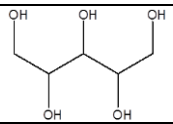	xylitol	C-C bond cleavage

High-throughput techniques have been developed to rapidly screen large amounts of catalytic material.[24, 28, 64-78] High-throughput studies have also led to the development of more efficient catalysts for many processes including hydrogen production from biomass,[24] oxidation of ethane,[67] and hydrogen evolution reactions.[69] The advantage of high-throughput catalytic studies is that large data bases can be rapidly built up.

In this chapter, the activity of monometallic catalysts for aqueous-phase hydrogenation and hydrogenolysis of feedstocks shown in Table 3.1 was compared in the same reactor system to get the insight into which metal might be useful for aqueous-phase conversion of more complicated biomass molecules.

3.2 Results and Discussion

3.2.1 Catalyst characterization

Table 3.2 lists the hydrogen chemisorption results obtained on the prepared γ-Al_2O_3-supported monometallic catalysts with varying metal loadings. The values of hydrogen uptake of the prepared catalysts are consistent with the values reported in previous studies. For example, the value of hydrogen uptake of the 1 wt% Pd/γ-Al_2O_3 agrees well with a value of hydrogen uptake of a commercial 1.2 wt% Pd/Al_2O_3.[79] The hydrogen uptake value of the 10 wt% Co/γ-Al_2O_3 also agrees with one of a 12.4 wt% Co catalyst.[80]

The hydrogen chemisorption data was used to estimate the metal dispersion and mean particle size of the Pd, Pt, Ru, and Rh catalysts using the equations below:

$$\text{Metal dispersion, } D\ (\%) = \frac{2\ \times \text{hydrogen uptake}}{\mu\text{mol of metal}_{\text{total}}/\text{g}_{\text{cat.}}} \times 100$$

$$\text{Mean metal particle size} = \frac{6v_m/a_m}{D}$$

where v_m is volume occupied by an atom in bulk metal and a_m is area occupied by a surface atom.[81] The values of v_m and a_m of metals are presented in Table A1. The dispersion and mean particle size of the Ni and Co catalysts were not estimated because the extent of reduction of these catalysts was not measured here.

Table 3.2 Hydrogen chemisorption data of the prepared monometallic catalysts.

Catalyst	Hydrogen uptake (μmol $g_{cat.}^{-1}$)	Dispersion (%)	Mean particle size (nm)
0.5 wt% Pd	12.4	52.6	2.1
1 wt% Pd	21.0	44.7	2.5
3 wt% Pd	58.1	41.2	2.7
0.5 wt% Pt	7.3	57.2	2.0
1 wt% Pt	14.0	54.4	2.1
3 wt% Pt	37.7	49.1	2.3
0.5 wt% Ru	3.6	14.7	8.8
1 wt% Ru	9.4	19.1	6.8
3 wt% Ru	34.3	23.1	5.6
5 wt% Rh	72.9	30.0	3.6
5 wt% Ni	10.0	-	-
10 wt% Ni	31.5	-	-
20 wt% Ni	84.7	-	-
5 wt% Co	6.2	-	-
10 wt% Co	8.6	-	-
20 wt% Co	18.1	-	-

3.2.2 Aqueous-phase hydrogenation and hydrogenolysis

Reaction time was varied to keep the conversion less than 30 % to measure turnover frequency (TOF) of the prepared monometallic catalysts for hydrogenation and hydrogenolysis reactions. TOF, conversion, reaction time, and carbon balance for the APH reactions conducted in this study are shown in Tables A2, A3, A4, and A5 respectively. Figures 3.1 to 3.6 show the most active of each of the monometallic catalyst series.

The comparison of the TOFs for the APH of non-furanic aldehydes including acetaldehyde, propanal, and xylose is shown in Figure 3.1. The TOF of the APH of acetaldehyde and propanal decreased in the order: Ru > Ni > Pt > Pd > Co > Rh. The 3 wt% Ru catalyst was the most active catalyst for the APH of acetaldehyde and propanal. The Pt catalysts were more active than the Pd catalysts; for example, the activity of the 3 wt% Pt catalyst was 79 % higher than one of the 3 wt%

Pd catalyst for the APH of acetaldehyde. The 5 wt% Rh catalyst had the lowest activity for the APH of acetaldehyde and propanal. The activity for the APH of xylose decreased in the order: Ru > Ni ~ Co > Pt > Rh ~ Pd. This result is consistent with the work of Wisniak *et al.* who concluded that the rate of xylose hydrogenation decreased according to the order Ru > Ni > Rh > Pd.[82, 83] Yadav *et al.* also concluded that supported Ru catalysts were more selective to xylitol than Raney Ni catalyst for xylose hydrogenation.[84] The 3 wt% Ru catalyst had the highest activity for the APH of xylose. The second most active metals were the 10 wt% Ni catalyst and the 5 wt% Co catalyst. The 3 wt% Pd catalyst had the activity for the APH of xylose. The 3 wt% Pt catalyst was 40 % more active than the 5 wt% Rh catalyst.

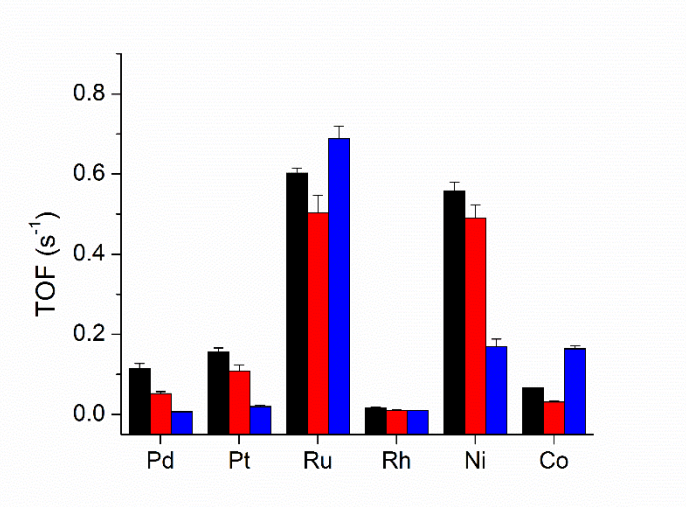

Figure 3.1 Comparison of TOFs of the APH of non-furanic aldehydes at 373 K (■ acetaldehyde to ethanol; ■ propanal to 1-propanol; ■ xylose to xylitol).

The comparison of the TOFs of the APH of acetaldehyde, propanal, and acetone is shown in Figure 3.2. The activity for the APH of acetone decreased in the order: Ru > Ni ~ Rh > Pt > Co > Pd whereas the activity for the APH of acetaldehyde and propanal decreased in the order: Ru > Ni > Pt > Pd > Co > Rh. Rh is more active for hydrogenation of C=O of ketone than for

hydrogenation of C=O of aldehyde. This is consistent with a previous study reporting that a supported Rh catalyst showed much higher conversion for acetone hydrogenation than propanal hydrogenation.[85] The rate of hydrogenation of ketone (*e.g.*, acetone) is faster than the rate of hydrogenation of aldehydes (*e.g.*, acetaldehyde and propanal) at the same reaction conditions. Binding energy of acetaldehyde and acetone on Pt(111) is -7 and -3.3 kcal mol^{-1}, respectively.[86] Also, binding energy of acetaldehyde and acetone on Co(0001) is -7 and -5 kcal mol^{-1}, respectively.[86] The weaker binding energy of ketone most likely leads to higher activity for hydrogenation of C=O bond.[85, 87]

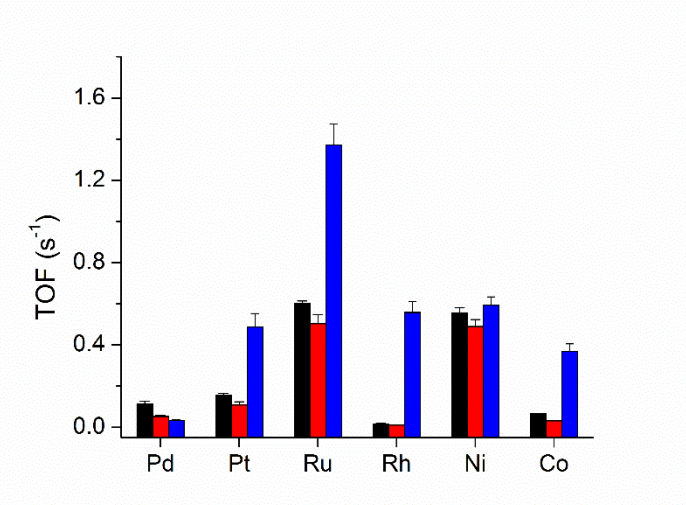

Figure 3.2 Comparison of TOFs of the APH of propanal and acetone at 373 K (■ acetaldehyde to ethanol; ■ propanal to 1-propanol; ■ acetone to 2-propanol).

Ru is most active for the APH of non-furanyl carbonyl compounds. For hydrogenation of xylose to xylitol, activation energy for Ru is lower than that for Ni so that Ru is more active than Ni at the same reaction conditions.[82] It was shown that Ru is most active for APH of acetic acid to ethanol in a continuous-flow reactor.[59]

As shown in Figure 3.3, however, the activity for the APH of furfural decreased in the order: Pd > Ni > Co > Ru > Pt > Rh. The 3 wt% Pd catalyst had the highest rate of the APH of furfural. Previous studies also reported that Pd is an effective catalyst for furfural hydrogenation to the corresponding alcohol at low temperatures.[88, 89] A current study has reported that furfural binds more weakly on Pd than on Pt.[90] The weaker furfural binding energy on Pd might lead to higher activity for furfural hydrogenation.[87]

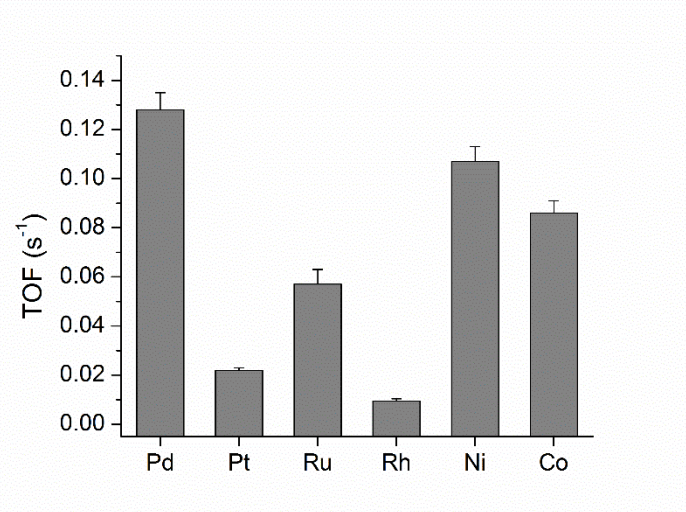

Figure 3.3 Comparison of TOFs of the APH of furfural at 373 K (■ furfural to furfuryl alcohol).

The TOF of different metals for the APH of furfuryl alcohol, which involves the hydrogenation of C=C bonds of furan ring, is shown in Figure 3.4. The activity for THFA production from furfuryl alcohol decreased in the order: Pd > Ni > Ru > Pt > Rh >> Co. The Co catalysts were inactive for the APH of furfuryl alcohol at 353 K. Pt and Rh showed relatively slow rates of the APH of furfuryl alcohol compared to other metals. Sitthisa and Resasco showed that Pd and Ni catalysts were active for the production of THFA from furfuryl alcohol.[91]

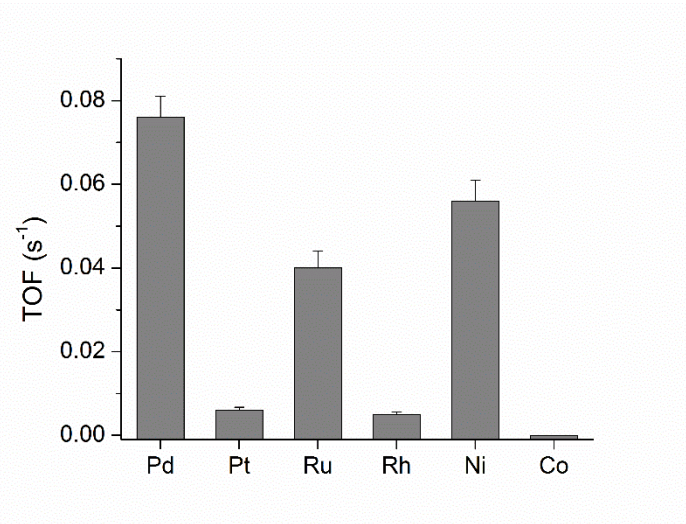

Figure 3.4 Comparison of TOFs of the APH of furfuryl alcohol at 353 K (■ furfuryl alcohol to THFA).

The aqueous-phase hydrogenolysis of THFA at 523 K was performed as a model reaction for C-O-C bond hydrogenolysis. Ni was more active than Pt for the aqueous-phase hydrogenolysis of THFA as shown in Figure 3.5. Pt and Ni produced 1,2-pentanediol or 1,5-pentanediol through cleaving C-O-C bond of THFA. This indicates that the location of C-O-C bond cleavage depends on the kind of metal. Sitthisa and Resasco showed that C-O-C bond cleavage occurred on a Ni/SiO_2 catalyst for THF hydrogenolysis to butanol at 523 K.[91] This might be because the interaction between the THF ring and Ni surface weakens C-O-C bond of the THF ring, thereby causing the ring opening reaction.[91]

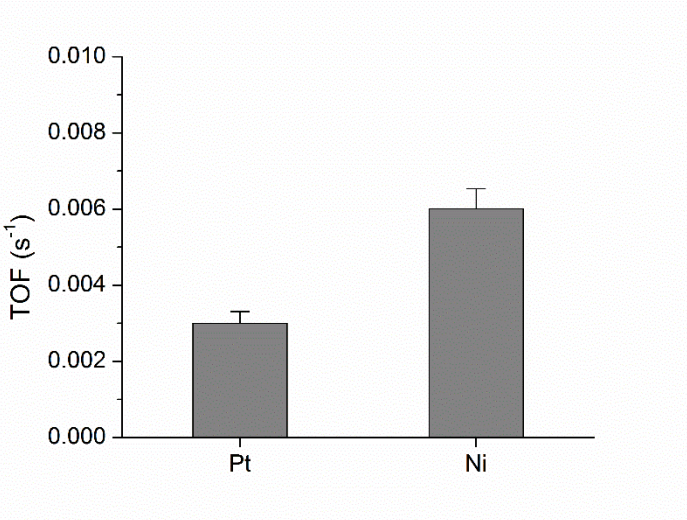

Figure 3.5 Comparison of TOFs of the aqueous-phase hydrogenolysis of THFA at 523 K (■ THFA to pentanediol).

The aqueous-phase hydrogenolysis of xylitol was carried out at 473 K as a model reaction for C-C bond cleavage. Figure 3.6 shows a comparison of the activity of the aqueous-phase hydrogenolysis of xylitol over monometallic catalysts, showing the most active of each of the monometallic catalyst series. The TOF of the aqueous-phase hydrogenolysis of xylitol decreased as: Ru > Co > Pt > Ni > Pd. Previous studies also showed that Ru is active for hydrogenolysis of polyols under neutral conditions.[92, 93]

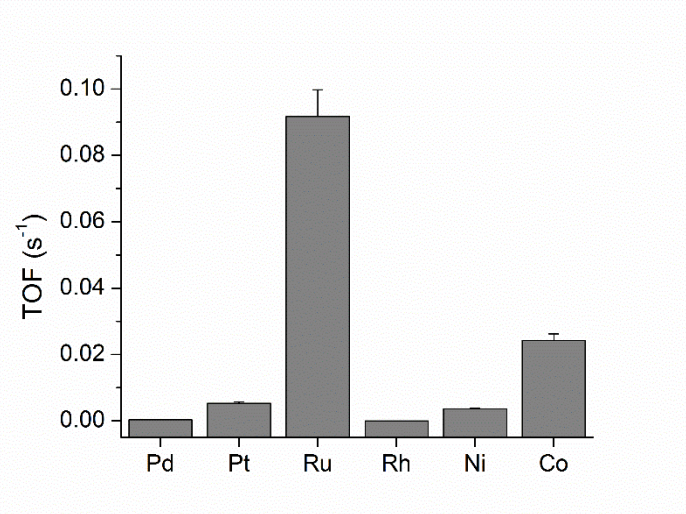

Figure 3.6 Comparison of TOFs of the aqueous-phase hydrogenolysis of xylitol at 473 K.

Selectivity for the aqueous-phase hydrogenolysis of xylitol over the monometallic catalysts is shown in Table 3.3. Conversion and carbon balance for the reaction are shown in Table A6. The main products from the xylitol hydrogenolysis on the Pt, Ru, Ni and Co catalysts were ethylene glycol and propylene glycol. Propylene glycol was the only product observed with the 3 wt% Pd catalyst; however, the 3 wt% Pd catalyst had a slow reaction rate. Small amounts of glycerol were detected with Ru catalysts. Ethylene glycol, propylene glycol and ethanol were detected with the Co catalysts.

Table 3.3 Selectivity for the aqueous-phase hydrogenolysis of xylitol at 473 K.

	methanol	ethanol	ethylene glycol	propylene glycol	propanol[(a)]	glycerol	butanol[(b)]	butanediol[(c)]	2-pentanol	THFA
3 wt% Pd	0	0	0	3.4	0	0	0	0	0	0
0.5 wt% Pt	0	0	2.6	5.2	0	0	0	0	0	0
1 wt% Pt	0	1.9	3.1	3.5	1.8	0	0	0	0	0
3 wt% Pt	1.4	2.0	5.3	6.4	1.5	0	2.4	0	1.8	1.0
0.5 wt% Ru	1.4	2.7	6.3	4.5	2.1	0	0	1.6	0	0
1 wt% Ru	1.0	3.3	9.9	10.8	4.1	4.8	2.6	5.6	1.4	1.0
3 wt% Ru	0.9	4.0	3.2	13.6	7.2	4.0	5.3	13.5	2.2	0
10 wt% Ni	0	3.7	29.3	18.5	0	0	0	0	0	0
20 wt% Ni	2.5	2.3	16.3	9.1	0	0	0	1.8	0	1.5
5 wt% Co	0	2.0	16.6	16.1	0	0	0	0	0	0
10 wt% Co	0	2.2	10.3	10.5	0	0	0	0	0	0
20 wt% Co	0	3.0	9.1	7.7	0	0	0	0	0	0

[(a)]Propanol includes 1-propanol and 2-propanol.

[(b)]Butanol includes 1-butanol and 2-butanol.

[(c)]Butanediol includes 1,2-butanediol and 2,3-butanediol.

Scheme 3.1 shows proposed reaction pathways for the aqueous-phase hydrogenolysis of xylitol. Our previous study showed that decarbonylation, dehydrogenation, hydrogenation and retro-aldol condensation reactions occur on metal sites, whereas dehydration reaction occurs on

acid sites.[38] Xylitol can undergo two different parallel reactions. One of these reactions involves an initial dehydration step to 1,4-anhydroxylitol, similar to the reaction pathway for APHDO of sorbitol shown in our previous study.[38] The 1,4-anhydroxylitol can undergo further dehydration and hydrogenation to produce THFA. The THFA can yield 2-methyltetrahydrofuran by dehydration and hydrogenation. The 2-methyltetrahydrofuran can react with hydrogen further to form 2-pentanol. 2-Pentanol is probably produced by hydrogenolysis of C-O-C bond in 2-methyltetrahydrofuran on Pt and Ru surfaces only, which is consistent with the results from THFA hydrogenolysis in this study. The 1,4-anhydroxylitol is also able to undergo decarbonylation to tetrahydrofuran-3,4-diol from which 2,3-butanediol and tetrahydrofuran (THF) can be produced further by dehydration and hydrogenation. 1-Butanol and 2-butanol are possibly made from 2,3-butanediol and THF by undergoing dehydration and hydrogenation, respectively. C1-C3 compounds are produced mainly via retro-aldol condensation, also described in the literature.[93] Xylitol converts to xylose via dehydrogenation, and the aldehyde, xylose, can undergo retro-aldol condensation to produce glycolaldehyde and glyceraldehyde. The glycolaldehyde then reacts with hydrogen to form ethylene glycol, and the glyceraldehyde further makes propylene glycol via dehydration and hydrogenation.

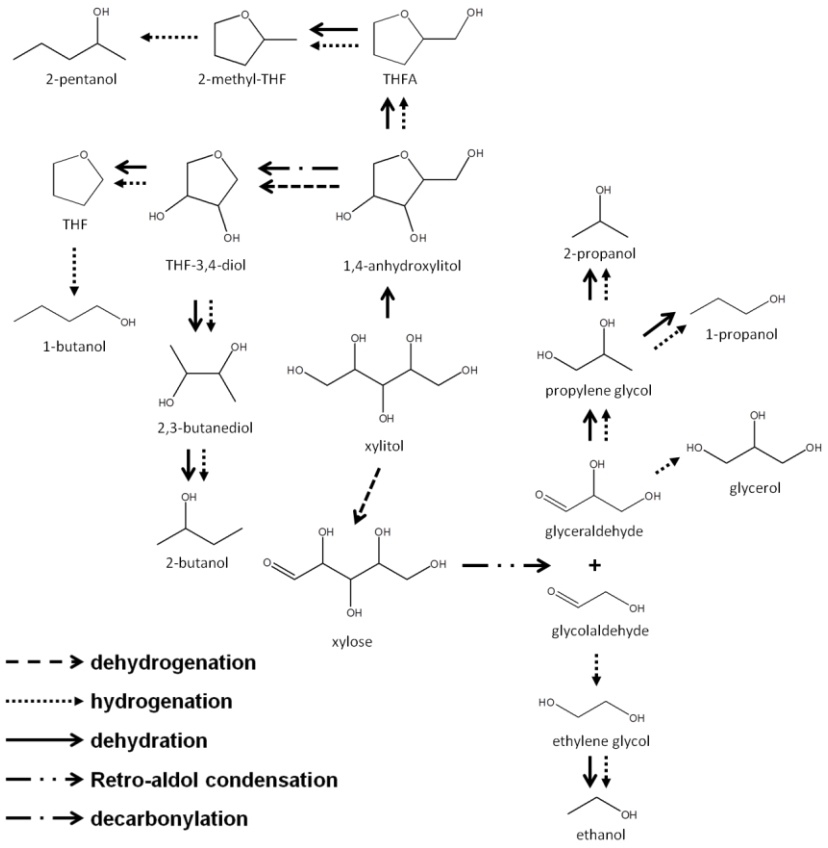

Scheme 3.1 Proposed reaction pathways for aqueous-phase hydrogenolysis of xylitol.

Table 3.4 summarizes the results of this study and compares the results with previous studies done for hydrogenation and hydrogenolysis reactions.[26, 59, 60, 82, 83, 86, 92, 93] The order of catalytic activity from this study is consistent with previous studies.

Table 3.4 Hydrogenation and hydrogenolysis of oxygenates on monometallic catalysts.

Reaction (phase)	Feed / product	Reaction conditions	Activity measured on	The order of activity	Reference
hydrogenation (aqueous)	acetaldehyde / ethanol	373 K, 800 psia, 5 wt% acetaldehyde solution	a per site basis with H_2 chemisorption	Ru ~ Ni > Pt > Pd > Co > Rh	Lee *et al.*[74]
hydrogenation (gas)	acetaldehyde / ethanol	343 K, H_2/acetaldehyde = 4:1	a per site basis with CO chemisorption	Pt > Co	Zheng *et al.*[86]
hydrogenation (aqueous)	propanal / 1-propanol	373 K, 800 psia, 5 wt% propanal solution	a per site basis with H_2 chemisorption	Ru ~ Ni > Pt > Pd > Co > Rh	Lee *et al.*[74]
hydrogenation (aqueous)	acetone / 2-propanol	373 K, 800 psia, 5 wt% acetone solution	a per site basis with H_2 chemisorption	Ru > Ni ~ Rh > Pt > Co > Pd	Lee *et al.*[74]
hydrogenation (gas)	acetone / 2-propanol	308 K, H_2/acetone = 2:1	a per site basis with CO chemisorption	Pt > Co	Zheng *et al.*[86]
hydrogenation (gas)	acetone / 2-propanol	373 - 523 K, 4.5 $cm^3 h^{-1}$ acetone feed rate	a per site basis with H_2 chemisorption	Ni > Co > Fe	Narayanan *et al.*[60]
hydrogenation (aqueous)	xylose / xylitol	373 K, 800 psia, 5 wt% xylose solution	a per site basis with H_2 chemisorption	Ru > Ni ~ Co > Pt > Rh ~ Pd	Lee *et al.*[74]
hydrogenation (liquid)	xylose / xylitol	373 - 398 K, 200 - 800 psig	a total catalyst basis	Ru > Ni > Rh > Pd	Wisniak *et al.*[82, 83]
hydrogenation (aqueous)	furfural / furfuryl alcohol	373 K, 800 psia, 4.8 wt% furfural solution	a per site basis with H_2 chemisorption	Pd ~ Ni > Co > Ru > Pt > Rh	Lee *et al.*[74]
hydrogenation (aqueous)	furfuryl alcohol / THFA	353 K, 800 psia, 4.8 wt% furfuryl alcohol solution	a per site basis with H_2 chemisorption	Pd > Ni > Ru > Rh ~ Pt >> Co	Lee *et al.*[74]
hydrogenation (aqueous)	acetic acid / ethanol	383 - 563 K, 5.17 MPa, 10 wt% acetic acid solution	a per site basis with H_2 chemisorption	Ru > Pt ~ Rh > Pd ~ Ir > Ni > Cu	Olcay *et al.*[59]
hydrogenolysis (aqueous)	xylitol / glycol	473 K, 800 psia, 5 wt% xylitol solution	a per site basis with H_2 chemisorption	Ru > Co > Pt > Ni > Pd	Lee *et al.*[74]
hydrogenolysis (aqueous)	xylitol / glycol	473 K, 4.0 MPa, 10 wt% xylitol solution	a total metal basis	Pt > Ru > Pd ~ Rh (with base)	Sun *et al.*[93]
hydrogenolysis (aqueous)	glycerol / glycol	473 K, 40 bar, 1 wt% glycerol solution	a per site basis with H_2 chemisorption	Ru > Pt (with no base) Pt > Ru (with base)	Maris *et al.*[92]

3.3 Conclusions

Ru was the most active metal for APH of C=O bond in non-furanyl molecules (*e.g.*, acetaldehyde, propanal, acetone, and xylose) at 373 K and for aqueous-phase hydrogenolysis of C-C bond (*e.g.*, xylitol hydrogenolysis) at 523 K. Pd was the most active metal for APH of C=O bond in furanyl molecules (*e.g.*, furfural) at 373 K and C=C bonds of furan ring at 353 K. Pt and Ni were active for hydrogenolysis of C-O-C bond in THFA at 523 K at which Pd, Rh, and Co were inactive.

CHAPTER 4

Aqueous-Phase Hydrogenation of Carbonyl Compounds and Aqueous-Phase Hydrodeoxygenation of Sorbitol over Bimetallic Catalysts

J. Lee, Y. T. Kim and G. W. Huber, Aqueous-Phase Hydrogenation and Hydrodeoxygenation of Biomass-Derived Oxygenates with Bimetallic Catalysts, *Green Chemistry*, 2014, **16**, 708-718.

4.1 Background

Catalytic hydrogenation of carbonyl groups is widely applicable for organic synthesis in chemical industries.[85, 94-96] Selective hydrogenation of compounds containing C=O and C=C bonds is an important reaction route for the production of fine chemicals.[97, 98] Furthermore, APH of C=O bond is an important initial reaction step for the conversion of biomass to liquid fuels.[99] It is also a critical step in APHDO where hydrogen is added to biomass-derived molecules to hydrogenate C=O and C=C bonds.[29, 38, 53]

Bimetallic catalysts often have a higher activity than either of their parent metals.[100] For instance, Co and Ni promoted Pt catalysts exhibited a higher activity for the hydrogenation of C=O bond than the corresponding monometallic catalysts.[86, 101] A bimetallic Ni-Pd catalyst was more active than Raney Ni for the hydrogenation of HMF and furfural.[102] The addition of Ni, Co, and Fe to Pt catalyst increased the activity for APR of ethylene glycol up to 3 times.[28] It was proposed that this increase in catalytic activity was because the Ni, Co, and Fe decrease the adsorption energy of CO and H on the Pt metal surface.[103-106] Bimetallic catalysts can also modify the reaction selectivity.[100] For example, Pd-Cu and Ni-Fe bimetallic catalysts had a higher selectivity toward hydrogenation products but lower selectivity toward decarbonylation products for furfural conversion than the pure monometallic Pd and Ni catalysts.[107, 108] Pt-Ni and Pt-Co bimetallic catalysts showed a higher deoxygenation products selectivity than monometallic Pt catalyst for hydrodeoxygenation of *meta*-cresol.[109] The addition of Sn to Ni catalyst can increase the hydrogen selectivity from 47 to 93 % for APR of ethylene glycol.[24]

In this chapter, the activity of Pd-, Ru-, and Pt-based bimetallic catalysts for aqueous-phase hydrogenation of carbonyl compounds (propanal, xylose, and furfural) was compared in the same reactor system. Then the most promising bimetallic catalyst for the APH of carbonyl compounds

was taken and tested for APHDO of sorbitol in a continuous flow reactor as a model reaction of biomass conversion.

4.2 Results and Discussion

4.2.1 Aqueous-phase hydrogenation of carbonyl compounds

Table 4.1 presents chemisorption uptake values of the catalysts tested. The addition of Ni and Co to the Ru catalyst and Fe to the Ru and Pt catalysts increased the hydrogen uptake. The hydrogen uptake went through a maximum at Ni/Pt = 1 or Co/Pt = 1 when Ni and Co were added to the Pt catalyst. However, the hydrogen uptake of Pd-based bimetallic catalysts was lower than the monometallic Pd catalyst by factors of 2 to 6. Hydrogen can adsorb into bulk Pd metal, causing an overestimation of the number of active sites.[110-112] CO chemisorption was performed for the Pd-based catalysts to check if hydrogen adsorbs into bulk Pd on the catalysts. The metal dispersion based on the hydrogen uptake and the CO uptake was 41.2 and 42.1 % respectively, suggesting that hydrogen atoms do not go into the Pd bulk for the catalyst systems. As more Ni and Co were added into the Pd catalyst, the CO uptake decreased, consistent with previous studies.[113, 114] Similar to the hydrogen uptake, the CO uptake also decreased as more Fe was added to the Pd catalyst. It is possible that Fe encapsulates Pd metal sites, allowing less hydrogen and CO chemisorb on the Pd sites. Shao *et al.* reported that overlayered Pd on Fe has a lower d-band center than Pd.[115] Greeley and Mavrikakis demonstrated that hydrogen binds weaker on Fe/Pd alloy than Pd metal.[116]

Table 4.1 Chemisorption data of the prepared monometallic and bimetallic catalysts.

Catalyst	Hydrogen uptake (μmol g^{-1})	CO uptake (μmol g^{-1})
Pd_1Ni_1	21.6	67.5
Pd_1Ni_3	22.5	56.9
Pd_1Co_1	21.8	57.4
Pd_1Co_3	22.9	50.1
Pd_1Fe_1	22.4	42.9
Pd_1Fe_3	10.6	13.2
3 wt% Pd	58.1	118.6
Ru_1Ni_1	44.8	-
Ru_1Ni_3	81.2	-
Ru_1Co_1	35.5	-
Ru_1Co_3	44.9	-
Ru_1Fe_1	36.5	-
Ru_1Fe_3	34.5	-
3 wt% Ru	34.3	-
Pt_1Ni_1	56.8	-
Pt_1Ni_3	48.7	-
Pt_1Co_1	51.9	-
Pt_1Co_3	46.4	-
Pt_1Fe_1	56.0	-
Pt_1Fe_3	38.8	-
3 wt% Pt	37.7	-
20 wt% Ni	84.7	-
20 wt% Co	18.1	-

Figure 4.1 shows TPR profiles of monometallic Pd/γ-Al_2O_3 and Fe/γ-Al_2O_3 catalysts and a bimetallic Pd_1Fe_3/γ-Al_2O_3 catalyst. Table 4.2 shows the hydrogen consumption during reduction for these catalysts. The monometallic Fe catalyst started to consume hydrogen at 590 K. Only 10.9 % of Fe species was reduced in the Fe/γ-Al_2O_3 catalyst. The monometallic Pd catalyst was completely reduced at < 430 K.[117] The hydrogen consumption of the bimetallic Pd_1Fe_3/γ-Al_2O_3

catalyst at < 430 K is 503.5 μmol g^{-1} which is higher than the hydrogen consumption of the monometallic Pd/γ-Al_2O_3 catalyst at < 430 K (280.3 μmol g^{-1}). This indicates that the existence of Pd not only lowers the reduction temperature of Fe species but also increases the extent of reduction of the Fe species. It is known that the presence of a noble metal lowers the reduction temperature of metal oxide.[118-120] Also, the addition of a noble metal into Fe catalyst increases the reducibility of iron oxides.[121-124] It is possible that a portion of Fe species is reduced and interacts with Pd forming Pd-Fe alloy after reduction.[125] However, other portion of Fe species could not be reduced and exist as iron oxides (most likely FeO and Fe_3O_4) and the iron oxides can be present on the periphery of Pd-Fe bimetallic particles.[125]

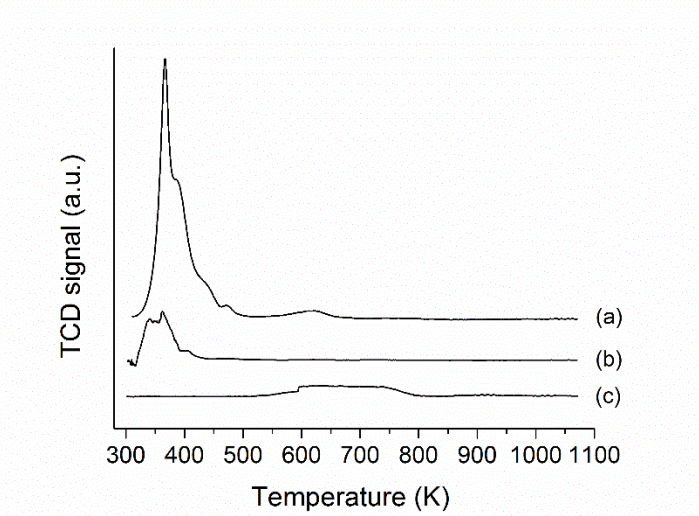

Figure 4.1 TPR patterns of (a) Pd_1Fe_3, (b) 3 wt% Pd/γ-Al_2O_3, and (c) 5 wt% Fe/γ-Al_2O_3.

Table 4.2 TPR analysis for Pd, Fe, and Pd_1Fe_3 catalysts.

Catalyst	Hydrogen consumption (μmol g^{-1})			Extent of reduction (%)
	< 430 K	430 ~ 590 K	590 ~ 800 K	
3 wt% Pd/γ-Al_2O_3	280.3	0	0	99.4
5 wt% Fe/γ-Al_2O_3	0	0	146.1	10.9
Pd_1Fe_3/γ-Al_2O_3	503.5	48.6	25.2	37.4

Conversion, reaction time, and carbon balance for the APH of the carbonyl compounds over the bimetallic catalysts are shown in Tables A7, A8, and A9, respectively.

Figure 4.2 shows the comparison of TOFs of the APH of propanal for various monometallic and bimetallic catalysts. The Pd-bimetallic catalysts were up to 63 times more active than the monometallic Pd catalyst for the APH of propanal. The bimetallic catalysts' activity for the APH of propanal decreased as Pd-Fe > Pd-Ni > Pd-Co. The Pd-Fe and Pd-Ni catalysts had the highest activity for the APH of propanal at a base metal to Pd molar ratio of 3:1 (Pd_1Fe_3 and Pd_1Ni_3). In contrast, the Pd-Co catalyst had the highest activity for the APH of propanal at a Co to Pd molar ratio of 1:1 (Pd_1Co_1). The Pd_1Fe_3 catalyst is the most active catalyst tested for the APH of propanal, 63 times higher than the rate of the 3 wt% Pd catalyst. The 3 wt% Ru catalyst was the most active monometallic catalyst for the APH of propanal with a hydrogenation rate of 0.5 s^{-1}. The Ru_1Co_1 catalyst had the highest hydrogenation rate for propanal conversion among all Ru bimetallic catalysts tested in this study. Based on a statistical student's *t*-test, the addition of Fe to the monometallic Ru catalyst did not significantly enhance the rate of the APH of propanal. Ni addition at a Ni/Ru = 1 level (Ru_1Ni_1) also did not statistically show any significant difference in the rate of the APH of propanal compared to the pure Ru catalyst. Further addition of Ni to form the Ru_1Ni_3 catalyst, decreased the catalytic activity for propanal hydrogenation to levels below that of the monometallic Ru catalyst. Addition of Ni, Co, and Fe to the monometallic Pt catalyst increased the rate of the APH of propanal. The maximum rate for all three of these bimetallic catalysts was observed at a base metal to Pt molar ratio of 3 to 1. The Pt_1Co_3 catalyst was very active for the APH of propanal with a rate of 1.4 s^{-1}. The Pt_1Fe_3 catalyst had a rate of 1.3 s^{-1} for the APH of propanal that was 14 times more active than the monometallic Pt catalyst. The TOF of the APH of

propanal for the Pt_1Ni_3 catalyst was 8 times as high as the TOF of the APH of propanal for the 3 wt% Pt catalyst. The results of Pt-Co bimetallic catalysts being more active for the APH of propanal are consistent with the work of Zheng *et al.* who showed that a Co-Pt bimetallic catalyst is more active than the parent monometallic catalysts (Pt and Co) for hydrogenation of acetaldehyde and acetone.[86] They concluded the increase in activity was because acetaldehyde and acetone adsorbed more weakly on Pt-Co-Pt(111) bimetallic surface than the parent monometallic surfaces (Pt(111) and Co(0001)).[86]

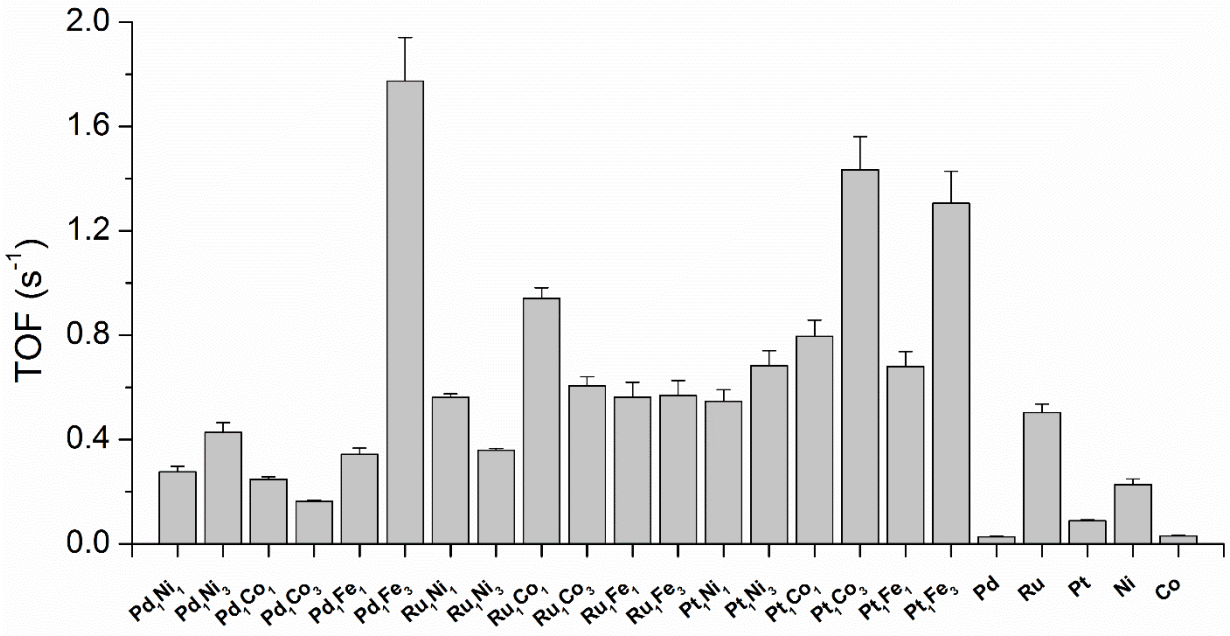

Figure 4.2 Comparison of TOFs of the APH of propanal at 373 K (■ propanal to 1-propanol).

As shown in Figure 4.3, the monometallic Ru catalyst was the most active catalyst for the APH of xylose to xylitol among all the tested catalysts. The addition of Ni, Co, and Fe to the Ru catalyst decreased the activity of the Ru catalyst for the APH of xylose. The addition of Ni, Co, and Fe to the monometallic Pd catalyst increased the activity for APH of xylose where each catalyst had a maximum rate at a base metal to Pd molar ratio of 3 to 1. The order of decreasing TOFs of

the APH of xylose decreased as Pd-Ni > Pd-Fe ~ Pd-Co. The Pd_1Ni_3 catalyst was 110 times more active than the monometallic Pd catalyst for the APH of xylose. The Pd_1Fe_3 catalyst had a 50 times higher reaction rate than the monometallic Pd catalyst for the APH of xylose. The addition of Ni, Co, and Fe to the monometallic Pt catalyst increased the activity for the APH of xylose with the bimetallic activity decreasing as Pt-Ni > Pt-Co > Pt-Fe. The Pt_1Ni_3 catalyst was 16 times more active than the monometallic Pt catalyst.

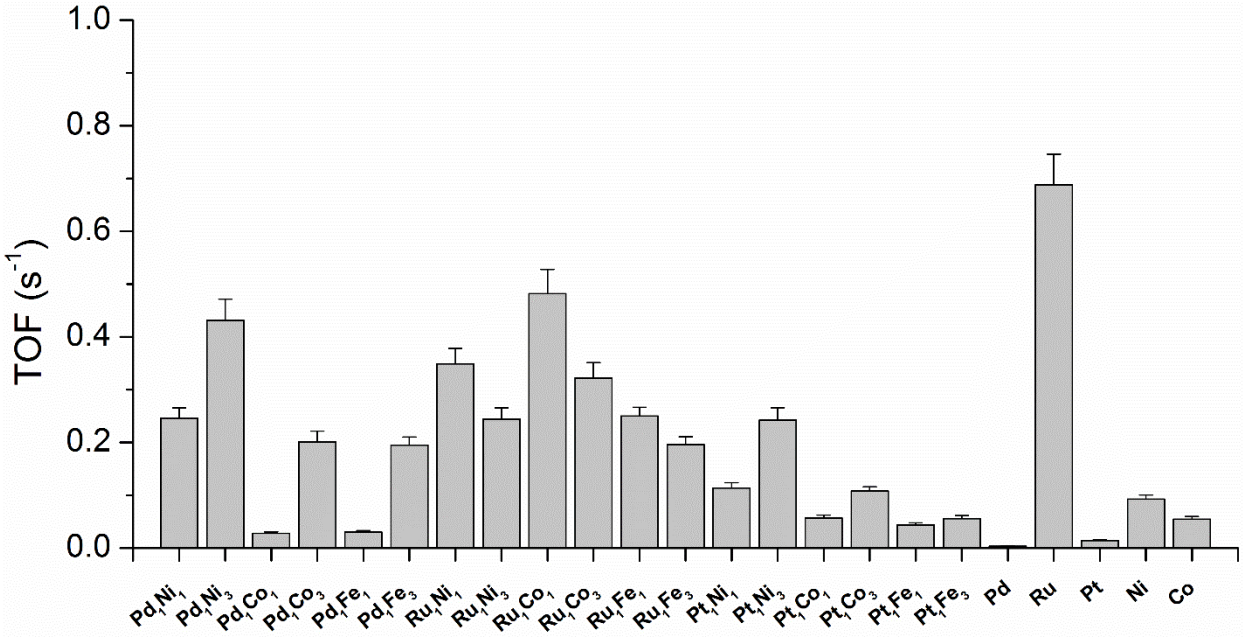

Figure 4.3 Comparison of TOFs of the APH of xylose at 373 K (■ xylose to xylitol).

Figure 4.4 shows the comparison of the activity of the catalysts for the APH of furfural. The products observed from the APH of furfural were furfuryl alcohol and THFA. Addition of Fe and Co to the Pd catalyst increased the activity of the Pd for the APH of furfural. The Pd-Fe bimetallic catalysts were the most active catalysts for the APH of furfural. The Pd_1Fe_3 catalyst was 9 times more active than the monometallic Pd catalyst for the APH of furfural. The Pd-Co bimetallic catalysts were up to 40 % more active than the monometallic Pd catalyst. The Pd_1Ni_3

bimetallic catalyst was less active than the 3 wt% Pd catalyst even though Pd and Ni are both very active metals for the APH of furfural. The addition of Fe and Co to the monometallic Ru catalyst increased the activity up to 2 times for the APH of furfural. Ni addition to the monometallic Ru catalyst decreased the activity by 19 %. The addition of Ni, Co, and Fe to the Pt catalyst increased the rate of the APH of furfural with the most active bimetallic catalysts being Pt-Fe. The Pt_1Fe_3 catalyst was 16 times more active than the 3 wt% Pt catalyst for the APH of furfural. The Pt_1Co_3 catalyst was 9 times as active as the 3 wt% Pt catalyst for the APH of furfural. The Pt_1Ni_1 catalyst had a higher TOF than the 3 wt% Pt catalyst but a lower TOF than the 20 wt% Ni catalyst.

The Pd-based bimetallic catalysts produced both furfuryl alcohol (88.5 to 93.1%) and THFA (6.9 to 11.5 %) from furfural. This indicates that the Pd-based bimetallic catalysts are also active in the hydrogenation of the C=C bond in a furan ring. The Ru-based bimetallic catalysts made THFA with small portions (0.2 to 3.6 %). The Pt-based bimetallic catalysts produced only furfuryl alcohol.

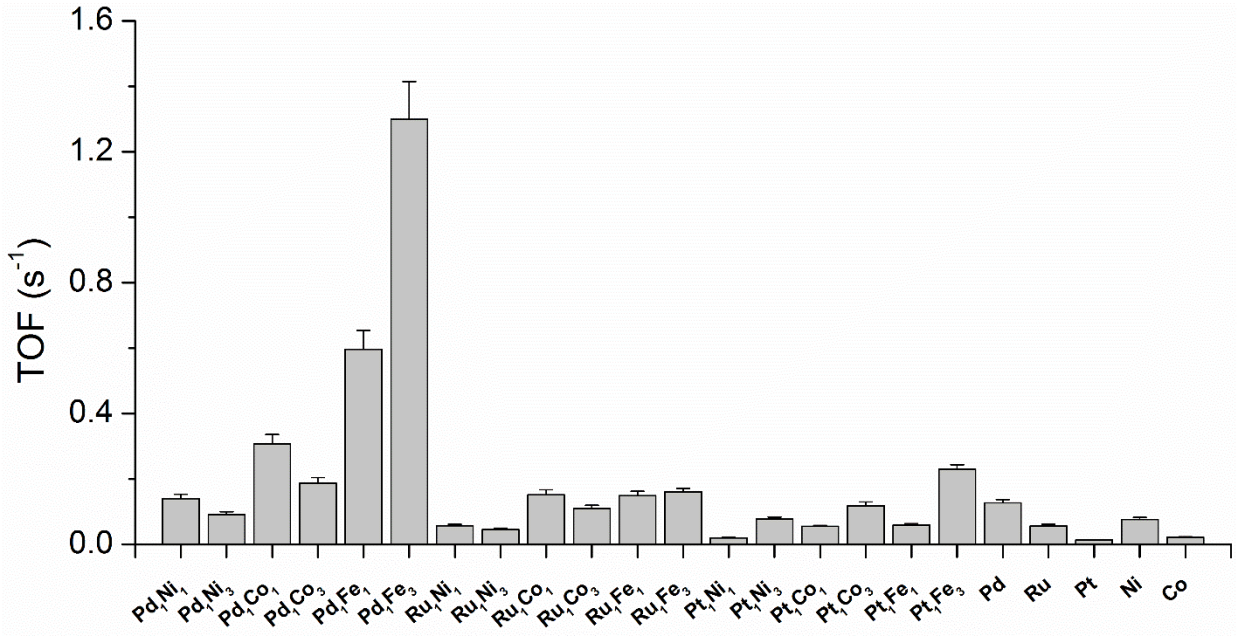

Figure 4.4 Comparison of TOFs of the APH of furfural at 373 K (■ furfural to furfuryl alcohol and THFA).

The results from the APH of different carbonyl compounds demonstrate that a Fe promoted Pd catalyst (*i.e.*, Pd_1Fe_3) is most active for the APH of propanal and furfural and also active for the APH of xylose (Figure 4.5), suggesting that Fe addition to Pd catalyst increases the activity for hydrogenation of carbonyl compounds. One hypothesis is that the aldehydes adsorb more weakly on Pd-Fe bimetallic surface, resulting in a higher activity for hydrogenation of carbonyl groups.[86, 87, 101]

Furthermore, on the Pd_1Fe_3 catalyst, the hydrogenation rate for each molecule decreases in the order: propanal > furfural > xylose (Figure 4.5). For xylose hydrogenation, the O atom on the carbonyl group adsorbs on a catalyst surface through O along with an adsorption of O atom on the hydroxyl group adjacent to the carbonyl group on the catalyst surface.[84] This adsorbed O atom of the hydroxyl group may prevent hydrogenation of C=O bond of xylose. However, for propanal and furfural, the carbonyl group adsorbs on Pd metal surface through both C and O.[107, 126] For propanal hydrogenation, the adsorbed carbonyl species is hydrogenated to form a surface alkoxide species via the addition of adsorbed H to the adsorbed O atom.[107, 127, 128] In contrast to propanal, a hydroxyalkyl surface species is the dominant intermediate through H addition to C atom due to the conjugation with the furan ring of furfural.[107, 129] Atomic O is more electronegative than atomic C; hence, the alkoxide intermediate can more easily react with H than the hydroxyalkyl intermediate resulting in higher activity for hydrogenation of propanal than of furfural.

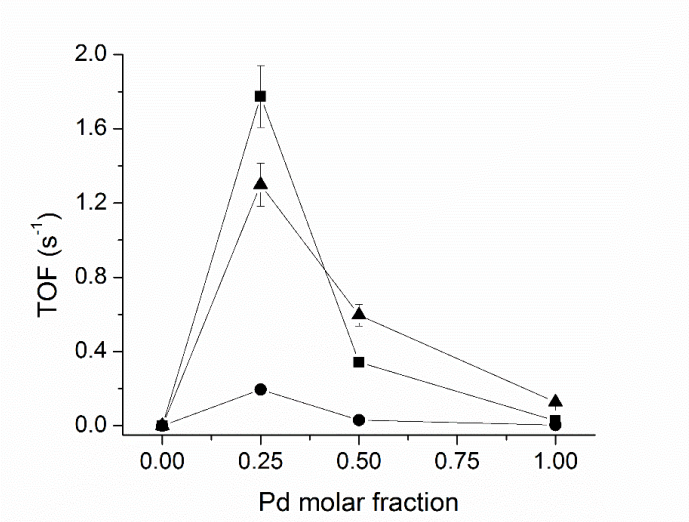

Figure 4.5 TOF of the APH of propanal, xylose, and furfural at 373 K as a function of Pd atomic fraction in Pd-Fe bimetallic system (■ propanal; ● xylose; ▲ furfural).

4.2.2 Aqueous-phase hydrodeoxygenation of sorbitol

As shown above, it is found that the addition of Fe to Pd increases the activity for APH of C=O bond. Hydrogenation of carbonyl groups is an important fundamental reaction in APHDO of biomass-derived oxygenates.[29, 38, 43] The carbonyl groups are produced during APHDO by several routes including dehydration of alcohols or polyols and C-C bond cleavage reactions.[38] For example, ethylene glycol is produced from hydrogenation of 2-hydroxyacetaldehyde which is produced through dehydrogenation and retro-aldol condensation of sorbitol.[38] Therefore, using a bimetallic Pd-Fe catalyst is an option to increase the catalytic activity for APHDO of sorbitol.

APHDO occurs through a bifunctional reaction pathway on metal-acid catalysts. Zirconium phosphate (Zr-P) is one of the most promising solid-acids for APHDO because it has a high Brønsted to Lewis acid ratio and does not leach during the reaction.[130, 131] Therefore, a Pd_1Fe_3/Zr-P catalyst was synthesized and APHDO of sorbitol was carried out with the Pd_1Fe_3/Zr-P catalyst in a continuous flow reactor.

Table 4.3 lists the BET surface area and hydrogen uptake of the 3 wt% Pd/Zr-P and Pd_1Fe_3/Zr-P catalysts before and after reaction. During the reaction both catalysts underwent phase transformation from an amorphous material to a crystalline material as shown by XRD in Figure A1. Both catalysts lost BET and metal surface area after reaction. Despite the loss of surface area, both catalysts were stable as shown by the time-on-stream data in Figure 4.6.

Table 4.3 BET surface area and hydrogen chemisorption data of Pd/Zr-P and Pd_1Fe_3/Zr-P.

Catalyst	BET surface area (m^2 g^{-1})	Hydrogen uptake (μmol g^{-1})
3 wt% Pd/Zr-P before reaction	238.0	19.3
3 wt% Pd/Zr-P after reaction	19.7	1.1
Pd_1Fe_3/Zr-P before reaction	102.3	16.4
Pd_1Fe_3/Zr-P after reaction	6.7	0.2

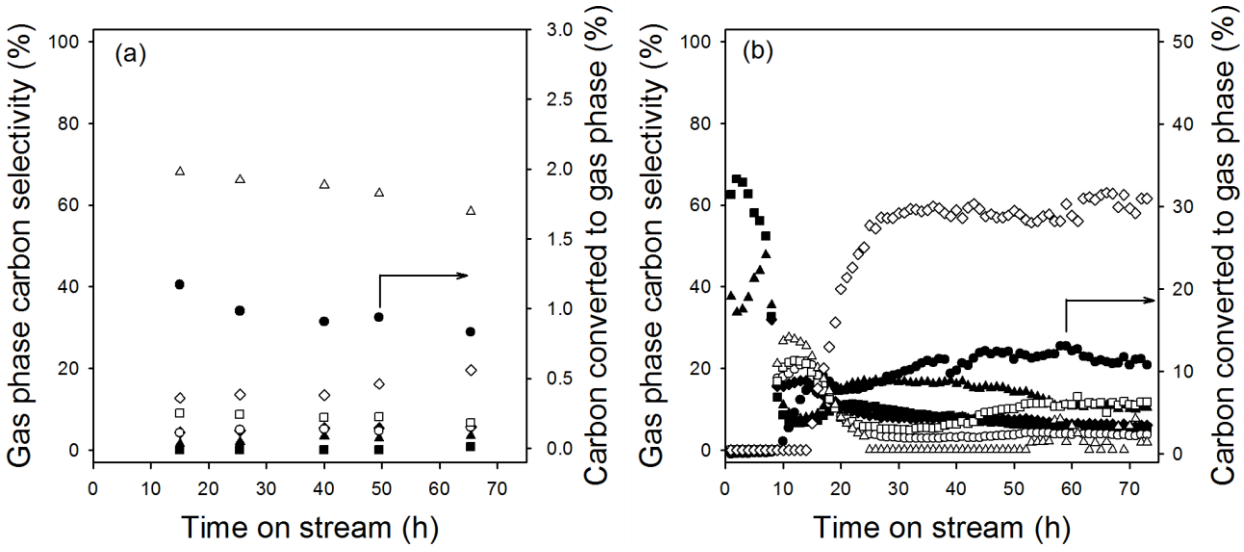

Figure 4.6 Carbon converted to gas phase (●) and gas phase carbon selectivity of C1 (■), C2 (▲), C3 (◆), C4 (○), C5 (□), C6 (△), and CO_2 (◇) as a function of time-on-stream over (a) Pd/Zr-P (WHSV = 0.73 h^{-1}) and (b) Pd_1Fe_3/Zr-P (WHSV = 0.16 h^{-1}). Reaction conditions: 518 K, 6.21 MPa, 20 wt% sorbitol solution as the feed, and hydrogen flow of 40 mL min^{-1}.

The Pd_1Fe_3/Zr-P was the most active catalyst we have tested for the APHDO of sorbitol, as shown in Figure 4.7.[38, 39, 52] The TOF of the Pd_1Fe_3/Zr-P (based on hydrogen uptake after reaction) was 14 times higher than the TOF of the Pd/Zr-P. The Pd_1Fe_3/Zr-P catalyst was 13 times more active than a Pt/Zr-P catalyst.[52] This suggests that hydrogenation of carbonyl groups is a kinetically slow step on Pd catalysts and carbonyl intermediates may poison the Pd surface.[98, 132, 133] Interactions between Pd and Fe shift the d-band center of Pd away from the Fermi level.[134] The change in the electronic structure of Pd weakens the adsorption strength of intermediates and products in APHDO facilitating product desorption, thereby increasing reaction rate.[135] Also, Pd promotes water formation over metallic Fe surface, preventing oxidation of the metallic Fe surface by surface oxygen species.[136] Pd is also known to stabilize the metallic Fe surface against deactivation by water oxidation.[120]

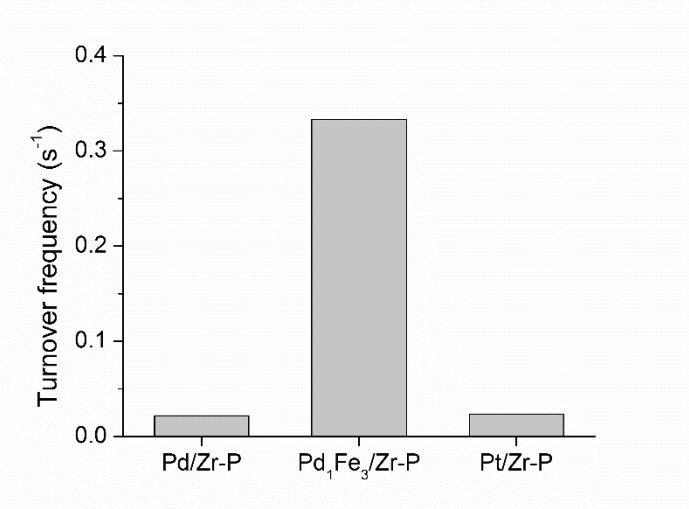

Figure 4.7 Comparison of TOFs of the APHDO of sorbitol. The values of the TOF of Pt/Zr-P is from the reference.[52] Reaction conditions: 518 K, 6.21 MPa, WHSV = 2.92 h^{-1}, 20 wt% sorbitol solution as the feed, and hydrogen flow of 40 mL min^{-1}.

Scheme 4.1 shows major reaction pathways for the APHDO of sorbitol. The APHDO of sorbitol involves three key classes of reactions:[29, 38, 53] (1) C-C bond cleavage through

dehydrogenation followed by decarbonylation and dehydrogenation followed by retro-aldol condensation at metal sites; (2) C-O cleavage through dehydration at acid sites; (3) hydrogenation at metal sites.

First, sorbitol undergoes stepwise dehydration to produce sorbitan and isosorbide. The sorbitan and isosorbide undergo a series of dehydration/hydrogenation reactions to produce polyols and cyclic ethers, respectively. The polyols and cyclic ethers undergo further dehydration/hydrogenation to produce alcohols, followed by the corresponding alkanes. Hydrogenation occurs rapidly, regardless of C-C and C-O bond cleavage. Dehydration is the rate-limiting step during dehydration/hydrogenation.[29, 137] The oxygenated intermediates probably also undergo dehydrogenation to produce the corresponding ketones and aldehydes. The aldehydes are selectively converted to their carboxyl acids through isomerization (or disproportionation). C-C bond cleavage reactions can also take place from the oxygenated intermediates, leading to smaller products and CO_2.

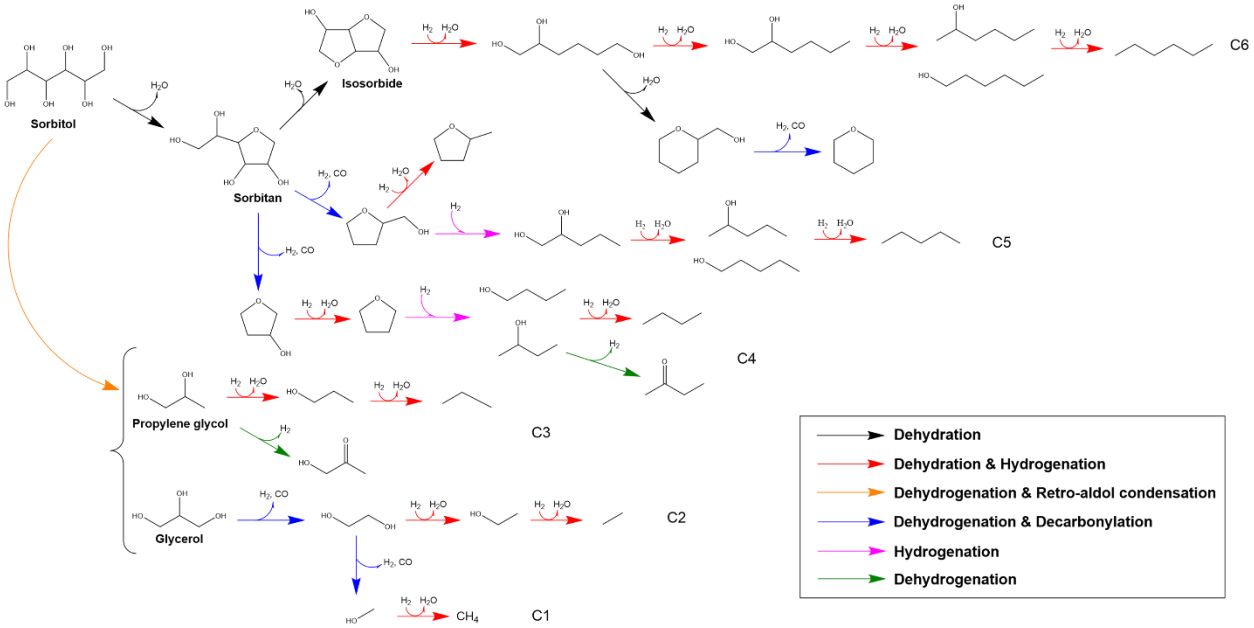

Scheme 4.1 Major reaction pathways and chemical reactions for APHDO of sorbitol.

As shown in Scheme 4.1, sorbitan and isosorbide which are produced through dehydration of sorbitol at acid sites of the Zr-P support are early intermediates of C4-C6 products for the APHDO of sorbitol. The products made through dehydrogenation/retro-aldol condensation of sorbitol (*i.e.*, propylene glycol and glycerol) are the intermediates of C1-C3 products for the APHDO of sorbitol. As shown in Figure 4.8, the Pd_1Fe_3/Zr-P had a significantly lower selectivity toward sorbitan and isosorbide than the Pd/Zr-P, thereby having a higher selectivity toward C4-C6 products than the Pd/Zr-P. This indicates that the addition of Fe to the Pd catalyst promotes the conversion of sorbitan and isosorbide to C4-C6 alcohols, cyclic ethers, and alkanes. Also, a selectivity toward C1-C3 products of the Pd_1Fe_3/Zr-P was higher than one of the Pd/Zr-P. This suggests that the addition of Fe to the Pd catalyst promotes C-C bond cleavage by dehydrogenation/retro-aldol condensation. The electronic structure change of Pd could alter the favorable reaction mechanism by changing the adsorption configuration.[138]

For both catalysts, a white insoluble product was observed in the liquid phase report as humins in Table 4.4. A less amount of humins was formed with the Pd_1Fe_3/Zr-P than with the Pd/Zr-P. The humins were formed via polymerization of isosorbide.[139]

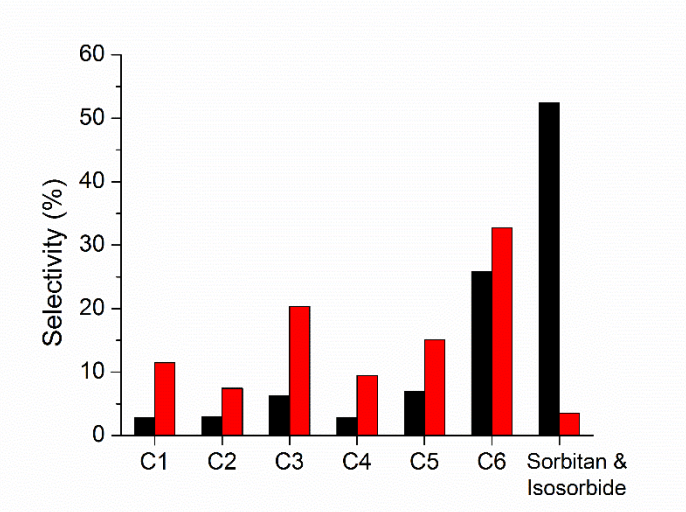

Figure 4.8 Molar carbon selectivity (normalized without polymerized humins) of C1-C6 products and of sorbitan and isosorbide (■ Pd/Zr-P; ■ Pd_1Fe_3/Zr-P). Reaction conditions: 518 K, 6.21 MPa, WHSV = 0.16 h^{-1}, 20 wt% sorbitol solution as the feed, and hydrogen flow of 40 mL min^{-1}.

Table 4.4 Molar carbon selectivity of products for the APHDO of sorbitol. Reaction conditions: 518 K, 6.21 MPa, WHSV = 0.16 h^{-1}, 20 wt% sorbitol solution as the feed, and hydrogen flow of 40 mL min^{-1}.

Catalyst	Pd/Zr-P	Pd_1Fe_3/Zr-P
Conversion (%)	97.8	100
Alcohols (%)		
Methanol	0.4	1.0
Ethanol	0.5	3.8
Ethylene glycol	1.1	0.3
1-Propanol	2.8	11.3
2-Propanol	0.02	0.4
Propylene glycol	0.1	1.1
Glycerol	0.2	0.3
1-Butanol	0.4	1.6
2-Butanol	0	0.3
1,2-Butanediol	0	0.4
1,4-Butanediol	0.1	0.3
2,3-Butanediol	0	1.0
1-Pentanol	0.1	0.8
2-Pentanol	0.1	0.2
1,2-Pentanediol	0.4	0.6
1,4-Pentanediol	0.04	0.5
1,5-Pentandiol	0.1	0.1
1-Hexanol	1.1	1.6

2-Hexanol	0.02	0.1
3-Hexanol	0.3	0.3
1,6-Hexanediol	0.1	0.1
2,5-Hexanediol	0	0.7
1,2,6-Hexanetriol	0.1	0.02
Cyclic ethers (%)		
THF	0.4	0.6
3-Hydroxy-THF	0.1	0.8
2-Methyl-THF	0.3	0.7
HMF	0	0
THFA	0.8	2.7
Tetrahydropyran	0.7	1.1
Tetrahydro-4H-pyran-4-ol	0.3	0.9
2,5-Dimethyl-THF	2.5	1.7
5-Methyl-THF-2-methanol	1.4	3.2
Tetrahydro-2-methoxymethyl-furan	0.7	2.2
2-Methyl-tetrahydropyran	3.4	2.8
Tetrahydropyran-2-methanol	5.0	9.5
Aldehydes (%)		
Butanal	0.1	0.1
Pentanal	0	0.6
Ketones (%)		
Acetone	0.03	0.7
Hydroxyacetone	0	0.2
2-Butanone	0.1	1.3
2-Pentanone	0.1	0.4
3-Pentanone	1.0	0.9
Cyclopentanone	0	0.1
2-Hexanone	0.1	0.3
3-Hexanone	0.1	0.6
Acids (%)		
Propanoic acid	0.3	0.5
Butylic acid	0.1	0.2
Pentanoic acid	0.2	0.3
Hexanoic acid	0.2	0.6
Alkanes (%)		
Methane	0.05	0.6
Ethane	0.2	1.4
Propane	0.5	0.8
Butane	0.5	0.4

Pentane	0.2	0.5
Hexane	1.0	0.5
CO (%)	0.6	1.5
CO_2 (%)	0.7	5.4
Isosorbide (%)	26.8	2.0
Sorbitan (%)	3.0	0.6
Mannitol (%)	3.0	0
Humins (%)	36.5	25.5

4.3 Conclusions

The addition of Ni, Co, or Fe to the monometallic Pd and Pt catalysts increased the activity for the APH of propanal and furfural. In contrast, all bimetallic catalysts tested in this study had a lower activity than the monometallic Ru catalyst for the APH of xylose. The TOF of the APH of propanal increased by the addition of Ni, Co, and Fe to the monometallic Pd catalyst with the bimetallic Pd_1Fe_3 catalyst being most active for the APH of propanal. The addition of Fe to the monometallic Pd catalyst also increased the TOF of the APH of xylose by a factor of 51. The Pd_1Fe_3 bimetallic catalyst has the highest activity for the APH of furfural. The Pd-based bimetallic catalysts produced not only furfuryl alcohol but also THFA for the APH of furfural, meaning that the Pd-based bimetallic catalysts are also active not only for hydrogenation of C=O bond of furfural but also for hydrogenation of C=C bonds of furan ring.

The Pd_1Fe_3/Zr-P catalyst was more active than the monometallic Pd/Zr-P and Pt/Zr-P catalysts for the APHDO of sorbitol. The addition of Fe to the Pd increased the conversion of sorbitan and isosorbide to C4-C6 products and promoted dehydrogenation/retro-aldol condensation of sorbitol causing the increase in the production of C1-C3 compounds.

CHAPTER 5

Stabilizing Cobalt Catalyst by Atomic Layer Deposition for Aqueous-Phase Reactions

J. Lee, D. H. K. Jackson, T. Li, R. E. Winans, J. A. Dumesic, T. F. Kuech and G. W. Huber, Enhanced Stability of Cobalt Catalysts by Atomic Layer Deposition for Aqueous-Phase Reactions, *Energy and Environmental Science*, 2014, **7**, 1657-1660.

5.1 Background

Aqueous-phase catalytic reactions are a common method to convert biomass into liquid fuels and chemicals.[6, 9, 14, 47, 140] Unfortunately, most of the catalysts used in these aqueous-phase reactions are precious metals like Pt and Ru.[29, 53, 75, 76] Precious-metal catalysts are active and stable under aqueous phase conditions,[52, 59, 74] but are expensive. While base metals are inexpensive, abundant, and active for liquid phase reactions,[141] they suffer from irreversible deactivation such as leaching of metal species under liquid-phase reaction conditions.[142, 143] Hence, it would be highly desirable to design stable base-metal catalysts for aqueous-phase catalytic processes.

Previous studies have shown that atomic layer deposition (ALD) of an Al_2O_3 overcoat can inhibit coking and sintering of Pd nanoparticles for a gas phase dehydrogenation reaction[144] and leaching and sintering of Cu for liquid-phase hydrogenation reactions.[145] ALD is a gas phase film deposition technique depending on discrete pulsing of chemical precursors for the film. Figure 5.1a-b shows the reaction of a metal precursor (A) with the substrate (the first half reaction), in which the reactive ligands of the metal precursor are partially removed by reaction with active sites on the substrate surface. In Figure 5.1b-c, the metal precursor pulse is stopped and unreacted precursor and byproducts are purged with an inert gas or evacuated when the first half reaction completes. Figure 5.1c-d represents the second half reaction (precursor B) removing the remaining ligands of the precursor A, regenerating the active sites, and completing the reaction cycle. In Figure 5.1d-e, the ALD reactor purged with the inert gas or evacuated after the completion of the surface reaction. The cycle is repeated until the desired film thickness is obtained (Figure 5.1f). The self-limiting nature of the half-reactions allows conformal film deposition and film thickness control.[150, 151]

In this chapter, an ALD TiO_2 coating is used to stabilize cobalt catalysts for APH reactions.

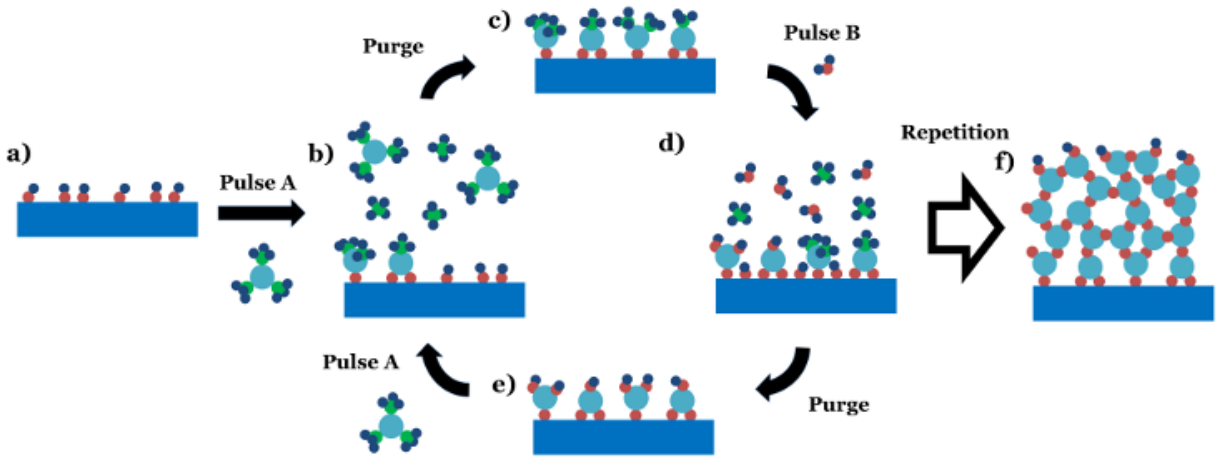

Figure 5.1 Schematic representation of film ALD using a binary (AB) precursor system.

5.2 Results and Discussion

5.2.1 Catalyst characterization

A high-temperature calcination treatment is required in preparing ALD catalyst to produce porosity in the ALD coating, thereby allowing access to the metal catalytic sites.[144, 145] As shown in Figure 5.2b, the ALD Al_2O_3/Co/γ-Al_2O_3 catalysts were not reducible in a hydrogen environment at temperatures up to 1073 K after a calcination treatment. The ALD Al_2O_3/Co/γ-Al_2O_3 catalyst most likely formed an irreducible cobalt aluminate phase after the high-temperature calcination,[146, 147] showing no activity for the APH of furfuryl alcohol. After the high-temperature calcination, the color of the calcined Co/γ-Al_2O_3 and ALD Al_2O_3/Co/γ-Al_2O_3 catalysts became blue. Blue is the color of cobalt aluminate.[148]

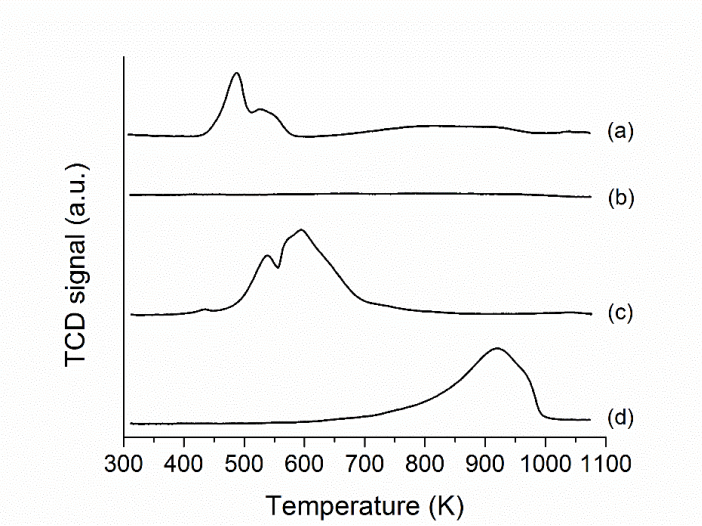

Figure 5.2 TPR patterns of (a) Co/γ-Al_2O_3, (b) Al_2O_3/Co/γ-Al_2O_3 calcined at 873 K, (c) Co/TiO_2, and (d) ALD TiO_2/Co/TiO_2 calcined at 873 K.

An ALD TiO_2 coated Co/TiO_2 (ALD TiO_2/Co/TiO_2) catalyst reduced at 873 K after calcination at 873 K were then prepared. The growth per cycle (GPC) of TiO_2 coating is 0.4 Å/cycle,[149] meaning that the thickness of the TiO_2 coating (30 cycles) is around 1.2 nm. Using this film thickness and the surface area, it was calculated a ~5 % increase in mass during the ALD treatment. This value was confirmed experimentally by weighing the sample before and after deposition, indicating that the addition of cobalt to the TiO_2 surface did not dramatically reduce or increase the ALD of TiO_2.

Table 5.1 shows the hydrogen chemisorption, percent reducibility, and BET surface area of the different catalysts. The hydrogen uptake of Co/TiO_2 was 7.38 μmol g^{-1}. After the ALD TiO_2 coating of the Co/TiO_2, the hydrogen uptake decreased to 0.73 μmol g^{-1}, indicating that the thin ALD TiO_2 coating covered 90.1 % of cobalt active sites. The hydrogen uptake increased to 2.01 μmol g^{-1} after a calcination treatment at 873 K in air, indicating more cobalt sites being accessible after the calcination. The hydrogen uptake of the used ALD TiO_2/Co/TiO_2 was 2.79 μmol g^{-1}, and thus more cobalt active sites were exposed after the regeneration. The BET surface area slightly

decreased after the ALD TiO_2 coating. The BET surface area increased after high temperature calcination.

Table 5.1 Hydrogen uptake, extent of reduction, and BET surface area of the TiO_2, Co/TiO_2, and ALD $TiO_2/Co/TiO_2$.

Material	Hydrogen uptake ($\mu mol\ g^{-1}$)	Extent of reduction (%)	BET surface area ($m^2\ g^{-1}$)
TiO_2	-	-	51.4
TiO_2-1023	-	-	10.2
Co/TiO_2	7.38	41.7[(a)]	10.1
ALD $TiO_2/Co/TiO_2$	0.73	-	9.9
ALD $TiO_2/Co/TiO_2$ calcined at 873 K	2.01	38.4[(b)]	10.6
ALD $TiO_2/Co/TiO_2$ used[(c)]	2.79	-	8.6

[(a)]measured at 473~773 K
[(b)]measured at 723~998 K
[(c)]Before the characterization, the used ALD $TiO_2/Co/TiO_2$ calcined at 873 K, reduced at 873 K, and then passivated in 10 % oxygen.

The effect of TiO_2 coating on thermal stability of cobalt particles was determined by TEM analysis as shown in Figure 5.3. The fresh cobalt particle size of the Co/TiO_2 was 25 ± 4 nm (Figure 5.3a and e). After calcination at 873 K, the cobalt particle size of the Co/TiO_2 increased (32 ± 6 nm, Figure 5.3b and e) with a broader particle size distribution. However, the cobalt particle size of the ALD $TiO_2/Co/TiO_2$ (24 ± 2 nm) did not change even after calcination, three reactions, and two regenerations (Figure 5.3c, d, and e). This confirms that 30 cycles of ALD TiO_2 coating (1.2 nm thickness) can suppress cobalt sintering. It is known that leaching and sintering of metal come from the under-coordinated metal atoms at defects, corners, and edges.[145, 150] In the ALD $TiO_2/Co/TiO_2$ catalyst, the thin TiO_2 film probably decorates the under-coordinated cobalt sites located at defects, corners, and edges which thereby prevents the leaching and sintering of cobalt.

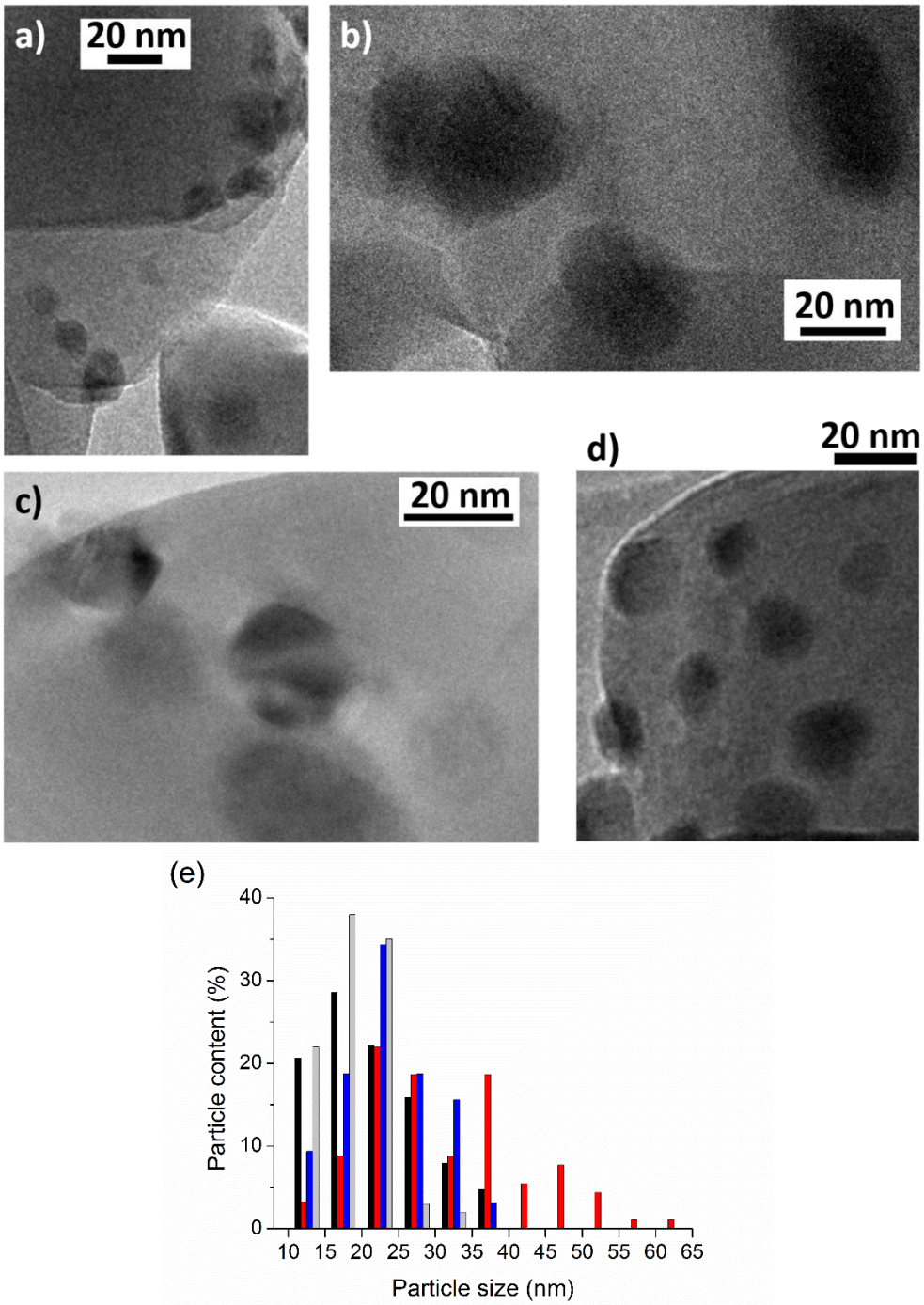

Figure 5.3 TEM images of (a) Co/TiO_2, (b) Co/TiO_2 calcined at 873 K, (c) ALD $TiO_2/Co/TiO_2$ calcined at 873 K, (d) the used ALD $TiO_2/Co/TiO_2$, and (e) cobalt particle size distribution (■ Co/TiO_2; ■ Co/TiO_2 calcined at 873 K; ■ ALD $TiO_2/Co/TiO_2$ calcined at 873 K; ■ the used ALD $TiO_2/Co/TiO_2$). The used catalyst calcined at 873 K and then reduced at 873 K after reaction.

The ALD $TiO_2/Co/TiO_2$ catalyst was further characterized by small-angle X-ray scattering (SAXS).[151] As shown in Figure 5.4, there was a difference in intensity at the *q* range of 0.01 to

0.07 $Å^{-1}$ between the ALD TiO_2/Co/TiO_2 catalyst before (blue curve) and after calcination (red curve). This intensity difference (black curve) is possibly due to structural change either of the support or of the overcoat before and after calcination. *In-situ* SAXS showed that the support is stable and no change in intensity took place during calcination (Figure 5.5). Therefore, the difference in intensity shown in Figure 5.4 indicates pore formation in the overcoat. The data was fitted with a spherical shape model using Modeling II tool in the Irena package within the IgorPro application.[152] From the data fitting (green curve), the average pore size in the ALD TiO_2 coating was estimated to be around 16 nm based on volume distribution.

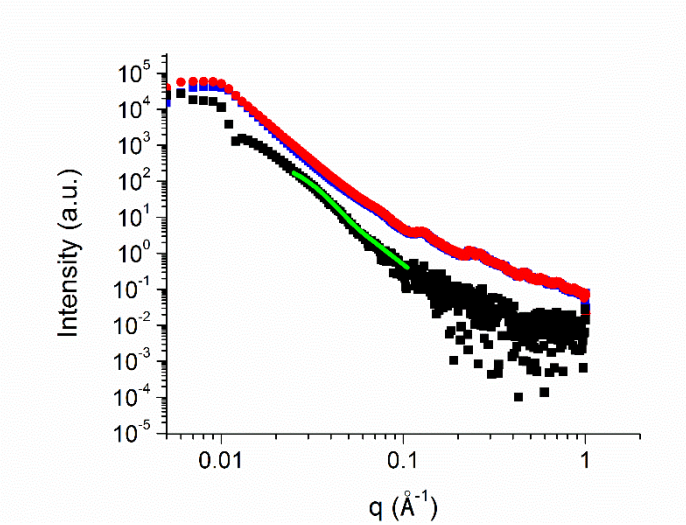

Figure 5.4 SAXS results for the ALD TiO_2/Co/TiO_2 before (■ blue curve) and after calcination at 873 K (● red curve). The intensity difference (■ black curve) subtracts blue curve from red curve. Green curve (●) shows data fitting.

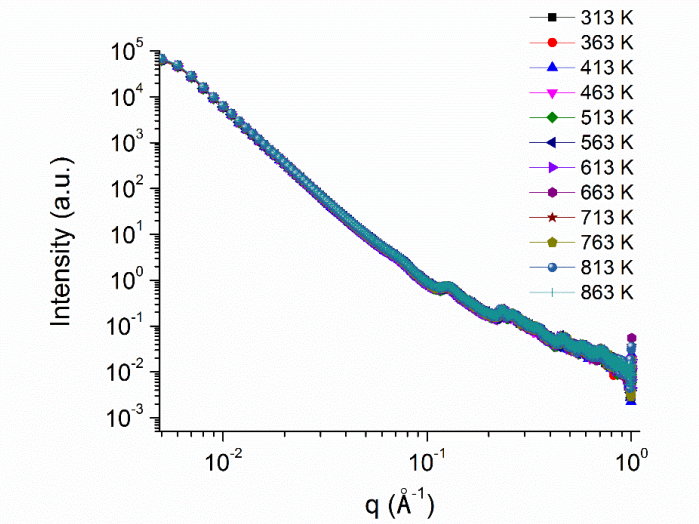

Figure 5.5 *In situ* SAXS data of the TiO_2 support.

XRD was performed to understand how pores were formed in the overcoat during calcination. Two amorphous peaks were observed (marked with red star in Figure 5.6) prior to calcination. These peaks did not match with any other peaks in our database. These two peaks disappeared after calcination (black dashed line in Figure 5.6). This suggests that pore formation resulted from densification of an amorphous TiO_2 coating to a crystallized TiO_2 during calcination.[153]

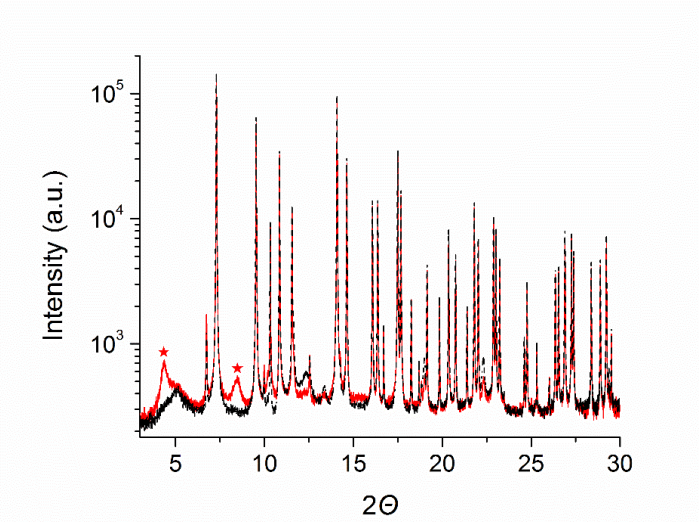

Figure 5.6 XRD patterns of the fresh ALD TiO_2/Co/TiO_2 before and after calcination at 873 K (red solid line: before calcination; black dashed line: after calcination at 873 K).

Figure 5.7 represents a proposed schematic model of a Co/TiO_2 catalyst with and without ALD TiO_2 decoration on edges. The TiO_2 forms a thin film over the cobalt particle during the ALD process. After calcination, the TiO_2 forms pores and migrates to defect sites on the cobalt particles.

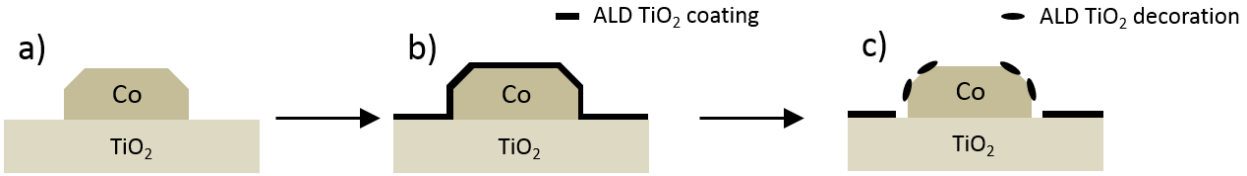

Figure 5.7 Proposed schematic model of a Co/TiO_2 catalyst with and without ALD TiO_2 decoration on edge. (a) Co/TiO_2, (b) ALD $TiO_2/Co/TiO_2$, and (c) ALD $TiO_2/Co/TiO_2$ after calcination.

5.2.2 Catalyst testing

The $Co/\gamma\text{-}Al_2O_3$, Co/TiO_2, and ALD $TiO_2/Co/TiO_2$ catalysts were tested for the APH of furfuryl alcohol in a continuous flow reactor. Furfuryl alcohol is a key platform renewable non-petroleum based molecule.[154, 155] Precious-metal catalysts have been used for hydrogenation of furfuryl alcohol.[74, 156] Therefore, hydrogenation of furfuryl alcohol would benefit from stabilizing inexpensive cobalt catalysts. Figure 5.8 shows the cobalt leaching as a function of time on stream for the APH of furfuryl alcohol with three different catalysts. As can be seen from Figure 5.8, the $Co/\gamma\text{-}Al_2O_3$ and Co/TiO_2 lost cobalt by leaching. In contrast, both the fresh and regenerated ALD $TiO_2/Co/TiO_2$ catalysts did not lose cobalt.

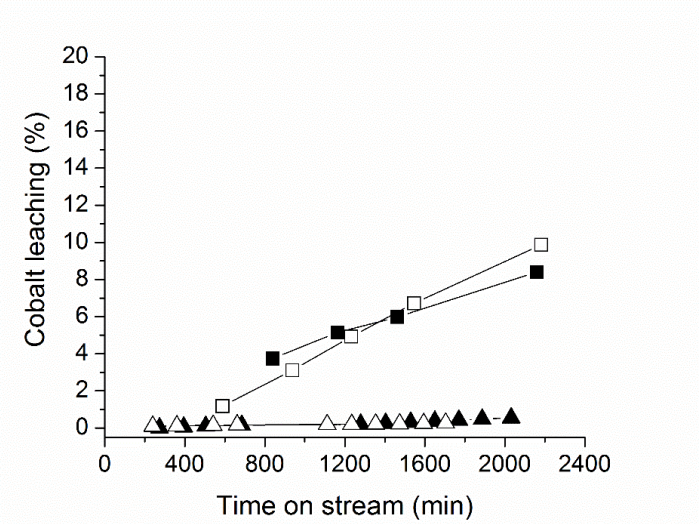

Figure 5.8 Cobalt leaching as a function of time-on-stream for the APH of furfuryl alcohol over ALD and non-ALD catalysts (▲ ALD $TiO_2/Co/TiO_2$ (fresh); △ ALD $TiO_2/Co/TiO_2$ (two regenerations); ■ $Co/\gamma\text{-}Al_2O_3$; □ Co/TiO_2). Reaction conditions: 413 K, 2.34 MPa, WHSV = 5.8 h^{-1}, 2 wt% furfuryl alcohol solution as the feed, and hydrogen flow of 40 mL min^{-1}. Regeneration of the catalyst was carried out by calcining the catalyst at 873 K and then re-reducing the catalyst at 873 K.

Figure 5.9 shows the conversion of furfuryl alcohol as a function of time-on-stream. The Co/TiO_2 and $Co/\gamma\text{-}Al_2O_3$ catalyst had almost a five times lower activity compared to the regenerated ALD $TiO_2/Co/TiO_2$ catalyst. The fresh ALD $TiO_2/Co/TiO_2$ catalyst deactivated during the first reaction cycle and stabilized at a conversion of 25 %. However, after regeneration (regeneration of the catalyst after reaction was carried out by oxidizing the catalyst at 873 K, purging with helium, and then re-reducing the catalyst at 873 K), the ALD $TiO_2/Co/TiO_2$ catalyst showed higher activity than the fresh catalyst. This increase is due to more cobalt active sites being exposed by more pores formed in the ALD TiO_2 coating during regeneration as measured by hydrogen chemisorption (Table 5.1). After a second regeneration and reaction cycle the catalyst activity did not change.

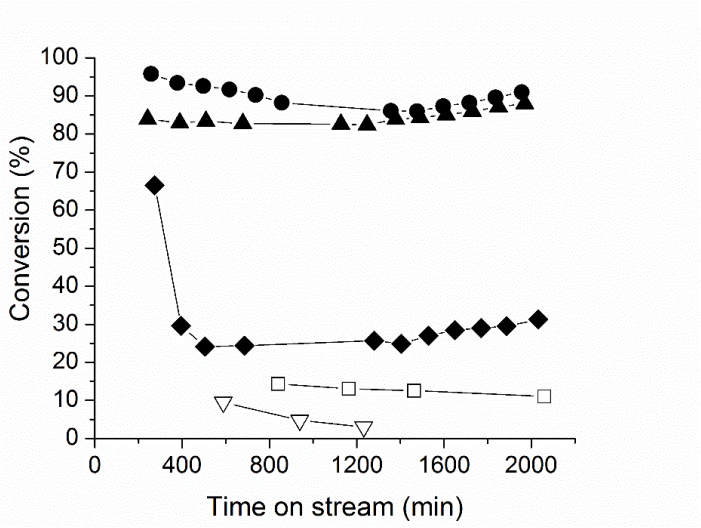

Figure 5.9 Conversion of furfuryl alcohol as a function of time-on-stream for the APH of furfuryl alcohol over ALD and non-ALD catalysts (◆ ALD TiO_2/Co/TiO_2 (fresh); ● ALD TiO_2/Co/TiO_2 (one regeneration); ▲ ALD TiO_2/Co/TiO_2 (two regenerations); ▽ Co/TiO_2; □ Co/γ-Al_2O_3). Reaction conditions: 413 K, 2.34 MPa, WHSV = 5.8 h^{-1}, 2 wt% furfuryl alcohol solution as the feed, and hydrogen flow of 40 mL min^{-1}. Regeneration of the catalyst was carried out by calcining the catalyst at 873 K and then re-reducing the catalyst at 873 K.

The APH of furfuryl alcohol produced several different products with the ALD TiO_2/Co/TiO_2, as shown in Scheme 5.1. THFA is produced via hydrogenation of the C=C bond of furan ring of furfuryl alcohol. 1,2-Pentanediol is converted from furfuryl alcohol via hydrogenolysis of C-O-C bond which occurs mostly on metal sites[157] whereas 1,5-pentanediol is produced on bifunctional sites.[158] 1,4-Pentanediol can be produced from isomerization of 1,2-pentanediol.[159] Ring rearrangement of furfuryl alcohol makes hydroxy-cyclopentenone as an intermediate in water.[160, 161] Hydrogenation of C=C and C=O bonds of the intermediate occurring on metal sites can produce 1,3-cyclopentanediol. The intermediate also undergoes hydrogenolysis of C-OH bond and hydrogenation of C=C bond, thereby produces cyclopentanone.[161] Cyclopentanol is produced through hydrogenation of C=O bond of the cyclopentanone.[161] 2-Methylfuran can be produced through hydrogenolysis the C-OH bond of furfuryl alcohol which has been reported to occur on metal sites of the catalysts.[108] 1-Pentanol and 2-Pentanol are formed

in a ring-opening reaction of the furan ring of the 2-methyfuran.[108] When the 2-pentanol undergoes C-C bond cleavage reactions on metal sites,[74] it produces 1-butanol and methane.

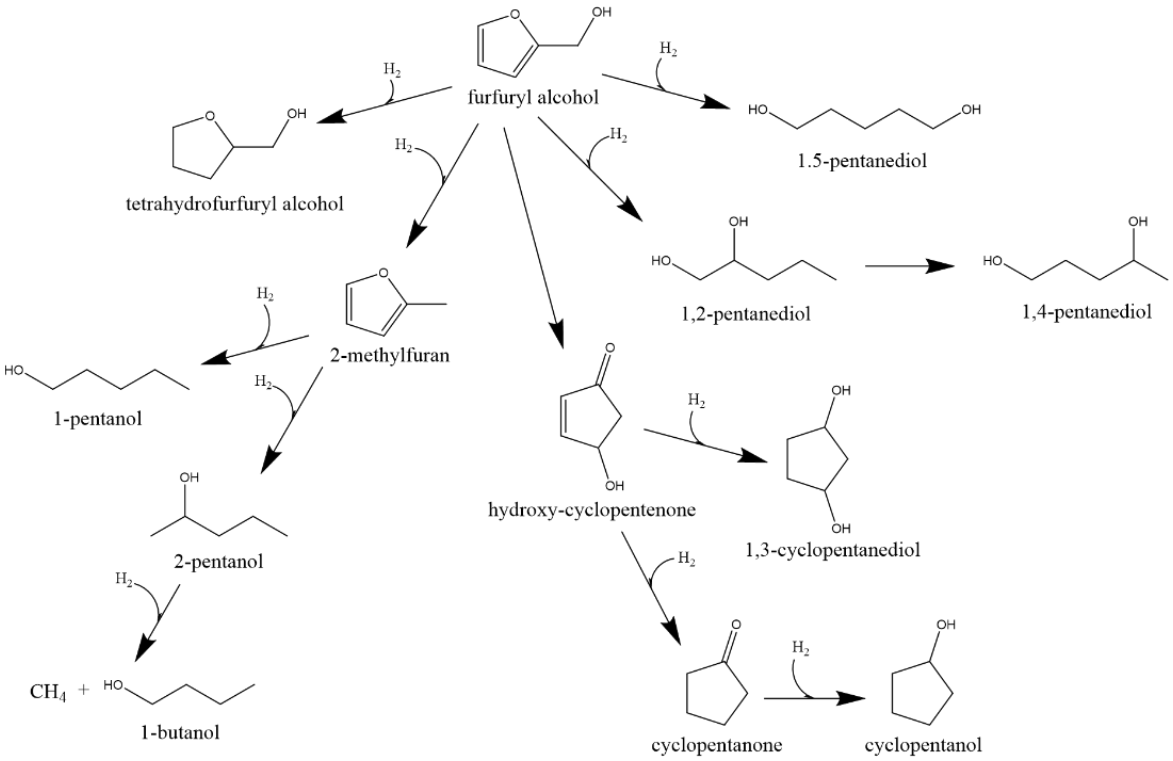

Scheme 5.1 Proposed reaction pathways for APH of furfuryl alcohol.

The main products made with the ALD $TiO_2/Co/TiO_2$ for the APH of furfuryl alcohol were THFA and 1,5-pentanediol (Figure 5.10). The THFA selectivity increased with each regeneration cycle. The cyclopentanone selectivity decreased while cyclopentanol selectivity stayed the same after the first regeneration, indicating ring rearrangement reactions became less dominant after regeneration. 1,5-Pentanediol is known to be produced from C-O-C bond hydrogenolysis of THFA.[158] Interestingly, even though 1,5-pentanediol was produced from the APH of furfuryl alcohol, there was no conversion for hydrogenolysis of THFA over the ALD $TiO_2/Co/TiO_2$. This suggests that 1,5-pentanediol and THFA are produced by parallel reactions for the APH of furfuryl

alcohol over the ALD TiO_2/Co/TiO_2 catalyst. 1,4-Pentanediol can be produced from isomerization of 1,2-pentanediol.[159]

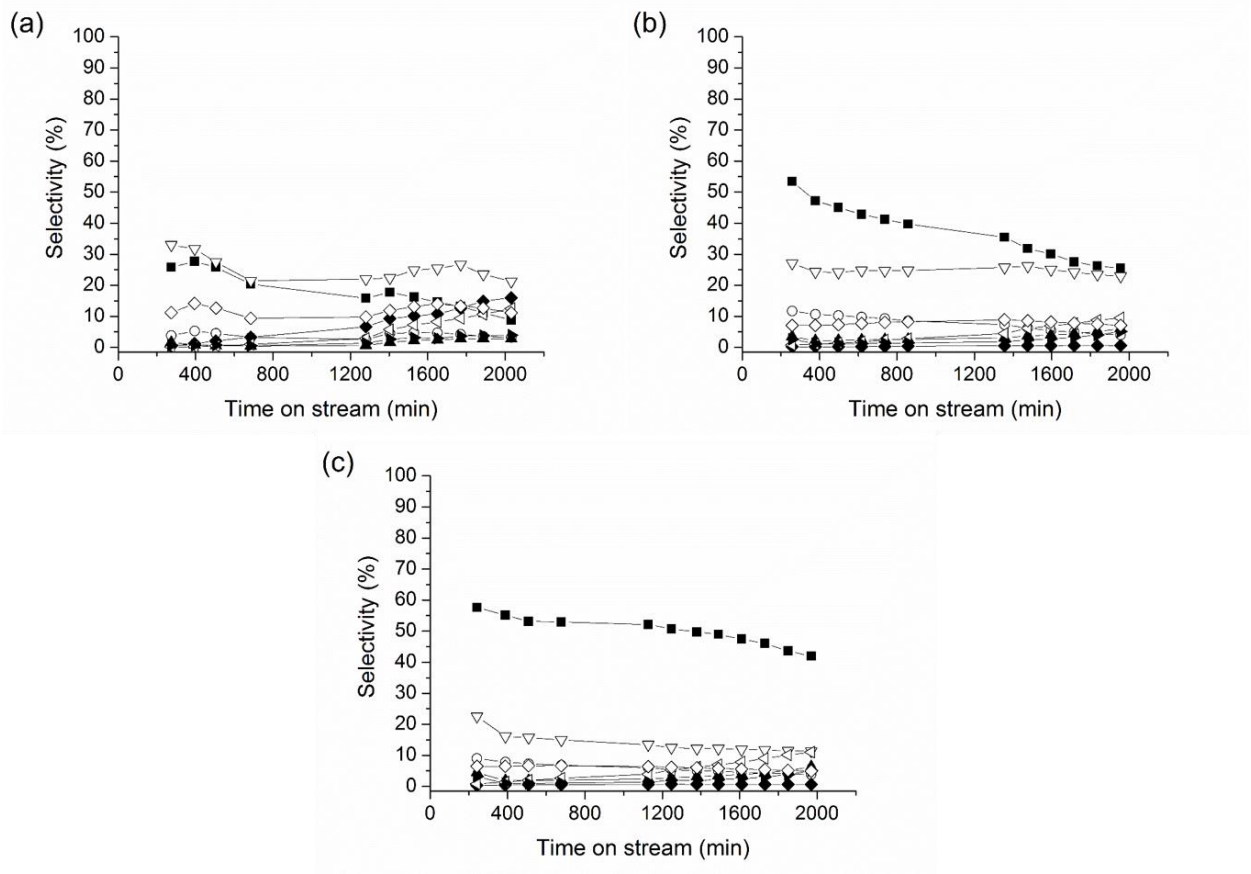

Figure 5.10 Carbon molar selectivity as a function of time-on-stream for the APH of furfuryl alcohol over (a) ALD TiO_2/Co/TiO_2 (fresh), (b) ALD TiO_2/Co/TiO_2 (one regeneration), and (c) ALD TiO_2/Co/TiO_2 (two regenerations) (■ THFA; ○ 1,2-pentanediol; ▲ 1,4-pentanediol; ▽ 1,5-pentnaediol; ◆ cyclopentanone; ◁ cyclopentanol; ▶ 1,3-cyclopentanediol; ◇ others). Others include 1-butanol, 2-methyl-furan, 1-pentanol, and 2-pentanol. Reaction conditions: 413 K, 2.34 MPa, WHSV = 5.8 h^{-1}, 2 wt% furfuryl alcohol solution as the feed, and hydrogen flow of 40 mL min^{-1}. Regeneration of the catalyst was carried out by calcining the catalyst at 873 K and then re-reducing the catalyst at 873 K.

5.3 Conclusions

It was shown that an ALD TiO_2 overcoat stabilized cobalt particles against leaching and sintering in the aqueous phase. High-temperature calcination exposed the cobalt by opening the overcoating, shown by hydrogen chemisorption, SAXS, and XRD, while maintaining a stabilizing interaction with under-coordinated cobalt sites that are prone to leaching and sintering. This strategy for base-metal stabilization under aqueous conditions should be useful in replacing novel-metal catalysts with inexpensive and abundant base-metal catalysts for aqueous-phase conversion of biomass.

CHAPTER 6

Stabilizing Cobalt Catalyst by Strong Metal-Support Interaction for Aqueous-Phase Reactions

6.1 Background

Catalytic aqueous-phase hydroprocessing approaches can be used to produce a wide variety of liquid fuels and commodity chemicals from biomass.[4, 6, 9, 14, 140, 162] Aqueous-phase processing has been primarily carried out with supported precious-metal catalysts. Dumesic and co-workers produced alkanes from aqueous-phase conversion of carbohydrates using Pt catalysts.[29, 30] Alkanes can also be prepared from cellulose using Ir-Re and Ru catalysts.[31, 32] Ru and Pt catalysts have been used for aqueous-phase hydrogenation of carbohydrates and organic acids.[33-35] Mono-functional organic compounds can be prepared from sugar alcohols using Pt-Re catalysts.[36, 37]

There have been efforts to use base-metal catalysts for these processes. It is generally known that base-metal catalysts leach and sinter under harsh aqueous conditions.[142, 143] Sulfided Co-Mo catalysts have been used for hydrodeoxygenation of pyrolysis oils.[163, 164] However, these catalysts deactivate due to coking and sulfur loss. Leaching of promoter metals (*e.g.*, Mo) is another problem when using the Mo-modified catalysts.[165] Other authors have used base-metal catalysts for aqueous-phase conversion of lignin and cellulose in batch reactors.[166, 167] However, the long term catalyst stability in these batch reactors was not determined. Raney Ni catalysts have also been used to upgrade bio-oils by hydrogen transfer reactions.[168, 169] However, the Raney catalysts are known to undergo metal leaching.[33, 84, 170] Therefore, it would be highly desirable to stabilize inexpensive supported non-sulfide base-metal catalysts for the aqueous-phase processes.

It has recently reported that base-metal catalysts can be stabilized by overcoating with a layer of Al_2O_3 or TiO_2 using ALD.[145, 171] An Al_2O_3 overcoat formed by ALD stabilized the copper particles against leaching and sintering for liquid-phase hydrogenation reactions.[145] An ALD TiO_2 overcoated cobalt catalyst was resistant against leaching and sintering for APH reactions where it was proposed that the TiO_2 selectively decorated defect and edge cobalt sites where leaching and

sintering begins, as shown in Chapter 5.[171] The ALD approach has also been used to stabilize Pd catalyst against coking and sintering for gas-phase ethane dehydrogenation at 948 K.[144] However, ALD is an expensive and time-intensive process to produce supported metal catalysts. It would be highly desirable to prepare stabilized base-metal catalysts without using ALD technology. The so-called strong metal-support interaction (SMSI) effect has been reported to be due to migration of partially reduced metal oxide species onto the surface of metal particles.[172-176] Dumesic *et al.* monitored the changes in physical and chemical properties of a Ni-TiO_2 system during reaction in hydrogen using TEM.[177] Zander *et al.* have recently observed the formation of a ZnO layer covering copper particles upon reduction by means of a depth-sensitive synchrotron X-ray photoelectron spectroscopy (XPS).[178] The SMSI effect has been used to design catalysts for methanol synthesis on Cu-based catalysts,[178] CO oxidation on Pd-based catalysts,[179] hydrogen production on Pt-based catalysts,[180] furfural hydrogenation on Pt-based catalysts,[181] and CO and CO_2 hydrogenation on Co-based catalysts.[182] However, previous studies have focused on enhancing activity and/or selectivity for the gaseous-phase reactions.

Herein, we show that the SMSI effect can be used to stabilize a Co/TiO_2 catalyst under aqueous-phase reaction conditions. High-temperature calcination and reduction treatments of a Co/TiO_2 catalyst create overcoats of TiO_x on cobalt particles by SMSI, protecting the cobalt particles against leaching and sintering in the aqueous phase. The SMSI effect also creates bifunctionality in the Co/TiO_2 system, which can be used to produce values-added commodity chemicals from renewable feedstocks. This is the first report of a highly stable and selective supported base-metal catalyst prepared using SMSI for aqueous-phase hydrogenation and hydrogenolysis of oxygenates.

6.2 Denotation of Catalyst

A batch of the Co/TiO_2 catalyst was directly reduced at temperatures of 723 and 873 K, without a 2nd calcination treatment. They are denoted as Co/TiO_2 723 R and Co/TiO_2 873R. A second batch of the Co/TiO_2 catalyst was calcined at 673 K (*i.e.*, 2nd calcination at 673 K) and then reduced at different temperatures of 723 and 873 K, labeled as Co/TiO_2 673C-723R and Co/TiO_2 673C-873R respectively. A third batch of the Co/TiO_2 catalyst was calcined at 873 K (*i.e.*, 2nd calcination at 873 K) and then reduced at 873 K, called Co/TiO_2 873C-873R.

6.3 Results and Discussion

6.3.1 Catalyst characterization

STEM images (Figure 6.1) show decoration of metallic cobalt particles by a thin layer that is blurry on the fringes of the cobalt particle. The blurriness is not observed with pure metallic particles indicating that a TiO_2 layer is forming over the cobalt catalysts. This has also previously been observed by de la Peña O'Shea *et al.* who observed cobalt particles covered by a TiO_2 layer using energy-dispersive X-ray spectroscopy (EDX).[183] The thickness of the layer can be measured from the STEM images. Adding a 2nd calcination step caused a statistical significantly increase (95 % confident limit using the student's *t*-test) in the size of the layer from 2.8 ($\pm$ 0.18) nm for the Co/TiO_2 873R catalyst to 3.5 ($\pm$ 0.2) nm for the Co/TiO_2 673C-873R catalyst. Increasing the 2nd calcination temperature from 673 to 873 K also significantly increased the size of the layer from 3.5 ($\pm$ 0.2) to 4.0 ($\pm$ 0.15) nm. Chemisorption results presented in Table 6.1 showed that the catalyst does adsorb hydrogen even after calcination and reduction at 873 K. This indicates that the cobalt surface sites are still accessible despite the overlayer.

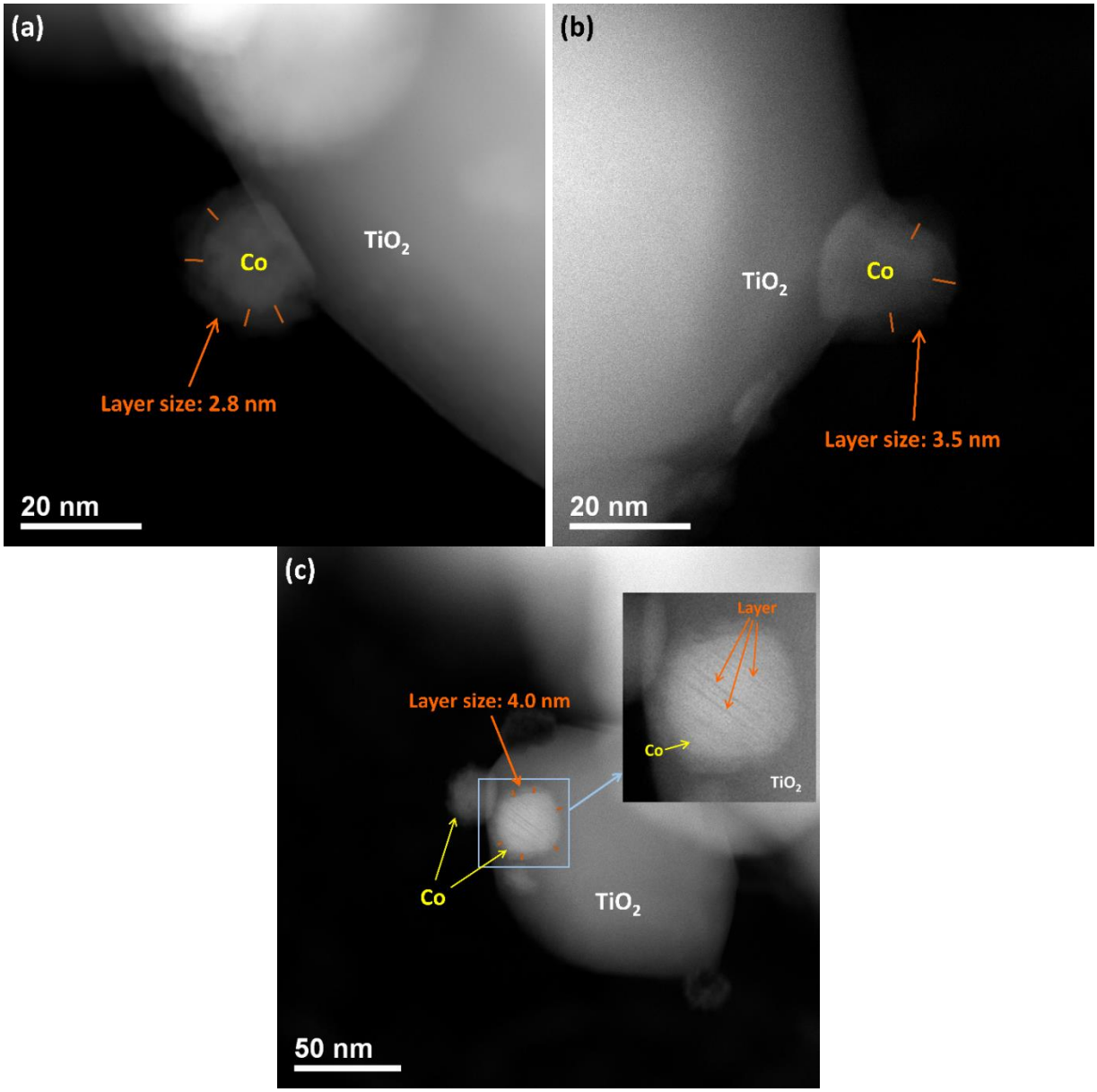

Figure 6.1 STEM images of (a) Co/TiO_2 873R, (b) Co/TiO_2 673C-873R, and (c) Co/TiO_2 873C-873R.

Table 6.1 Cobalt particle size, dispersion, hydrogen uptake, and BET surface area of the Co/TiO_2 catalysts with different treatments.

Catalyst	Cobalt particle size[(a)] (nm)	Dispersion[(b)] (%)	Hydrogen uptake[(c)] (μmol H g^{-1})	Dispersion[(d)] (%)	BET surface area (m^2 g^{-1})
Co/TiO_2 723R	17.0 ± 5.4	6.3 ± 2.1	16.70	4.7	10.1
Co/TiO_2 673C-723R	17.6 ± 5.3	6.1 ± 1.9	11.88	6.3	11.4
Co/TiO_2 873R	17.7 ± 5.4	6.1 ± 1.9	15.58	4.4	10.2
Co/TiO_2 673C-873R	18.8 ± 5.7	5.7 ± 1.8	10.28	5.4	11.7
Co/TiO_2 873C-873R	20.2 ± 6.2	5.3 ± 1.7	7.38	3.9	11.8

[(a)]Cobalt particle size measured by TEM

[(b)]Cobalt dispersion estimated based on cobalt particle size measured by TEM

[(c)]Hydrogen uptake determined by static hydrogen chemisorption

[(d)]Cobalt dispersion estimated based on hydrogen uptake and reducibility

The cobalt particle size of the Co/TiO_2 catalyst as measured by TEM ranged from 17 (± 5.4) to 20.2 (± 6.2) nm (Table 6.1 and Figure 6.3). The cobalt particle size of the Co/TiO_2 723R and the Co/TiO_2 673C-723R were not significantly different based on student's *t*-test at 95 % confident limit. In the case of the Co/TiO_2 873R and the Co/TiO_2 673C-873R, there was also no statistically significant change in the cobalt particle size. However, there was a statistically siginificant difference in the cobalt particle size between the Co/TiO_2 673C-873R and the Co/TiO_2 873C-873R. The particle size growth during the 2nd calcination at 873 K is due to agglomeration of cobalt.[184] The hydrogen uptake decreased with an increase in calcination temperature. This is mainly due to the partially reduced TiO_2 species covering cobalt sites. This is similiar to our previous results that showed a decrease in hydrogen uptake when a TiO_2 overcoat was added to a Co/TiO_2 catalyst by ALD.[171] The cobalt dispersion estimated from the cobalt particle size matches with the dispersion estimated from hydrogen uptake and the extent of reduction (Table 6.1).

Increasing the calcination temperature caused the cobalt to reduce at higher temperature, as shown in Figure 6.2. The extent of reduction of the Co/TiO_2 decreased with increasing

calcination temperature (Table 6.2). The decrease in the extent of reduction and shift in reduction peaks indicates that an interaction between cobalt oxide and support exists at increasing calcination temperature.[176, 185] The extent of reduction decreased when a TiO_2 was overcoated by ALD over the surface of a Co/TiO_2 catalyst.[171] The hydrogen chemisorption and TPR results indicate that the TiO_2 encapsulation of cobalt particles by SMSI and ALD are similiar.

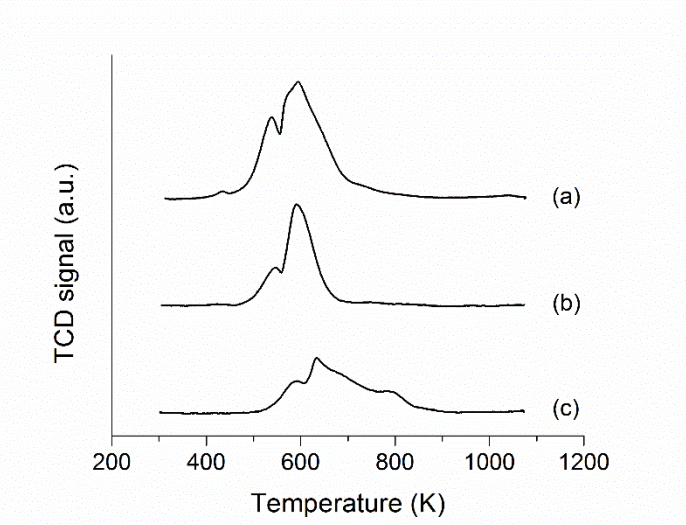

Figure 6.2 TPR patterns of the Co/TiO_2 after different 2nd calcination temperatures. (a) No 2nd calcination, (b) 2nd calcination at 673 K, and (c) 2nd calcination at 873 K.

Table 6.2 Extent of reduction of the Co/TiO_2 with different calcination treatments.

Catalyst	Extent of reduction[(a)]
Co/TiO_2 no 2nd calcination	41.7 % (420 - 710 K)
Co/TiO_2 after 673 K calcination	22.4 % (480 - 710 K)
Co/TiO_2 after 873 K calcination	22.3 % (480 - 900 K)

[(a)]Reducibility based on hydrogen consumption from TPR and theoretical hydrogen consumption assuming that Co_3O_4 is completely reduced to Co.

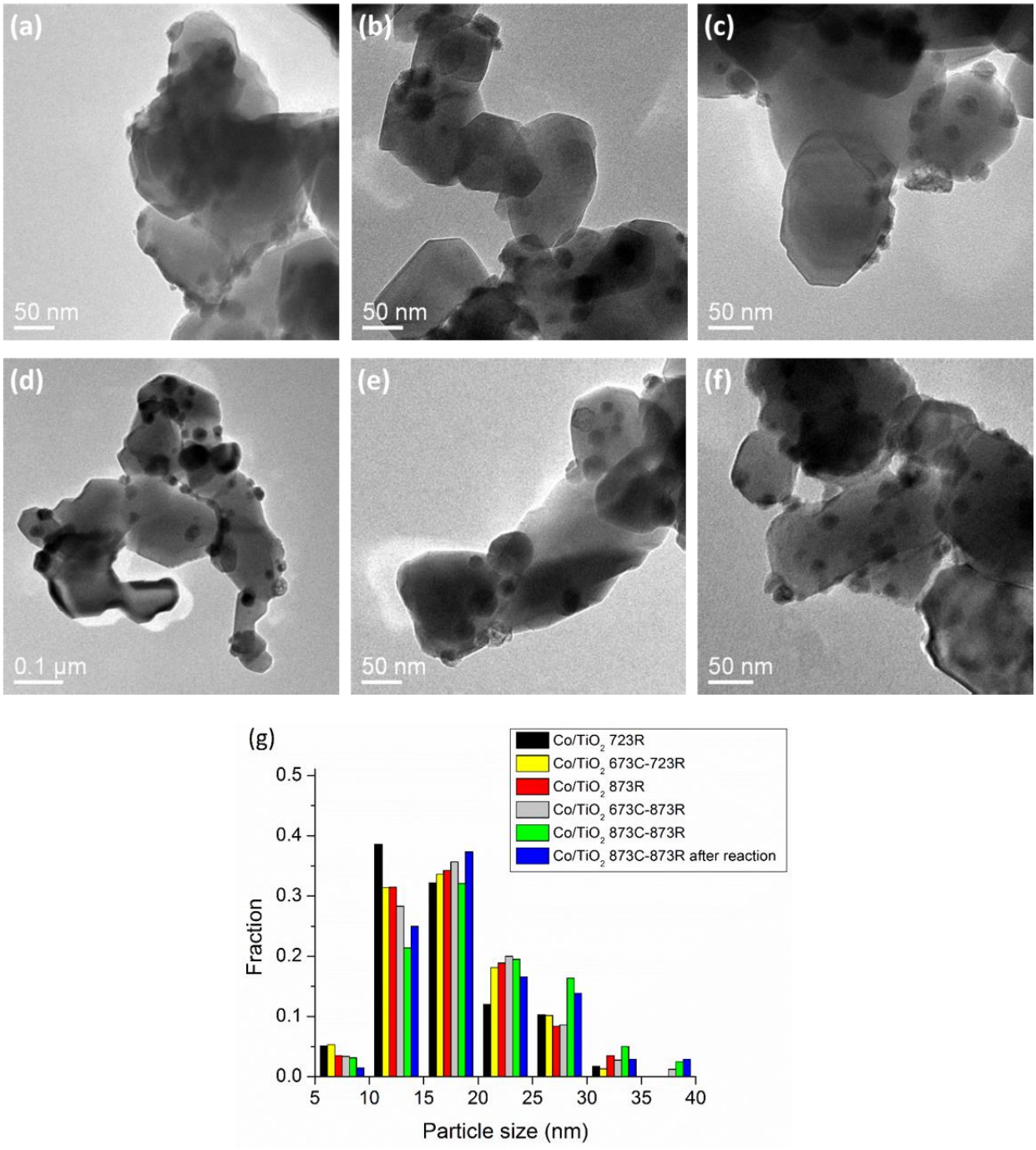

Figure 6.3 TEM images of (a) Co/TiO_2 723R, (b) Co/TiO_2 673C-723R, (c) Co/TiO_2 873R, (d) Co/TiO_2 673C-873R, (e) Co/TiO_2 873C-873R, (f) Co/TiO_2 873C-873R after three reactions with intermediate regeneration, and (g) particle size distribution of the catalysts.

The TiO_2 support and the Co/TiO_2 catalyst before the 2nd calcination and reduction were analyzed by Raman spectroscopy and XRD. Figure 6.4(i) shows the Raman spectrum of the TiO_2

support. The 440 and 615 cm^{-1} bands represent the rutile phase of TiO_2.[186] The intensities of these bands relative to the 140 cm^{-1} anatase band[186] show that the TiO_2 support is composed primarily of rutile. The XRD pattern of the TiO_2 support also confirms that the TiO_2 support is composed of rutile (Figure 6.5(i)).

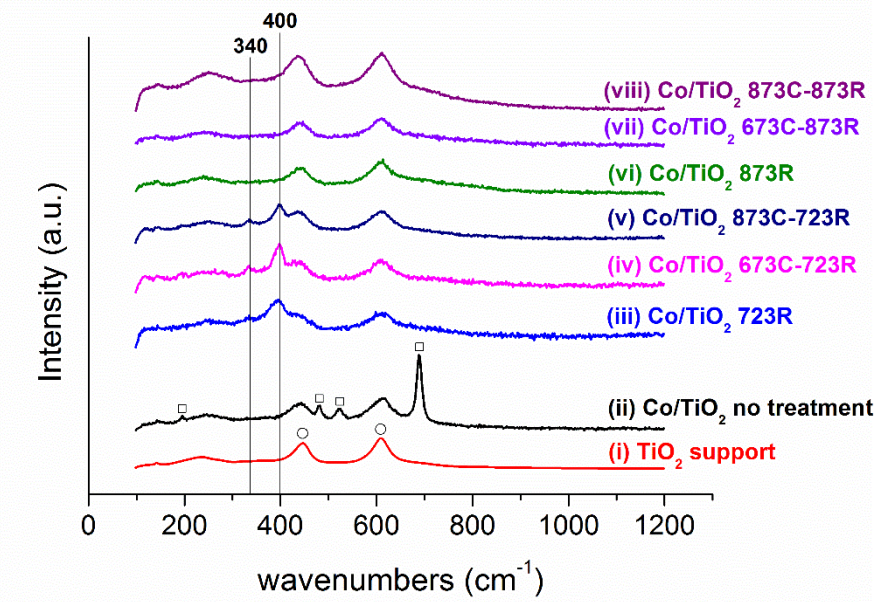

Figure 6.4 Raman spectra of Co/TiO_2 with different calcination and reduction temperatures. Spectra (iii) to (viii) were obtained by being treated *in situ* at different temperatures (○ TiO_2 rutile; □ Co_3O_4).

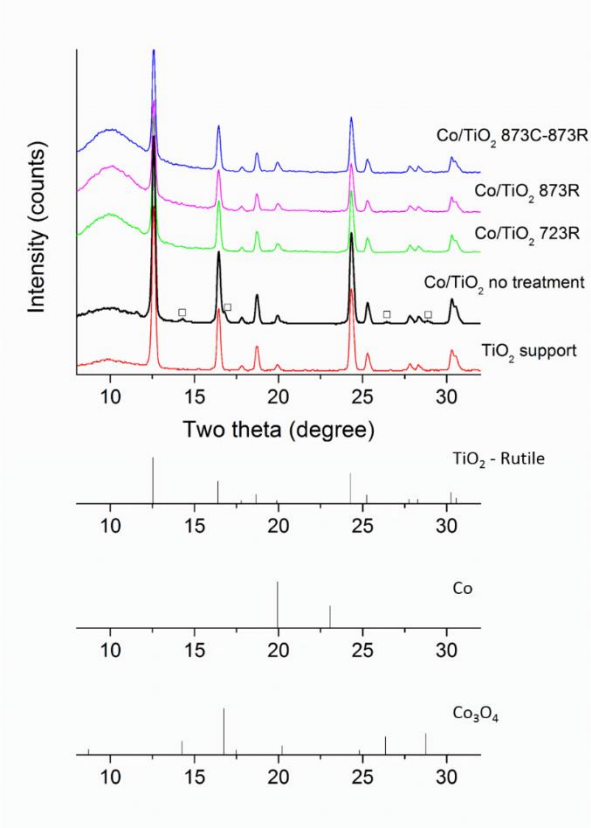

Figure 6.5 XRD patterns of TiO_2 support, Co/TiO_2 with no treatment (□ Co_3O_4), Co/TiO_2 723R, Co/TiO_2 873R, and Co/TiO_2 873C-873R.

The spectrum of the Co/TiO_2 before the 2nd calcination and reduction is shown in Figure 6.4(ii). The peaks at 190, 480, 520, and 685 cm^{-1} indicate that Co_3O_4 exists in the catalyst.[187] The XRD also shows the Co_3O_4 phase in this material (Figure 6.5(ii)). In Figure 6.4(iii)-(viii), no Co_3O_4 signals (*i.e.*, no peaks at 190, 480, 520, and 685 cm^{-1}) was observed after reduction at temperatures of 723 and 873 K. It should be noted that Raman spectroscopy cannot detect species in the metallic state. Thus, this indicates that Co_3O_4 is reduced to its metallic phase above 723 K. The XRD patterns presented in Figure 6.5(iii)-(v) show that Co_3O_4 peaks disappear after reduction at 723 or 873 K, indicating the reduction of the Co_3O_4 to metallic cobalt at above 723 K. However, the XRD could not distinguish between the overlapping metallic cobalt (19.94 °) and TiO_2 rutile peaks (19.89 °).

New Raman signals at 340 and 400 cm^{-1} appear in Figure 6.4(iii)-(v). These 340 and 400 cm^{-1} signals do not match with either cobalt titanate ($CoTiO_3$) or cobalt (II) oxide (CoO), as shown in Figure 6.6. Moreover, Figures 6.7 and A2 show that $CoTiO_3$ is essentially unreducible under the 873 K reduction treatment that is carried out in Figure 6.4(vi)-(viii). However, the samples producing the spectra (vi) to (viii) in Figure 3 are reduced at 873 K (*i.e.*, no 340 and 400 cm^{-1} signals in Figure 6.4(vi)-(viii)), so $CoTiO_3$ is not formed during the 2nd calcination and reduction treatments of the Co/TiO_2.

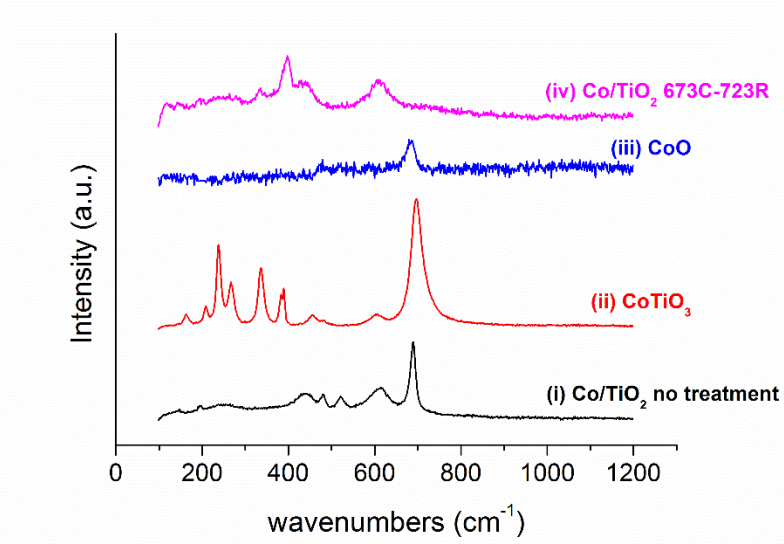

Figure 6.6 Comparison of Raman spectrum of the Co/TiO_2 catalysts, $CoTiO_3$ (Alfa Aesar, 99.8 %), and CoO (Acros Organics, > 99 %).

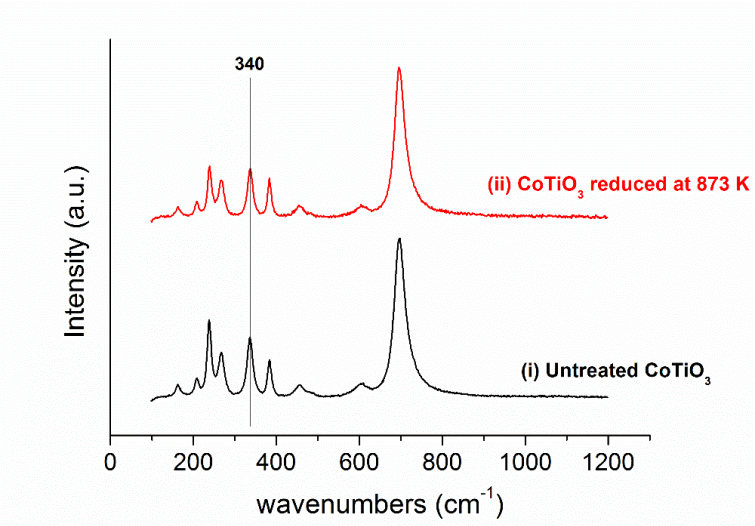

Figure 6.7 Comparison of Raman spectrum of $CoTiO_3$ before and after reduction at 873 K.

We attribute the 340 and 400 cm^{-1} signals to TiO_y migration onto cobalt, namely SMSI. High-temperature calcination leads to SMSI, which can form new bonds between Co, O, and Ti, creating new Raman signatures at 340 and 400 cm^{-1}. Figure 6.4(ii) does not show these signals while they are clearly visible in Figure 6.4(iii). The SMSI occurring on the Co/TiO_2 is unlikely due to restructuring of the TiO_2 support because the BET surface area of the catalysts was not affected by the high-temperature treatments (Table 6.1).[172] Figure 3 shows the persistence of TiO_2 signals after the calcination and reduction treatments up to 873 K. This observations suggest that the 340 and 400 cm^{-1} Raman signals are not due to changes in the TiO_2 support but due to the interaction between cobalt and TiO_2.

Figure 6.8 shows the relative peak area of the 340 and 400 cm^{-1} signals with different calcination temperatures. The area of the 340 cm^{-1} signal increases with increasing calcination temperature from 573 to 673 K and then decreases with increasing calcination temperature from 673 to 873 K. TiO_y layers are formed over Co_3O_4 (Co_3O_4-TiO_y) during the 673 K calcination, and this is then slightly reduced to a Co-TiO_y species under 723 K reduction, which gives rise to the 340 cm^{-1} signal. Additional TiO_y species migrate onto the Co_3O_4, creating multiple layers with

873 K calcination. This diminishes the 340 cm^{-1} signal. Therefore, this signal is attributed to the Co-O-Ti bond on top of a cobalt particle. This interaction requires some high-temperature treatment to be created, but is covered up by additional TiO_y layers with higher-temperature calcination.

The area of the 400 cm^{-1} signal decreases with increasing calcination temperature (Figure 6.8). This signal is probably due to interfacial sites on the Co_3O_4 covered by TiO_y species (Co-O-Ti bond). In the 340 cm^{-1} case, the environment directly below the surface of the bond is a cobalt particle. However, in the 400 cm^{-1} case, the environment directly below the bond is the TiO_2 support, as this signal is brought about at the particle edges. The decrease in the 400 cm^{-1} signal with increasing calcination temperature is because multiple layers of TiO_y may cover up these sites, making them invisible with surface-sensitive Raman spectroscopy. The sites creating the 400 cm^{-1} signal are affected more strongly by metal-support interaction than the sites on top of cobalt particles creating 340 cm^{-1} signal because covering the interfacial sites by TiO_y is easier than TiO_y migrating over the cobalt particles.

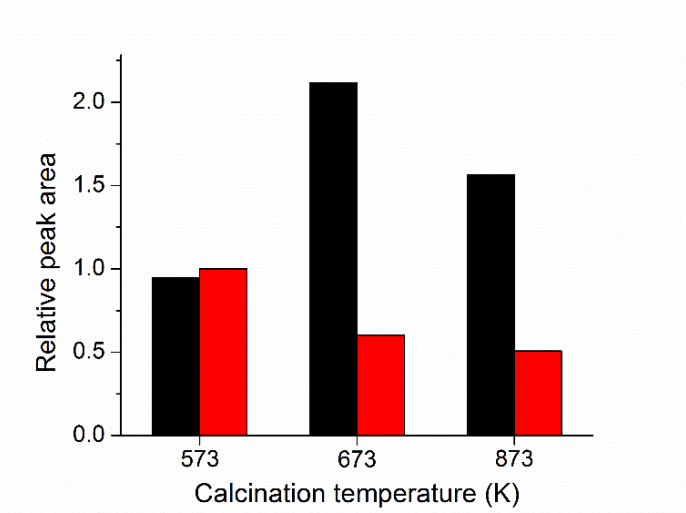

Figure 6.8 Relative peak area of 340 and 400 cm^{-1} signals with increasing calcination temperature while holding reduction temperature constant at 723 K (■ 340 cm^{-1}; ■ 400 cm^{-1}). All spectra were normalized to the 615 cm^{-1} rutile peak. The peak areas were then further normalized to 1.0 for Figure 6.4(iii).

The 340 and 400 cm^{-1} signals appears to be due to the TiO_y overlayer on the Co_3O_4. The intensity of these signals depended on calcination temperature, showing that higher-temperature calcination leads to stronger interaction between cobalt and TiO_2. These signals are not visible in the samples reduced at 873 K (Figure 6.4(vi)-(viii)), indicating that the Co_3O_4-TiO_y species formed with high-temperature calcination is reduced to its metallic state (Co-TiO_x, $x < y$) at 873 K (again, metallic species are not visible by Raman spectroscopy). The *in situ* Raman spectroscopy results are consistent with the STEM and TPR work that indicate the overcoating of cobalt particles with a TiO_2 layer.

Figure 6.9 is a model of what suggest occurs during the encapsulation of the cobalt particles. Oxidized TiO_y species migrate onto Co_3O_4 particles during high-temperature calcination, forming Co_3O_4-TiO_y species. Increasing the calcinatination temperature gives a strong interaction between the cobalt and TiO_2, increasing the TiO_y layer thickness. A high-temperature reduction treatment can reduce the Co_3O_4-TiO_y to Co-TiO_x. The size of the TiO_x layer is greatly influenced by the treatment conditions.

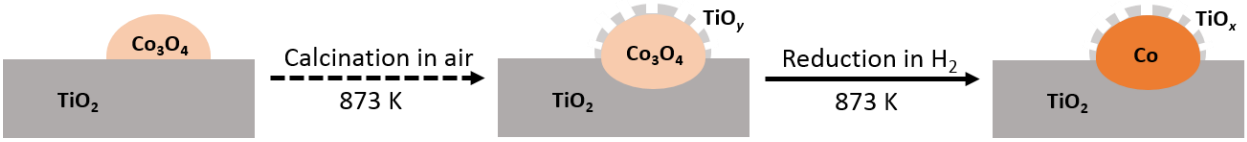

Figure 6.9 A model of the Co/TiO_2 system before and after calcination and reduction treatments.

6.3.2 Catalyst testing

The catalytic properties of the Co/TiO_2 with different treatments was studied for APH of furfuryl alcohol, furfural, and xylose. These are all key platform renewable non-petroleum based molecules.[154, 155] Hydrogenation of furfuryl alcohol and furfural has been studied using Pt, Pd, and Ru catalysts.[74, 107, 156, 188] Hydrogenation of carbohydrates (*e.g.*, xylose to xylitol) is an industrial process using Ru catalysts.[33] Precious-metal catalysts have been used for all the reactions. Thus, hydrogenation of furfuryl alcohol, furfural, and xylose would benefit from stabilizing inexpensive cobalt catalysts.

The deactivation of the Co/TiO_2 873C-873R catalyst during the APH of furfuryl alcohol in a continuous flow reactor is shown in Figure 6.10. Deactivation by coke formation on the catalyst is reversible upon calcination, while deactivation by leaching or sintering of cobalt is irreversible. The catalytic activity was able to be regenerated by calcination/re-reduction treatments, which suggests that no irreversible deactivation such as leaching and sintering occurred on the catalyst. No statistical difference in cobalt particle size of this catalyst was observed after 105 hour time-on-stream (20.2 ($\pm$6.2) nm before reaction and 19.3 ($\pm$5.4) nm after reaction; see Figure S1e-g). Furthermore, there was no change in the cobalt loading of the Co/TiO_2 873C-873R catalyst before and after the reaction and regeneration cycles, as measured by ICP-AES (Figure 6.11). However, up to 44.6 % of the cobalt leached from the Co/TiO_2 723R catalyst was observed. This suggests that treatments at high temperatures (*e.g.*, 873 K) prevent cobalt leaching and sintering. According to *in situ* Raman spectroscopy, cobalt particles are decorated by a more reduced TiO_x species formed with reduction at 873 K. These results suggest that reduced TiO_x over the cobalt particles are required to stabilize the cobalt particles under aqueous conditions. The TiO_x layers formed by

SMSI could preferentially decorate under-coordinated defect and edge sites of cobalt atoms which is where leaching and sintering begin.[150]

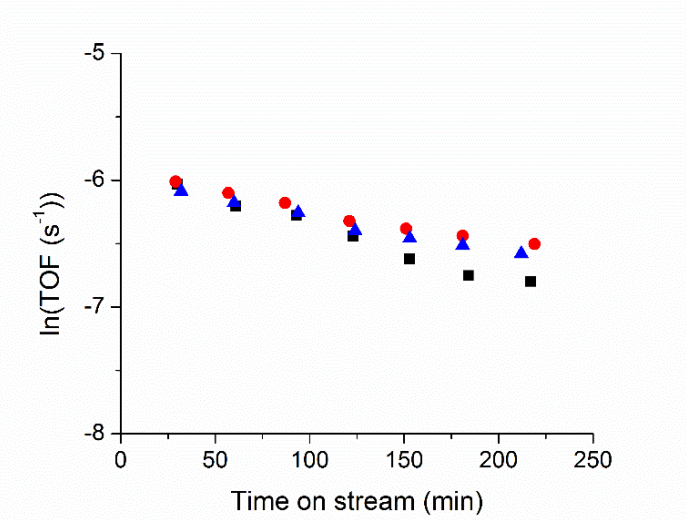

Figure 6.10 TOF for the APH of furfuryl alcohol as a function of time-on-stream and number of regenerations using Co/TiO_2 873C-873R (■ fresh; ● one regeneration; ▲ two regenerations). Furfuryl alcohol conversion varied between 9.3 and 19.5 %. Reaction conditions: 413 K, 2.34 MPa, WHSV = 94 h^{-1}, 2 wt% furfuryl alcohol solution as the feed, and hydrogen flow of 40 mL min^{-1}. Regeneration of the catalyst was carried out by calcining the catalyst at 873 K and then re-reducing the catalyst at 873 K.

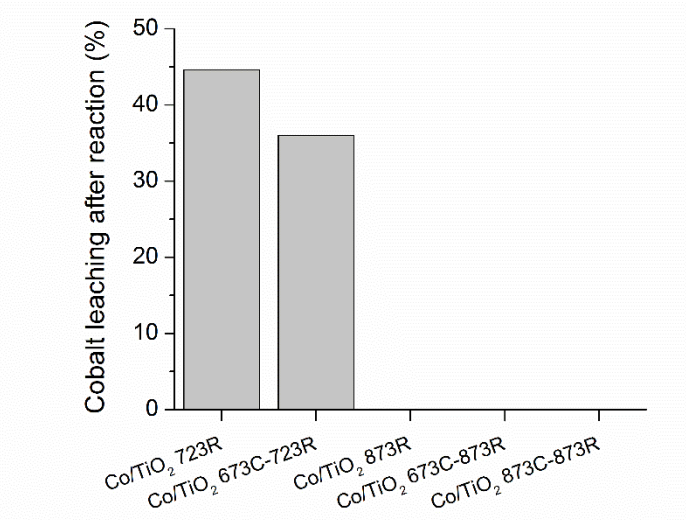

Figure 6.11 Cobalt leaching according to treatment conditions after reaction.

A main product produced from the APH of furfuryl alcohol over the Co/TiO_2 catalysts reduced at 873 K (*i.e.*, Co/TiO_2 873R, Co/TiO_2 673C-873R, and Co/TiO_2 873C-873R) was 1,5-pentanediol (Table 6.3). 1,5-Pentanediol is a valuable commodity chemical that could potentially be used to make polyurethanes and polyesters.[189] 1,5-Pentanediol can be produced via selective hydrogenolysis of tetrahydrofuran (THF) ring which occurs on bifunctional catalysts[158] (*e.g.*, hydrogenolysis of tetrahydrofurfuryl alcohol (THFA)) using noble-metal catalytic systems such as Rh-Re, Pd-Ir-Re, or Rh-Ir-Re.[158, 190-192] No product was observed when THFA was used as the feed over the Co/TiO_2 catalysts. Thus, 1,5-pentanediol is produced not by hydrogenolysis of THF ring but by hydrogenolysis of furan ring of furfuryl alcohol over the Co/TiO_2 catalysts. As shown in Table 6.3, the Co/TiO_2 873R catalyst had 17.5 % selectivity toward 1,5-pentanediol. The Co/TiO_2 673C-873R had 19.3 % 1,5-pentanediol selectivity. The 1,5-pentanediol selectivity increased from 19.3 to 30.3 % with increasing calcination temperature from 673 to 873 K (then reduced at 873 K). Nevertheless, the Co/TiO_2 723R catalyst made no 1,5-pentanediol and the Co/TiO_2 673C-723R produced 1,5-pentanediol but with low selectivity (4.5 %). These experimental results suggest that both calcination and reduction temperatures of Co/TiO_2 have a strong effect on 1,5-pentanediol production from furfuryl alcohol. As shown by *in situ* Raman spectroscopy, calcination at higher temperature causes stronger interaction between cobalt and TiO_x in the reduced catalyst. Based on the experimentally observed hydrogenolysis selectivity trends, we hypothesize that the SMSI effect forms bifunctional sites that are present at the Co-TiO_x interface. These bifunctional sites facilitate hydrogenolysis of C-O-C bond of furan ring, which give rise to high selectivity toward 1,5-pentanediol. The 1,5-pentanediol yield from furfuryl

alcohol hydrogenolysis over the Co/TiO_2 873C-873R remained after three cycles of calcination/reduction treatments, as shown in Figure 6.12.

Table 6.3 Molar carbon selectivity and cobalt leaching for the APH of furfuryl alcohol using the Co/TiO_2 with different treatment conditions. Reaction conditions: 413 K, 2.34 MPa, WHSV = 5.8 h^{-1}, 2 wt% furfuryl alcohol solution as the feed, and hydrogen flow of 40 mL min^{-1}.

Catalyst	Co/TiO_2 723R	Co/TiO_2 673C-723R	Co/TiO_2 873R	Co/TiO_2 673C-873R	Co/TiO_2 873C-873R
1st calcination (K)	573	573	573	573	573
2nd calcination (K)	-	673	-	673	873
Reduction (K)	723	723	873	873	873
Conversion (%)	59.4	99.6	99.7	99.4	99.0
Selectivity (%)					
1,5-pentanediol	0	4.5	17.5	19.3	30.3
1,2-pentanediol	0	0.9	2.5	2.3	2.4
1,4-pentanediol	0	6.6	6.0	7.9	2.1
tetrahydrofurfuryl alcohol	0.3	2.5	11.9	7.8	20.7
cyclopentanone	45.8	2.2	0.6	0.4	0.5
cyclopentanol	0.6	28.6	12.2	11.1	5.2
1.3-cyclopentandiol	2.1	6.7	5.5	5.4	1.6
2-methylfuran	0.1	0.5	2.5	3.9	4.6
methane	0	0.02	0.1	0.1	0.6
1-butanol	0	0.2	1.2	1.2	1.5
1-pentanol	0	1.2	2.5	2.5	2.1
2-pentanol	0	0.9	1.6	1.7	1.4
undetected liquid carbon[(a)]	4.5	14.1	21.7	21.4	23.6
Carbon balance[(b)] (%)	53.4	68.9	85.8	85.0	96.6
Time-on-stream (h)	35.4	35.3	37.5	37.9	43.9

[(a)]Undetected liquid carbon is the difference between moles of liquid carbon measured by TOC analyzer and moles of liquid carbon measured by GC-FID.
[(b)] Carbon balance is the sum of moles of liquid carbon measured by TOC analyzer and moles of gaseous carbon measured by GC-FID/TCD.

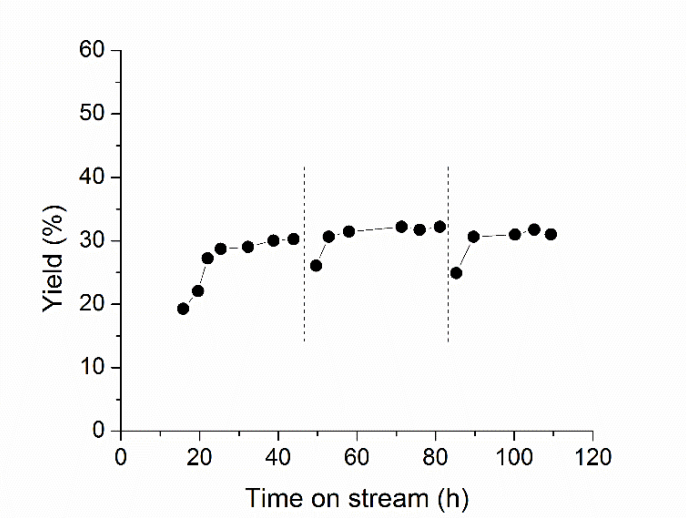

Figure 6.12 Carbon molar yield of 1,5-pentanediol from furfuryl alcohol according to the number of regenerations using the Co/TiO_2 873C-873R. Reaction conditions: 413 K, 2.34 MPa, WHSV = 94 h^{-1}, 2 wt% furfuryl alcohol solution as the feed, and hydrogen flow of 40 mL min^{-1}. Regeneration of the catalyst was carried out by calcining the catalyst at 873 K and then re-reducing the catalyst at 873 K.

The reaction pathways of the APH of furfuryl alcohol over the Co/TiO_2 873C-873R was found same as the reaction pathways shown in Scheme 5.1.

The Co/TiO_2 873C-873R catalyst was also selective for other APH reactions. It had 99.1 % xylitol yield for the APH of xylose at 373 K, as shown in Figure 6.13a. After the APH of xylose, the catalyst was regenerated and then tested for the APH of furfural. As shown in Figure 6.13b, furfural was converted into furfuryl alcohol with 95.4 % yield at 353 K. These results demonstrate that the Co/TiO_2 873C-873R catalyst was highly selective for hydrogenation of carbonyl compounds to the corresponding alcohols which is an important reaction for biomass conversion.[38, 53, 75]

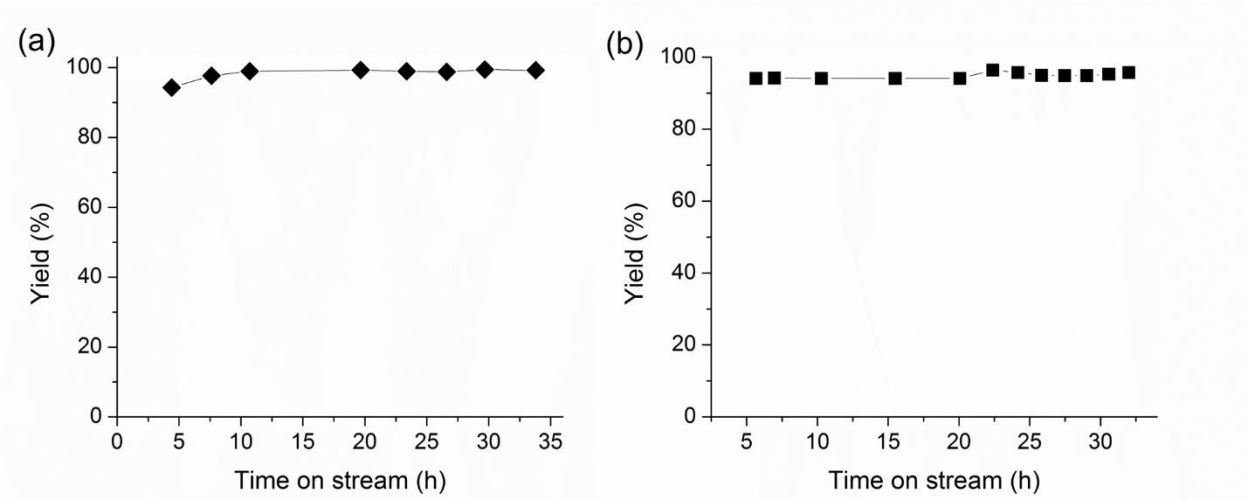

Figure 6.13 (a) Carbon molar yield as a function of time-on-stream for the conversion of xylose to xylitol at 373 K and WHSV = 5.8 h^{-1} using the Co/TiO_2 873C-873R (fresh). (b) Carbon molar yield as a function of time-on-stream for the conversion of furfural to furfuryl alcohol at 353 K and WHSV = 17.5 h^{-1} using the Co/TiO_2 873C-873R (one regeneration). Reaction conditions: 2.34 MPa, 2 wt% furfuryl alcohol solution as the feed, and hydrogen flow of 40 mL min^{-1}. Regeneration of the catalyst was carried out by calcining the catalyst at 873 K and then re-reducing the catalyst at 873 K.

6.4 Conclusions

High-temperature reduction treatments of a Co/TiO_2 catalyst stabilized the Co/TiO_2 catalyst by SMSI protecting the cobalt particles against leaching and sintering during aqueous-phase reactions. The SMSI effect stabilized the cobalt catalyst in a similar way that ALD stabilizes supported metal catalysts. High-temperature calcination was required to achieve a more intimate interaction between cobalt and TiO_x in the reduced catalyst. The SMSI effect enabled the Co/TiO_2 catalyst to selectively cleave C-O-C bond of furan ring, thereby producing 1,5-pentanediol from furfuryl alcohol. The selectivity toward 1,5-pentanediol was changed by calcination treatments. Moreover, the Co/TiO_2 873C-873R catalyst had over 95 % yield for hydrogenation of C=O bond to C-OH bond. These results open the door for the practical utilization of inexpensive base-metal catalysts for aqueous-phase conversion of renewable feedstocks and also demonstrate a more practical method to prepare stable supported base-metal catalysts.

CHAPTER 7

Summary and Recommendations for Future Research

7.1 Summary and Overall Conclusions

In this dissertation, APHDO and APH are chosen as model reactions for the conversion of biomass-derived feedstocks to design more active and stable supported metal catalysts.

In Chapter 3, the activity of monometallic catalysts were compared for hydrogenation and hydrogenolysis of different functionalities existing in biomass. Ru was the most active metal for hydrogenation of aldehydes containing no furan ring, whereas Pd was the most active metal for hydrogenation of aldehyde containing furan ring at 373 K. Ru was also most active for C-C bond cleavage reaction at 473 K among the tested catalysts. Pt and Ni were active for C-O-C bond cleavage at 523 K at which other metals were inactive.

As shown in Chapter 4, bimetallic Pd-Fe was even more active than monometallic Ru and Pd catalysts for hydrogenation of propanal and furfural to corresponding alcohols. A Pd_1Fe_3/Zr-P catalyst was up to 14 times more active than monometallic Pd/Zr-P and Pt/Zr-P catalysts for APHDO of sorbitol. The addition of Fe addition of Pd promoted not only the conversion of byproducts such as sorbitan and isosorbide but also the C-C bond cleavage by dehydrogenation followed by retro-aldol condensation.

In Chapters 5 and 6, the issue of base-metal catalyst stability in the aqueous phase was addressed by ALD and SMSI, respectively. ALD of TiO_2 film protected cobalt particles against irreversible leaching and sintering by decorating under-coordinated cobalt edge and defect sites. High-temperature treatments also stabilized Co/TiO_2 in the aqueous phase, causing SMSI. By the SMSI, partially reduced TiO_2 migrates onto cobalt decorating cobalt sites located at defects, edges, and corners. The SMSI also facilitated hydrogenolysis of C-O-C bond of furan ring over Co/TiO_2 catalyst.

7.2 Recommendations for Future Research

Catalysts for APHDO reactions require bifunctional sites (*i.e.*, metal and acid sites). For bifunctional metal-acid catalysts, the sites are mixed at the atomic level and distance between metal and acid sites is important for determining selectivity.[52] ALD allows carefully tuning catalytic sites by having intermediate mixing between different catalytic materials. Thus, ALD could be used to control selectivity of the catalysts for APHDO of sorbitol and other biomass-derived compounds. Also, bimetallic Pd-Fe catalysts was shown as an active catalyst for APH of carbonyl groups and APHDO of sorbitol. ALD could also be used to synthesize Pd-Fe catalysts having small and uniform nanoparticles which enable to increase catalytic activity.

The activity and selectivity data shown in this dissertation were obtained using diluted feedstocks. For the catalysts to become industrial, more concentrated feedstocks should be used to test the catalysts. Therefore, future research should study the effects of concentration of feedstocks for APH and APHDO reactions on the catalysts.

SMSI can occur between various metals and reducible metal oxide supports.[172, 193] There can be a number of applications of the SMSI effect with various combinations of metal-metal oxide support. The new SMSI catalysts can be used to improve selectivity toward products via C-O-C ring opening. Furthermore, the new SMSI catalysts would be tested for aqueous-phase conversion of more complicated and larger molecules such as sorbitol.

APPENDIX

Table A1 The values of a_m and v_m of metals from the reference.[81]

Metal	Structure	a_m (Å^2)	v_m (Å^3)
Pd	fcc	7.93	14.70
Pt	fcc	8.07	15.10
Ru	hcp	6.35	13.65
Rh	fcc	7.58	13.78
Ni	fcc	6.51	10.95
Co	hcp	5.43	11.00

Table A2 TOF (s^{-1}) of the APH of different feedstocks for the γ-Al_2O_3 supported monometallic catalysts.

Feedstock	acetaldehyde	propanal	acetone	xylose	furfural	furfuryl alcohol
0.5 wt% Pd	0.114	0.045	0.026	0.007	0.043	0.076
1 wt% Pd	0.1	0.052	0.033	0.006	0.092	0.068
3 wt% Pd	0.08	0.028	0.03	0.004	0.128	0.037
0.5 wt% Pt	0.149	0.094	0.24	0.019	0.022	0.006
1 wt% Pt	0.155	0.108	0.203	0.02	0.016	0.004
3 wt% Pt	0.143	0.089	0.486	0.014	0.014	0.003
0.5 wt% Ru	0.34	0.409	1.372	0.214	0	0
1 wt% Ru	0.436	0.369	4.737	0.295	0	0.018
3 wt% Ru	0.602	0.503	4.701	0.688	0.057	0.04
5 wt% Rh	0.017	0.01	0.558	0.01	0.01	0.005
5 wt% Ni	0.194	0.184	0.427	0.149	0.107	0.056
10 wt% Ni	0.557	0.49	0.592	0.169	0.12	0.062
20 wt% Ni	0.301	0.228	0.311	0.093	0.084	0.024
5 wt% Co	0.066	0	0.368	0.164	0.086	0
10 wt% Co	0	0	0.192	0.041	0.012	0
20 wt% Co	0.019	0.031	0.065	0.054	0.022	0

Table A3 Conversion (%) for the APH of different feedstocks for the γ-Al_2O_3 supported monometallic catalysts.

Feedstock	acetaldehyde	propanal	acetone	xylose	furfural	furfuryl alcohol
0.5 wt% Pd	8.5	4.4	2.6	4.2	10.9	20.0
1 wt% Pd	12.7	8.6	5.5	5.8	16.7	30.2
3 wt% Pd	28.0	12.9	14.0	10.3	30.1	25.6
0.5 wt% Pt	6.6	5.5	14.0	6.6	3.3	0.9
1 wt% Pt	13.1	12.0	22.5	13.0	4.7	1.3
3 wt% Pt	16.2	26.7	15.2	24.9	10.6	2.1
0.5 wt% Ru	5.9	9.4	3.3	28.6	0	0
1 wt% Ru	9.5	10.7	14.2	6.4	0	1.4
3 wt% Ru	5.0	30.6	30.9	19.6	2.3	8.0
5 wt% Rh	1.1	0.9	30.6	0.7	3.1	7.7
5 wt% Ni	11.7	14.7	3.5	8.9	4.6	11.8
10 wt% Ni	17.0	17.9	15.5	30.9	16.3	28.6
20 wt% Ni	22.4	22.3	21.8	23.4	30.8	30.9
5 wt% Co	2.5	0	1.8	6.1	11.1	0
10 wt% Co	0	0	1.3	2.1	2.1	0
20 wt% Co	2.1	4.5	1.0	5.9	8.2	0

Table A4 Reaction time (minutes) for the APH of different feedstocks for the γ-Al_2O_3 supported monometallic catalysts.

Feedstock	acetaldehyde	propanal	acetone	xylose	furfural	furfuryl alcohol
0.5 wt% Pd	120	120	120	180	180	180
1 wt% Pd	120	120	120	180	75	180
3 wt% Pd	120	120	120	180	75	75
0.5 wt% Pt	120	120	120	180	180	180
1 wt% Pt	120	120	120	180	180	180
3 wt% Pt	120	120	25	180	180	180
0.5 wt% Ru	120	120	25	180	180	180
1 wt% Ru	120	120	25	70	180	180
3 wt% Ru	35	120	25	35	75	180
5 wt% Rh	35	35	25	70	75	180
5 wt% Ni	120	120	25	70	75	180
10 wt% Ni	35	35	25	70	75	75
20 wt% Ni	35	35	25	35	75	75
5 wt% Co	120	120	25	70	180	180
10 wt% Co	120	120	25	70	180	180
20 wt% Co	120	120	25	70	180	180

Table A5 Carbon balance (%) for the APH of different feedstocks for the γ-Al_2O_3 supported monometallic catalysts.

Feedstock	acetaldehyde	propanal	acetone	xylose	furfural	furfuryl alcohol
0.5 wt% Pd	90.4	90.4	98.3	90.3	95.3	90.4
1 wt% Pd	90.6	90.2	90.1	91.1	99.5	90.7
3 wt% Pd	96.6	90.4	98.7	90.4	97.4	90.7
0.5 wt% Pt	91.3	98.1	90.3	94.2	90.0	98.7
1 wt% Pt	97.4	96.8	90.1	92.0	94.4	97.2
3 wt% Pt	90.4	90.6	93.4	93.3	90.7	90.3
0.5 wt% Ru	90.8	92.3	97.1	98.3	101.7	90.3
1 wt% Ru	90.5	90.2	90.8	97.5	96.7	90.8
3 wt% Ru	93.0	97.8	90.6	91.2	98.2	90.6
5 wt% Rh	98.6	90.3	90.9	96.5	99.3	90.6
5 wt% Ni	90.4	97.2	90.8	96.5	96.5	90.9
10 wt% Ni	95.3	95.5	91.4	97.9	92.8	90.9
20 wt% Ni	94.6	90.5	100.4	93.0	95.0	90.1
5 wt% Co	90.6	94.4	90.1	97.6	97.9	90.3
10 wt% Co	90.4	93.6	103.0	97.0	96.2	90.4
20 wt% Co	90.6	90.3	90.8	96.9	94.7	90.9

Table A6 TOF, conversion, and carbon balance for the aqueous-phase hydrogenolysis of xylitol over the γ-Al_2O_3 supported monometallic catalysts. Reaction conditions: 473 K, 5.41 MPa, and 5 wt% xylitol solution as the feed.

Catalyst	TOF $\times 10^3$ (s^{-1})	Conversion (%)	Carbon balance (%)
3 wt% Pd	0.3	9.5	90.9
0.5 wt% Pt	5.3	9.2	91.5
1 wt% Pt	3.3	8.3	92.6
3 wt% Pt	3.6	11.8	90.8
0.5 wt% Ru	28.3	8.3	93.2
1 wt% Ru	91.7	14.1	92.2
3 wt% Ru	48.3	16.4	92.4
10 wt% Ni	3.6	4.3	97.9
20 wt% Ni	1.9	8.9	94.1
5 wt% Co	24.2	8.3	94.6
10 wt% Co	13.3	10.0	92.3
20 wt% Co	4.4	7.1	94.3

Table A7 Conversion (%) for the APH of different feedstocks for the γ-Al_2O_3 supported monometallic and bimetallic catalysts.

Feedstock	propanal	xylose	furfural
Pd_1Ni_1	6.8	15.4	15.2
Pd_1Ni_3	10.3	30.9	10.3
Pd_1Co_1	6.8	2.3	27.6
Pd_1Co_3	4.1	14.2	13.5
Pd_1Fe_1	6.8	2.3	54.0
Pd_1Fe_3	15.7	7.1	45.5
3 wt% Pd	12.9	10.3	30.1
Ru_1Ni_1	28.6	31.8	10.9
Ru_1Ni_3	30.6	32.3	15.2
Ru_1Co_1	25.6	29.6	23.5
Ru_1Co_3	23.3	28.5	21.3
Ru_1Fe_1	16.8	27.0	25.4
Ru_1Fe_3	16.2	27.0	21.2
3 wt% Ru	30.6	19.6	2.3
Pt_1Ni_1	38.3	24.5	5.9
Pt_1Ni_3	45.6	29.7	18.2
Pt_1Co_1	33.9	10.4	11.5
Pt_1Co_3	39.7	16.4	15.8
Pt_1Fe_1	40.5	9.5	17.6
Pt_1Fe_3	41.8	7.6	44.8
3 wt% Pt	26.7	24.9	10.6
20 wt% Ni	22.3	23.4	30.8
20 wt% Co	4.5	5.9	8.2
20 wt% Fe	0	0	0

Table A8 Reaction time (minutes) for the APH of different feedstocks for the γ-Al_2O_3 supported monometallic and bimetallic catalysts.

Feedstock	propanal	xylose	furfural
Pd_1Ni_1	35	35	75
Pd_1Ni_3	35	35	75
Pd_1Co_1	35	35	75
Pd_1Co_3	35	35	75
Pd_1Fe_1	35	35	75
Pd_1Fe_3	35	35	75
3 wt% Pd	120	180	75
Ru_1Ni_1	35	35	75
Ru_1Ni_3	35	35	75
Ru_1Co_1	35	35	75
Ru_1Co_3	35	35	75
Ru_1Fe_1	35	35	75
Ru_1Fe_3	35	35	75
3 wt% Ru	120	35	75
Pt_1Ni_1	35	35	75
Pt_1Ni_3	35	35	75
Pt_1Co_1	35	35	75
Pt_1Co_3	35	35	75
Pt_1Fe_1	35	35	75
Pt_1Fe_3	35	35	75
3 wt% Pt	120	180	180
20 wt% Ni	35	35	75
20 wt% Co	120	70	180
20 wt% Fe	120	180	180

Table A9 Carbon balance (%) for the APH of different feedstocks for the γ-Al_2O_3 supported monometallic and bimetallic catalysts.

Feedstock	propanal	xylose	furfural
Pd_1Ni_1	91.3	96.8	94.0
Pd_1Ni_3	90.8	96.2	98.0
Pd_1Co_1	91.7	94.6	98.4
Pd_1Co_3	92.1	96.5	92.6
Pd_1Fe_1	93.2	95.6	98.1
Pd_1Fe_3	90.9	93.2	97.6
3 wt% Pd	90.4	90.4	97.4
Ru_1Ni_1	91.4	96.9	92.4
Ru_1Ni_3	93.5	96.5	93.5
Ru_1Co_1	94.1	97.1	94.1
Ru_1Co_3	95.0	95.6	91.4
Ru_1Fe_1	92.7	98.9	92.3
Ru_1Fe_3	91.6	95.6	95.6
3 wt% Ru	97.8	91.2	98.2
Pt_1Ni_1	93.1	95.9	91.4
Pt_1Ni_3	92.5	97.9	91.2
Pt_1Co_1	92.1	96.0	93.1
Pt_1Co_3	92.6	95.5	92.8
Pt_1Fe_1	92.7	95.4	94.6
Pt_1Fe_3	90.9	95.3	93.2
3 wt% Pt	90.6	93.3	90.7
20 wt% Ni	90.5	93.0	95.0
20 wt% Co	90.3	96.9	94.7
20 wt% Fe	98.2	99.8	98.9

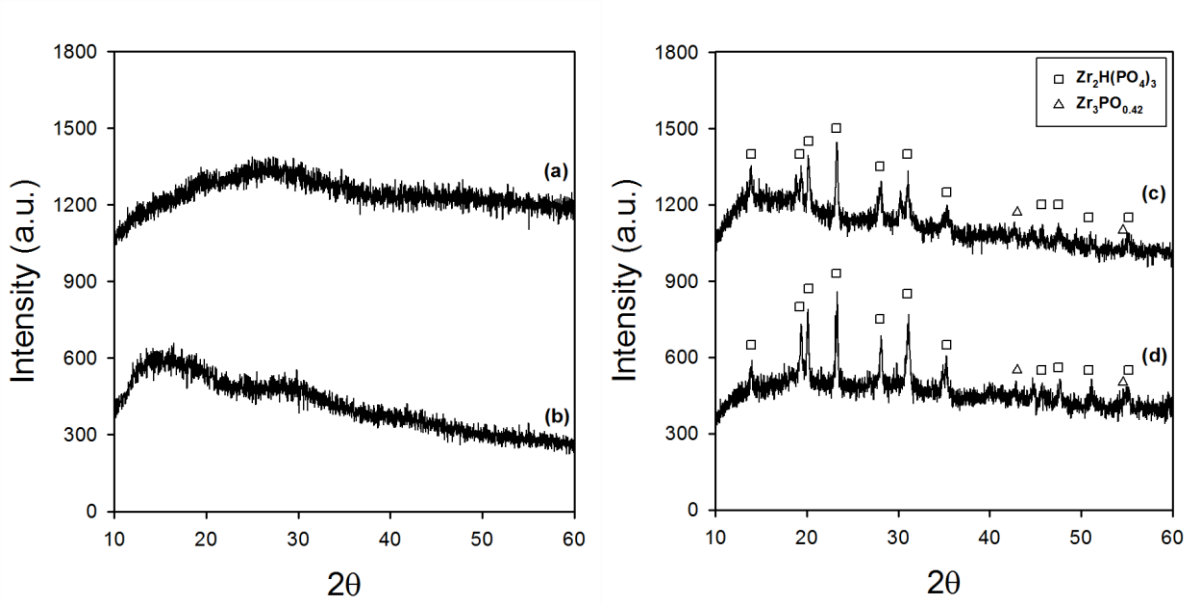

Figure A1 XRD patterns of (a) Pd/Zr-P before reaction, (b) Pd-Fe/Zr-P before reaction, (c) Pd/Zr-P after reaction, and (d) Pd-Fe/Zr-P after reaction.

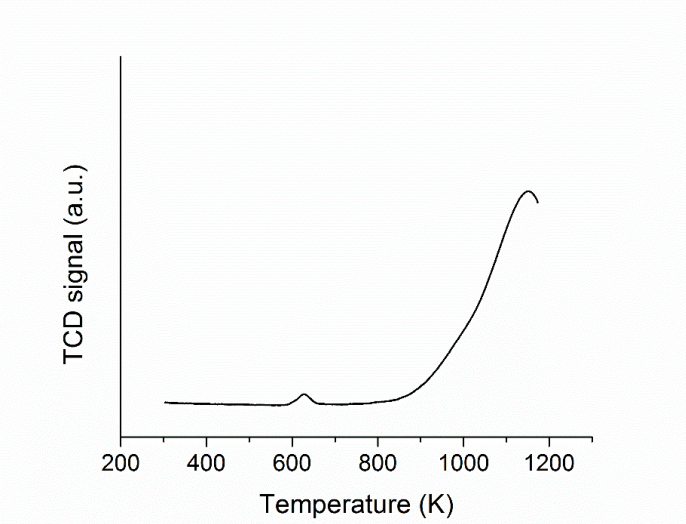

Figure A2 TPR pattern of bulk $CoTiO_3$ (Alfa Aesar, 99.8 %).

REFERENCES

1. BP, *BP Statistical Review of World Energy June 2014*, British Petroleum, 2014.
2. L. R. Lynd, J. H. Cushman, R. J. Nichols and C. E. Wyman, Fuel Ethanol from Cellulosic Biomass, *Science*, 1991, **251**, 1318-1323.
3. R. R. Davda, J. W. Shabaker, G. W. Huber, R. D. Cortright and J. A. Dumesic, A Review of Catalytic Issues and Process Conditions for Renewable Hydrogen and Alkanes by Aqueous-Phase Reforming of Oxygenated Hydrocarbons over Supported Metal Catalysts, *Applied Catalysis B: Environmental*, 2005, **56**, 171-186.
4. G. W. Huber and J. A. Dumesic, An Overview of Aqueous-Phase Catalytic Processes for Production of Hydrogen and Alkanes in a Biorefinery, *Catalysis Today*, 2006, **111**, 119-132.
5. J. N. Chheda and J. A. Dumesic, An Overview of Dehydration, Aldol-Condensation and Hydrogenation Processes for Production of Liquid Alkanes from Biomass-Derived Carbohydrates, *Catalysis Today*, 2007, **123**, 59-70.
6. J. N. Chheda, G. W. Huber and J. A. Dumesic, Liquid-Phase Catalytic Processing of Biomass-Derived Oxygenated Hydrocarbons to Fuels and Chemicals, *Angewandte Chemie International Edition*, 2007, **46**, 7164-7183.
7. D. A. Simonetti and J. A. Dumesic, Catalytic Strategies for Changing the Energy Content and Achieving C-C Coupling in Biomass-Derived Oxygenated Hydrocarbons, *ChemSusChem*, 2008, **1**, 725-733.
8. D. A. Simonetti and J. A. Dumesic, Catalytic Production of Liquid Fuels from Biomass-Derived Oxygenated Hydrocarbons: Catalytic Coupling at Multiple Length Scales, *Catalysis Reviews: Science and Engineering*, 2009, **51**, 441-484.
9. D. M. Alonso, J. Q. Bond and J. A. Dumesic, Catalytic conversion of biomass to biofuels, *Green Chemistry*, 2010, **12**, 1493-1513.
10. J. C. Serrano-Ruiz, R. M. West and J. A. Dumesic, Catalytic Conversion of Renewable Biomass Resources to Fuels and Chemicals, *Annual Review of Chemical and Biomolecular Engineering*, 2010, **1**, 79-100.
11. J. C. Serrano-Ruiz and J. A. Dumesic, Catalytic Routes for the Conversion of Biomass into Liquid Hydrocarbon Transportation Fuels, *Energy & Environmental Science*, 2011, **4**, 83-99.
12. Y. Pu, D. Zhang, P. M. Singh and A. J. Ragauskas, The New Forestry Biofuels Sector, *Biofuels, Bioproducts and Biorefining*, 2008, **2**, 58-73.
13. C.-H. Zhou, X. Xia, C.-X. Lin, D.-S. Tong and J. Beltramini, Catalytic Conversion of Lignocellulosic Biomass to Fine Chemicals and Fuels, *Chemical Society Reviews*, 2011, **40**, 5588-5617.
14. G. W. Huber, S. Iborra and A. Corma, Synthesis of Transportation Fuels from Biomass: Chemistry, Catalysts, and Engineering, *Chemical Reviews*, 2006, **106**, 4044-4098.
15. L. Petrus and M. A. Noordermeer, Biomass to Biofuels, a Chemical Perspective, *Green Chemistry*, 2006, **8**, 861-867.
16. A. Corma, S. Iborra and A. Velty, Chemical Routes for the Transformation of Biomass into Chemicals, *Chemical Reviews*, 2007, **107**, 2411-2502.
17. D. L. Klass, *Biomass for Renewable Energy, Fuels, and Chemicals*, Academic Press, 1998.
18. G. W. Huber, *Intrinsic Kinetics of Pt Promoted Co/SiO_2 Fischer-Tropsch Synthesis Catalysts*, Brigham Young University, Provo, UT, 2000.

19. C. H. Bartholomew and R. J. Farrauto, *Fundamentals of Industrial Catalytic Processes*, 2nd ed., John Wiley & Sons, Inc., Hoboken, NJ, 2005.
20. J. Lee and M. J. Castaldi, A Study on Performance and Emissions of a 4-stroke IC Engine Operated on Landfill Gas with Syngas Addition, *ASME Conference Proceedings*, 2010, **43932**, 61-67.
21. J. Lee, *A Study on Performance and Emissions of a 4-stroke IC Engine Operating on Landfill Gas with the Addition of H_2, CO and Syngas*, Columbia University, New York, NY, 2010.
22. M. P. Kohn, J. Lee, M. L. Basinger and M. J. Castaldi, Performance of an Internal Combustion Engine Operating on Landfill Gas and the Effect of Syngas Addition, *Industrial & Engineering Chemistry Research*, 2011, **50**, 3570-3579.
23. R. D. Cortright, R. R. Davda and J. A. Dumesic, Hydrogen from Catalytic Reforming of Biomass-Derived Hydrocarbons in Liquid Water, *Nature*, 2002, **418**, 964-967.
24. G. W. Huber, J. W. Shabaker and J. A. Dumesic, Raney Ni-Sn Catalyst for H_2 Production from Biomass-Derived Hydrocarbons, *Science*, 2003, **300**, 2075-2077.
25. J. W. Shabaker, G. W. Huber, R. R. Davda, R. D. Cortright and J. A. Dumesic, Aqueous-Phase Reforming of Ethylene Glycol over Supported Platinum Catalysts, *Catalysis Letters*, 2003, **88**, 1-8.
26. R. R. Davda, J. W. Shabaker, G. W. Huber, R. D. Cortright and J. A. Dumesic, Aqueous-Phase Reforming of Ethylene Glycol on Silica-Supported Metal Catalysts, *Applied Catalysis B: Environmental*, 2003, **43**, 13-26.
27. J. W. Shabaker, G. W. Huber and J. A. Dumesic, Aqueous-Phase Reforming of Oxygenated Hydrocarbons over Sn-Modified Ni Catalysts, *Journal of Catalysis*, 2004, **222**, 180-191.
28. G. W. Huber, J. W. Shabaker, S. T. Evans and J. A. Dumesic, Aqueous-Phase Reforming of Ethylene Glycol over Supported Pt and Pd Bimetallic Catalysts, *Applied Catalysis B: Environmental*, 2006, **62**, 226-235.
29. G. W. Huber, R. D. Cortright and J. A. Dumesic, Renewable Alkanes by Aqueous-Phase Reforming of Biomass-Derived Oxygenates, *Angewandte Chemie International Edition*, 2004, **43**, 1549-1551.
30. G. W. Huber, J. N. Chheda, C. J. Barrett and J. A. Dumesic, Production of Liquid Alkanes by Aqueous-Phase Processing of Biomass-Derived Carbohydrates, *Science*, 2005, **308**, 1446-1450.
31. S. Liu, M. Tamura, Y. Nakagawa and K. Tomishige, One-Pot Conversion of Cellulose into n-Hexane over the Ir-ReO_x/SiO_2 Catalyst Combined with HZSM-5, *ACS Sustainable Chemistry & Engineering*, 2014, **2**, 1819-1827.
32. B. Op de Beeck, M. Dusselier, J. Geboers, J. Holsbeek, E. Morré, S. Oswald, L. Giebeler and B. F. Sels, Direct Catalytic Conversion of Cellulose to Liquid Straight-Chain Alkanes, *Energy & Environmental Science*, 2015, **8**, 230-240.
33. P. Gallezot, N. Nicolaus, G. Flèche, P. Fuertes and A. Perrard, Glucose Hydrogenation on Ruthenium Catalysts in a Trickle-Bed Reactor, *Journal of Catalysis*, 1998, **180**, 51-55.
34. A. Perrard, P. Gallezot, J. P. Joly, R. Durand, U. Baljou, B. Coq and P. Trens, Highly Efficient Metal Catalysts Supported on Activated Carbon Cloths: A Catalytic Application for the Hydrogenation of D-Glucose to D-Sorbitol, *Applied Catalysis A: General*, 2007, **331**, 100-104.

35. H. Olcay, Y. Xu and G. W. Huber, Effects of Hydrogen and Water on the Activity and Selectivity of Acetic Acid Hydrogenation on Ruthenium, *Green Chemistry*, 2014, **16**, 911-924.
36. E. L. Kunkes, D. A. Simonetti, R. M. West, J. C. Serrano-Ruiz, C. A. Gärtner and J. A. Dumesic, Catalytic Conversion of Biomass to Monofunctional Hydrocarbons and Targeted Liquid-Fuel Classes, *Science*, 2008, **322**, 417-421.
37. E. I. Gurbuz, E. L. Kunkes and J. A. Dumesic, Dual-bed catalyst system for C-C coupling of biomass-derived oxygenated hydrocarbons to fuel-grade compounds, *Green Chemistry*, 2010, **12**, 223-227.
38. N. Li and G. W. Huber, Aqueous-Phase Hydrodeoxygenation of Sorbitol with Pt/SiO_2-Al_2O_3: Identification of Reaction Intermediates, *Journal of Catalysis*, 2010, **270**, 48-59.
39. N. Li, G. A. Tompsett and G. W. Huber, Renewable High-Octane Gasoline by Aqueous-Phase Hydrodeoxygenation of C_5 and C_6 Carbohydrates over Pt/Zirconium Phosphate Catalysts, *ChemSusChem*, 2010, **3**, 1154-1157.
40. T. P. Vispute, H. Y. Zhang, A. Sanna, R. Xiao and G. W. Huber, Renewable Chemical Commodity Feedstocks from Integrated Catalytic Processing of Pyrolysis Oils, *Science*, 2010, **330**, 1222-1227.
41. N. Li, G. A. Tompsett, T. Y. Zhang, J. A. Shi, C. E. Wyman and G. W. Huber, Renewable Gasoline from Aqueous Phase Hydrodeoxygenation of Aqueous Sugar Solutions Prepared by Hydrolysis of Maple Wood, *Green Chemistry*, 2011, **13**, 91-101.
42. D. C. Elliott, T. R. Hart, G. G. Neuenschwander, L. J. Rotness and A. H. Zacher, Catalytic Hydroprocessing of Biomass Fast Pyrolysis Bio-Oil to Produce Hydrocarbon Products, *Environmental Progress & Sustainable Energy*, 2009, **28**, 441-449.
43. G. W. Huber, *Renewable Hydrogen and Liquid Alkanes from Aqueous-Phase Processing of Biomass-Derived Carbohydrates*, University of Wisconsin-Madison, Madison, WI, 2005.
44. J. Lee, Y. Xu and G. W. Huber, Aqueous-Phase Hydrogenation of Biomass-Derived Oxygenates over Monometallic Catalysts, 245th American Chemical Society National Meeting, New Orleans, LA, 2013.
45. J. Lee, Y. Xu and G. W. Huber, Aqueous-Phase Hydrogenation and Hydrogenolysis of Biomass-Derived Oxygenates over Monometallic Catalysts, 246th American Chemical Society National Meeting, Indianapolis, IN, 2013.
46. T. P. Vispute and G. W. Huber, Production of hydrogen, alkanes and polyols by aqueous phase processing of wood-derived pyrolysis oils, *Green Chemistry*, 2009, **11**, 1433-1445.
47. D. C. Elliott, Historical developments in hydroprocessing bio-oils, *Energy & Fuels*, 2007, **21**, 1792-1815.
48. B. W. Hoffer, E. Crezee, P. R. M. Mooijman, A. D. van Langeveld, F. Kapteijn and J. A. Moulijn, Carbon Supported Ru Catalysts as Promising Alternative for Raney-Type Ni in the Selective Hydrogenation of D-Glucose, *Catalysis Today*, 2003, **79–80**, 35-41.
49. E. P. Maris, W. C. Ketchie, V. Oleshko and R. J. Davis, Metal Particle Growth during Glucose Hydrogenation over Ru/SiO_2 Evaluated by X-ray Absorption Spectroscopy and Electron Microscopy, *The Journal of Physical Chemistry B*, 2006, **110**, 7869-7876.
50. L. Vilcocq, A. Cabiac, C. Especel, S. Lacombe and D. Duprez, New Insights into the Mechanism of Sorbitol Transformation over an Original Bifunctional Catalytic System, *Journal of Catalysis*, 2014, **320**, 16-25.

51. A. V. Kirilin, A. V. Tokarev, E. V. Murzina, L. M. Kustov, J.-P. Mikkola and D. Y. Murzin, Reaction Products and Transformations of Intermediates in the Aqueous-Phase Reforming of Sorbitol, *ChemSusChem*, 2010, **3**, 708-718.
52. Y. T. Kim, J. A. Dumesic and G. W. Huber, Aqueous-Phase Hydrodeoxygenation of Sorbitol: A Comparative Study of Pt/Zr phosphate and Pt-ReO_x/C, *Journal of Catalysis*, 2013, **304**, 72-85.
53. B. M. Moreno, N. Li, J. Lee, G. W. Huber and M. T. Klein, Modeling Aqueous-Phase Hydrodeoxygenation of Sorbitol over Pt/SiO_2-Al_2O_3, *RSC Advances*, 2013, **3**, 23769-23784.
54. *Mineral Commodity Summaries 2014*, U.S. Geological Survey, 2014.
55. Y. Kamiya, S. Sakata, Y. Yoshinaga, R. Ohnishi and T. Okuhara, Zirconium Phosphate with a High Surface Area as a Water-Tolerant Solid Acid, *Catalysis Letters*, 2004, **94**, 45-47.
56. M. K. Wiedmann, D. H. K. Jackson, Y. J. Pagan-Torres, E. Cho, J. A. Dumesic and T. F. Kuech, Atomic Layer Deposition of Titanium Phosphate on Silica Nanoparticles, *Journal of Vacuum Science & Technology A*, 2012, **30**, 01A13.
57. M. A. Vannice, *Kinetics of Catalytic Reactions*, Springer, New York, NY, 2005.
58. H. S. Fogler, *Elements of Chemical Reaction Engineering*, 4th ed., Prentice Hall, NJ, 2006.
59. H. Olcay, L. J. Xu, Y. Xu and G. W. Huber, Aqueous-Phase Hydrogenation of Acetic Acid over Transition Metal Catalysts, *ChemCatChem*, 2010, **2**, 1420-1424.
60. S. Narayanan and R. Unnikrishnan, Acetone Hydrogenation over co-Precipitated Ni/Al_2O_3, Co/Al_2O_3 and Fe/Al_2O_3 Catalysts, *Journal of the Chemical Society, Faraday Transactions*, 1998, **94**, 1123-1128.
61. B. Coq, F. Figueras, P. Geneste, C. Moreau, P. Moreau and M. Warawdekar, Hydrogenation of α,β-Unsaturated Carbonyls: Acrolein Hydrogenation on Group VIII Metal Catalysts, *Journal of Molecular Catalysis*, 1993, **78**, 211-226.
62. P. L. Dhepe and A. Fukuoka, Cellulose Conversion under Heterogeneous Catalysis, *ChemSusChem*, 2008, **1**, 969-975.
63. J. J. Bozell and G. R. Petersen, Technology Development for the Production of Biobased Products from Biorefinery Carbohydrates-the US Department of Energy's "Top 10" Revisited, *Green Chemistry*, 2010, **12**, 539-554.
64. S. Senkan, K. Krantz, S. Ozturk, V. Zengin and I. Onal, High-Throughput Testing of Heterogeneous Catalyst Libraries using Array Microreactors and Mass Spectrometry, *Angewandte Chemie International Edition*, 1999, **38**, 2794-2799.
65. U. Rodemerck, D. Wolf, O. V. Buyevskaya, P. Claus, S. Senkan and M. Baerns, High-Throughput Synthesis and Screening of Catalytic Materials: Case Study on the Search for a Low-Temperature Catalyst for the Oxidation of Low-Concentration Propane, *Chemical Engineering Journal*, 2001, **82**, 3-11.
66. I. Hahndorf, O. Buyevskaya, M. Langpape, G. Grubert, S. Kolf, E. Guillon and M. Baerns, Experimental Equipment for High-Throughput Synthesis and Testing of Catalytic Materials, *Chemical Engineering Journal*, 2002, **89**, 119-125.
67. Y. Liu, P. Cong, R. D. Doolen, S. Guan, V. Markov, L. Woo, S. Zey ßand U. Dingerdissen, Discovery from Combinatorial Heterogeneous Catalysis: A New Class of Catalyst for Ethane Oxidative Dehydrogenation at Low Temperatures, *Applied Catalysis A: General*, 2003, **254**, 59-66.

68. A. Corma, J. M. Serra and A. Chica, Discovery of New Paraffin Isomerization Catalysts Based on SO_4^{2-}/ZrO_2 and WO_x/ZrO_2 Applying Combinatorial Techniques, *Catalysis Today*, 2003, **81**, 495-506.
69. J. Greeley, T. F. Jaramillo, J. Bonde, I. Chorkendorff and J. K. Norskov, Computational High-Throughput Screening of Electrocatalytic Materials for Hydrogen Evolution, *Nature Materials*, 2006, **5**, 909-913.
70. P. Serna, L. A. Baumes, M. Moliner and A. Corma, Combining High-Throughput Experimentation, Advanced Data Modeling and Fundamental Knowledge to Develop Catalysts for the Epoxidation of Large Olefins and Fatty Esters, *Journal of Catalysis*, 2008, **258**, 25-34.
71. I. Onal, D. Duzenli, A. Seubsai, M. Kahn, E. Seker and S. Senkan, Propylene Epoxidation: High-Throughput Screening of Supported Metal Catalysts Combinatorially Prepared by Rapid Sol-Gel Method, *Topics in Catalysis*, 2010, **53**, 92-99.
72. L. A. Baumes, P. Serna and A. Corma, Merging Traditional and High-Throughput Approaches Results in Efficient Design, Synthesis and Screening of Catalysts for an Industrial Process, *Applied Catalysis A: General*, 2010, **381**, 197-208.
73. J. E. Bedenbaugh, S. Kim, E. Sasmaz and J. Lauterbach, High-Throughput Investigation of Catalysts for JP-8 Fuel Cracking to Liquefied Petroleum Gas, *ACS Combinatorial Science*, 2013, **15**, 491-497.
74. J. Lee, Y. Xu and G. W. Huber, High-Throughput Screening of Monometallic Catalysts for Aqueous-Phase Hydrogenation of Biomass-Derived Oxygenates, *Applied Catalysis B: Environmental*, 2013, **140–141**, 98-107.
75. J. Lee, Y. T. Kim and G. W. Huber, Aqueous-Phase Hydrogenation and Hydrodeoxygenation of Biomass-Derived Oxygenates with Bimetallic Catalysts, *Green Chemistry*, 2014, **16**, 708-718.
76. S. K. Green, J. Lee, H. J. Kim, G. A. Tompsett, W. B. Kim and G. W. Huber, The Electrocatalytic Hydrogenation of Furanic Compounds in a Continuous Electrocatalytic Membrane Reactor, *Green Chemistry*, 2013, **15**, 1869-1879.
77. H. J. Kim, S. K. Green, J. Lee and G. W. Huber, Electrocatalytic Oxidation and Reduction of Biomass-Derived Oxygenates in a Continuous-Flow PEM Reactor, 23rd North American Catalysis Society Meeting, Louisville, KY, 2013.
78. H. J. Kim, J. Lee, S. K. Green, G. W. Huber and W. B. Kim, Selective Glycerol Oxidation by Electrocatalytic Dehydrogenation, *ChemSusChem*, 2014, **7**, 1051-1056.
79. X. Wang, N. Perret and M. A. Keane, The Role of Hydrogen Partial Pressure in the Gas Phase Hydrogenation of *p*-Chloronitrobenzene over Alumina Supported Au and Pd: A Consideration of Reaction Thermodynamics and Kinetics, *Chemical Engineering Journal*, 2012, **210**, 103-113.
80. T. K. Das, W. A. Conner, J. L. Li, G. Jacobs, M. E. Dry and B. H. Davis, Fischer-Tropsch Synthesis: Kinetics and Effect of Water for a Co/SiO_2 Catalyst, *Energy & Fuels*, 2005, **19**, 1430-1439.
81. G. Ertl, H. Knözinger, F. Schüth and J. Weiktamp (Eds.), 2nd ed., *Handbook of Heterogeneous Catalysis*, Wiley-VCH, Weinheim, 2008.
82. J. Wisniak, M. Hershkowitz and S. Stein, Hydrogenation of Xylose over Platinum Group Catalysts, *Industrial & Engineering Chemistry Product Research and Development*, 1974, **13**, 232-236.

83. J. Wisniak, Hershkow.M, Leibowit.R and S. Stein, Hydrogenation of Xylose to Xylitol, *Industrial & Engineering Chemistry Product Research and Development*, 1974, **13**, 75-79.
84. M. Yadav, D. K. Mishra and J.-S. Hwang, Catalytic Hydrogenation of Xylose to Xylitol using Ruthenium Catalyst on NiO Modified TiO_2 Support, *Applied Catalysis A: General*, 2012, **425–426**, 110-116.
85. G. M. R. van Druten and V. Ponec, Hydrogenation of Carbonylic Compounds Part I: Competitive Hydrogenation of Propanal and Acetone over Noble Metal Catalysts, *Applied Catalysis A: General*, 2000, **191**, 153-162.
86. R. Y. Zheng, Y. X. Zhu and J. G. G. Chen, Promoting Low-Temperature Hydrogenation of C=O Bonds of Acetone and Acetaldehyde by using Co-Pt Bimetallic Catalysts, *ChemCatChem*, 2011, **3**, 578-581.
87. L. E. Murillo, A. M. Goda and J. G. Chen, Selective Hydrogenation of the C=O Bond in Acrolein through the Architecture of Bimetallic Surface Structures, *Journal of the American Chemical Society*, 2007, **129**, 7101-7105.
88. D. E. Resasco, S. Sitthisa, J. Faria, T. Prasomsri and M. P. Ruiz, Furfurals as Chemical Platform for Biofuels Production, *Heterogeneous Catalysis in Biomass to Chemicals and Fuels*, Research Signpost, Trivandrum, Kerala, 2011, Ch. 5, pp. 155-188.
89. W. J. Yu, Y. Tang, L. Y. Mo, P. Chen, H. Lou and X. M. Zheng, One-Step Hydrogenation-Esterification of Furfural and Acetic Acid over Bifunctional Pd Catalysts for Bio-Oil Upgrading, *Bioresource Technology*, 2011, **102**, 8241-8246.
90. B. Liu, L. Cheng, L. Curtiss and J. Greeley, Effects of van der Waals Density Functional Corrections on Trends in Furfural Adsorption and Hydrogenation on Close-Packed Transition Metal Surfaces, *Surface Science*, 2014, **622**, 51-59.
91. S. Sitthisa and D. E. Resasco, Hydrodeoxygenation of Furfural Over Supported Metal Catalysts: A Comparative Study of Cu, Pd and Ni, *Catalysis Letters*, 2011, **141**, 784-791.
92. E. P. Maris and R. J. Davis, Hydrogenolysis of Glycerol over Carbon-Supported Ru and Pt Catalysts, *Journal of Catalysis*, 2007, **249**, 328-337.
93. J. Y. Sun and H. C. Liu, Selective Hydrogenolysis of Biomass-Derived Xylitol to Ethylene Glycol and Propylene Glycol on Supported Ru Catalysts, *Green Chemistry*, 2011, **13**, 135-142.
94. R. L. Augustine, The Stereochemistry of Hydrogenation of α,β-Unsaturated Ketones, *Advances in Catalysis*, Academic Press, 1976, vol. 25, pp. 56-80.
95. S. Nishimura, *Handbook of Heterogeneous Catalytic Hydrogenation for Organic Synthesis*, John Wiley & Sons, Inc., New York, NY, 2001.
96. G. F. Santori, M. L. Casella and O. A. Ferretti, Hydrogenation of Carbonyl Compounds using Tin-Modified Platinum-Based Catalysts Prepared via Surface Organometallic Chemistry on Metals (SOMC/M), *Journal of Molecular Catalysis A: Chemical*, 2002, **186**, 223-239.
97. P. Claus, Selective Hydrogenation of α,β-Unsaturated Aldehydes and Other C=O and C=C Bonds Containing Compounds, *Topics in Catalysis*, 1998, **5**, 51-62.
98. P. Mäki-Arvela, J. Hájek, T. Salmi and D. Y. Murzin, Chemoselective Hydrogenation of Carbonyl Compounds over Heterogeneous Catalysts, *Applied Catalysis A: General*, 2005, **292**, 1-49.
99. X. L. Zhu, L. L. Lobban, R. G. Mallinson and D. E. Resasco, Tailoring the Mesopore Structure of HZSM-5 to Control Product Distribution in the Conversion of Propanal, *Journal of Catalysis*, 2010, **271**, 88-98.

100. D. M. Alonso, S. G. Wettstein and J. A. Dumesic, Bimetallic Catalysts for Upgrading of Biomass to Fuels and Chemicals, *Chemical Society Reviews*, 2012, **41**, 8075-8098.
101. R. Y. Zheng, M. P. Humbert, Y. X. Zhu and J. G. Chen, Low-Temperature Hydrogenation of the C=O bond of Propanal over Ni-Pt Bimetallic Catalysts: From Model Surfaces to Supported Catalysts, *Catalysis Science & Technology*, 2011, **1**, 638-643.
102. Y. Nakagawa and K. Tomishige, Total Hydrogenation of Furan Derivatives over Silica-Supported Ni-Pd Alloy Catalyst, *Catalysis Communications*, 2010, **12**, 154-156.
103. J. C. Bertolini, B. Tardy, M. Abon, J. Billy, P. Delichere and J. Massardier, Surface Reactivity of Platinum-Nickel Single Crystal Alloys: Carbon Monoxide Adsorption, *Surface Science*, 1983, **135**, 117-127.
104. H. Igarashi, T. Fujino, Y. M. Zhu, H. Uchida and M. Watanabe, CO Tolerance of Pt Alloy Electrocatalysts for Polymer Electrolyte Fuel Cells and the Detoxification Mechanism, *Physical Chemistry Chemical Physics*, 2001, **3**, 306-314.
105. E. Christoffersen, P. Liu, A. Ruban, H. L. Skriver and J. K. Norskov, Anode Materials for Low-Temperature Fuel Cells: A Density Functional Theory Study, *Journal of Catalysis*, 2001, **199**, 123-131.
106. J. Greeley and M. Mavrikakis, Alloy Catalysts Designed from First Principles, *Nature Materials*, 2004, **3**, 810-815.
107. S. Sitthisa, T. Pham, T. Prasomsri, T. Sooknoi, R. G. Mallinson and D. E. Resasco, Conversion of Furfural and 2-Methylpentanal on Pd/SiO_2 and $Pd-Cu/SiO_2$ Catalysts, *Journal of Catalysis*, 2011, **280**, 17-27.
108. S. Sitthisa, W. An and D. E. Resasco, Selective Conversion of Furfural to Methylfuran over Silica-Supported Ni-Fe Bimetallic Catalysts, *Journal of Catalysis*, 2011, **284**, 90-101.
109. P. T. M. Do, A. J. Foster, J. G. Chen and R. F. Lobo, Bimetallic Effects in the Hydrodeoxygenation of *meta*-Cresol on γ-Al_2O_3 Supported Pt-Ni and Pt-Co Catalysts, *Green Chemistry*, 2012, **14**, 1388-1397.
110. F. A. Lewis, The Hydrides of Palladium and Palladium Alloys, *Platinum Metals Review*, 1960, **4**, 132-137.
111. F. D. Manchester, A. San-Martin and J. M. Pitre, The H-Pd (hydrogen-palladium) System, *Journal of Phase Equilibria*, 1994, **15**, 62-83.
112. G. Fagherazzi, A. Benedetti, S. Polizzi, A. Dimario, F. Pinna and M. Signoretto, Structural Investigation on the Stoichiometry of β-PdH_x in Pd/SiO_2 Catalysts as a Function of Metal Dispersion, *Catalysis Letters*, 1995, **32**, 293-303.
113. A. Sarkany, Z. Zsoldos, G. Stefler, J. W. Hightower and L. Guczi, Promoter Effect of Pd in Hydrogenation of 1,3-Butadiene over Co-Pd Catalysts, *Journal of Catalysis*, 1995, **157**, 179-189.
114. N. S. Babu, N. Lingaiah and P. S. S. Prasad, Characterization and Reactivity of Al_2O_3 Supported Pd-Ni Bimetallic Catalysts for Hydrodechlorination of Chlorobenzene, *Applied Catalysis B: Environmental*, 2012, **111**, 309-316.
115. M. H. Shao, P. Liu, J. L. Zhang and R. Adzic, Origin of Enhanced Activity in Palladium Alloy Electrocatalysts for Oxygen Reduction Reaction, *The Journal of Physical Chemistry B*, 2007, **111**, 6772-6775.
116. J. Greeley and M. Mavrikakis, Surface and Subsurface Hydrogen: Adsorption Properties on Transition Metals and Near-Surface Alloys, *The Journal of Physical Chemistry B*, 2005, **109**, 3460-3471.

117. M. J. Maccarrone, C. Lederhos, C. Betti, G. C. Torres, J. M. Badano, M. Quiroga and J. Yori, Kinetic Study of the Partial Hydrogenation of 1-Heptyne over Ni and Pd Supported on Alumina, *Hydrogenation*, InTech, 2012, Ch. 7, pp. 159-184.
118. A. Guerrero-Ruiz, A. Sepúlveda-Escribano and I. Rodríguez-Ramos, Carbon Supported Bimetallic Catalysts Containing Iron: I. Preparation and Characterization, *Applied Catalysis A: General*, 1992, **81**, 81-100.
119. R. Burch and M. J. Hayes, The Preparation and Characterisation of Fe-Promoted Al2O3-Supported Rh Catalysts for the Selective Production of Ethanol from Syngas, *Journal of Catalysis*, 1997, **165**, 249-261.
120. A. J. R. Hensley, Y. Hong, R. Zhang, H. Zhang, J. Sun, Y. Wang and J.-S. McEwen, Enhanced Fe_2O_3 Reducibility via Surface Modification with Pd: Characterizing the Synergy within Pd/Fe Catalysts for Hydrodeoxygenation Reactions, *ACS Catalysis*, 2014, **4**, 3381-3392.
121. L. Guczi, Structure and Catalytic Properties of Iron-Containing Bimetallic Catalysts, *Catalysis Reviews: Science and Engineering*, 1981, **23**, 329-376.
122. D. Richard, J. Ockelford, A. Giroirfendler and P. Gallezot, Composition and Catalytic Properties in Cinnamaldehyde Hydrogenation of Charcoal-Supported Platinum Catalysts Modified by $FeCl_2$ Additives, *Catalysis Letters*, 1989, **3**, 53-58.
123. F. J. Berry, C. H. Xu and S. Jobson, Titania-Supported Iron-Ruthenium and Iron-Iridium Catalysts - An *in situ* Iron-57 Mössbauer Spectroscopic Study of the Effects of Pretreatment in Hydrogen, *Journal of the Chemical Society, Faraday Transactions*, 1990, **86**, 165-169.
124. J. Xu, C. H. Bartholomew, J. Sudweeks and D. L. Eggett, Design, Synthesis, and Catalytic Properties of Silica-Supported, Pt-Promoted Iron Fischer-Tropsch Catalysts, *Topics in Catalysis*, 2003, **26**, 55-71.
125. B. D. Li, J. Wang, Y. Z. Yuan, H. Ariga, S. Takakusagi and K. Asakura, Carbon Nanotube-Supported RuFe Bimetallic Nanoparticles as Efficient and Robust Catalysts for Aqueous-Phase Selective Hydrogenolysis of Glycerol to Glycols, *ACS Catalysis*, 2011, **1**, 1521-1528.
126. M. Mavrikakis and M. A. Barteau, Oxygenate Reaction Pathways on Transition Metal Surfaces, *Journal of Molecular Catalysis A: Chemical*, 1998, **131**, 135-147.
127. R. Alcala, J. Greeley, M. Mavrikakis and J. A. Dumesic, Density-Functional Theory Studies of Acetone and Propanal Hydrogenation on Pt(111), *Journal of Chemical Physics*, 2002, **116**, 8973-8980.
128. G. M. R. van Druten and V. Ponec, Hydrogenation of Carbonylic Compounds Part II: The Influence of Alcohols on the Hydrogenation of Carbonyl Compounds, *Applied Catalysis A: General*, 2000, **191**, 163-176.
129. S. Sitthisa, T. Sooknoi, Y. G. Ma, P. B. Balbuena and D. E. Resasco, Kinetics and Mechanism of Hydrogenation of Furfural on Cu/SiO_2 Catalysts, *Journal of Catalysis*, 2011, **277**, 1-13.
130. R. Weingarten, G. A. Tompsett, W. C. Conner and G. W. Huber, Design of Solid Acid Catalysts for Aqueous-Phase Dehydration of Carbohydrates: The Role of Lewis and Brønsted Acid Sites, *Journal of Catalysis*, 2011, **279**, 174-182.
131. R. Weingarten, Y. T. Kim, G. A. Tompsett, A. Fernández, K. S. Han, E. W. Hagaman, W. C. Conner Jr, J. A. Dumesic and G. W. Huber, Conversion of Glucose into Levulinic Acid with Solid Metal(IV) Phosphate Catalysts, *Journal of Catalysis*, 2013, **304**, 123-134.

132. F. Delbecq and P. Sautet, Competitive C=C and C=O Adsorption of α,β-Unsaturated Aldehydes on Pt and Pd Surfaces in Relation with the selectivity of Hydrogenation Reactions: A Theoretical Approach, *Journal of Catalysis*, 1995, **152**, 217-236.
133. M. Burgener, R. Wirz, T. Mallat and A. Baiker, Nature of Catalyst Deactivation during Citral Hydrogenation: A Catalytic and ATR-IR Study, *Journal of Catalysis*, 2004, **228**, 152-161.
134. A. J. R. Hensley, R. Zhang, Y. Wang and J.-S. McEwen, Tailoring the Adsorption of Benzene on PdFe Surfaces: A Density Functional Theory Study, *The Journal of Physical Chemistry C*, 2013, **117**, 24317-24328.
135. J. Nørskov, T. Bligaard, A. Logadottir, S. Bahn, L. B. Hansen, M. Bollinger, H. Bengaard, B. Hammer, Z. Sljivancanin, M. Mavrikakis, Y. Xu, S. Dahl and C. J. H. Jacobsen, Universality in Heterogeneous Catalysis, *Journal of Catalysis*, 2002, **209**, 275-278.
136. S. Wang, V. Petzold, V. Tripkovic, J. Kleis, J. G. Howalt, E. Skúlason, E. M. Fernández, B. Hvolbæk, G. Jones, A. Toftelund, H. Falsig, M. Björketun, F. Studt, F. Abild-Pedersen, J. Rossmeisl, J. K. Nørskov and T. Bligaard, Universal Transition State Scaling Relations for (de)hydrogenation over Transition Metals, *Physical Chemistry Chemical Physics*, 2011, **13**, 20760-20765.
137. R. M. West, Z. Y. Liu, M. Peter and J. A. Dumesic, Liquid Alkanes with targeted molecular weights from biomass-derived carbohydrates, *ChemSusChem*, 2008, **1**, 417-424.
138. L. Nie, P. M. de Souza, F. B. Noronha, W. An, T. Sooknoi and D. E. Resasco, Selective Conversion of m-Cresol to Toluene over Bimetallic Ni-Fe Catalysts, *Journal of Molecular Catalysis A: Chemical*, 2014, **388–389**, 47-55.
139. A. Yamaguchi, N. Hiyoshi, O. Sato and M. Shirai, Sorbitol Dehydration in High Temperature Liquid Water, *Green Chemistry*, 2011, **13**, 873-881.
140. F. Jin and H. Enomoto, Rapid and Highly Selective Conversion of Biomass into Value-Added Products in Hydrothermal Conditions: Chemistry of Acid/Base-Catalysed and Oxidation Reactions, *Energy & Environmental Science*, 2011, **4**, 382-397.
141. R. M. Bullock (Ed.), *Catalysis without Precious Metals*, Wiley-VCH, Weinheim, 2010.
142. I. W. C. E. Arends and R. A. Sheldon, Activities and Stabilities of Heterogeneous Catalysts in Selective Liquid Phase Oxidations: Recent Developments, *Applied Catalysis A: General*, 2001, **212**, 175-187.
143. M. Besson and P. Gallezot, Deactivation of Metal Catalysts in Liquid Phase Organic Reactions, *Catalysis Today*, 2003, **81**, 547-559.
144. J. L. Lu, B. S. Fu, M. C. Kung, G. M. Xiao, J. W. Elam, H. H. Kung and P. C. Stair, Coking- and Sintering-Resistant Palladium Catalysts Achieved Through Atomic Layer Deposition, *Science*, 2012, **335**, 1205-1208.
145. B. J. O'Neill, D. H. K. Jackson, A. J. Crisci, C. A. Farberow, F. Shi, A. C. Alba-Rubio, J. Lu, P. J. Dietrich, X. Gu, C. L. Marshall, P. C. Stair, J. W. Elam, J. T. Miller, F. H. Ribeiro, P. M. Voyles, J. Greeley, M. Mavrikakis, S. L. Scott, T. F. Kuech and J. A. Dumesic, Stabilization of Copper Catalysts for Liquid-Phase Reactions by Atomic Layer Deposition, *Angewandte Chemie International Edition*, 2013, **52**, 13808-13812.
146. P. J. van Berge, J. van de Loosdrecht, S. Barradas and A. M. van der Kraan, Oxidation of Cobalt Based Fischer-Tropsch Catalysts as a Deactivation Mechanism, *Catalysis Today*, 2000, **58**, 321-334.

147. W. Chu, P. A. Chernavskii, L. Gengembre, G. A. Pankina, P. Fongarland and A. Y. Khodakov, Cobalt Species in Promoted Cobalt Alumina-Supported Fischer-Tropsch Catalysts, *Journal of Catalysis*, 2007, **252**, 215-230.
148. P. H. Bolt, F. Habraken and J. W. Geus, Formation of Nickel, Cobalt, Copper, and Iron Aluminates from α- and γ-Alumina-Supported Oxides: A Comparative Study, *Journal of Solid State Chemistry*, 1998, **135**, 59-69.
149. M. Ritala, M. Leskela, E. Nykanen, P. Soininen and L. Niinisto, Growth of Titanium Dioxide Thin Films by Atomic Layer Epitaxy, *Thin Solid Films*, 1993, **225**, 288-295.
150. J. Greeley, Structural effects on trends in the deposition and dissolution of metal-supported metal adstructures, *Electrochimica Acta*, 2010, **55**, 5545-5550.
151. C. Xiao, R. V. Maligal-Ganesh, T. Li, Z. Qi, Z. Guo, K. T. Brashler, S. Goes, X. Li, T. W. Goh, R. E. Winans and W. Huang, High-Temperature-Stable and Regenerable Catalysts: Platinum Nanoparticles in Aligned Mesoporous Silica Wells, *ChemSusChem*, 2013, **6**, 1915-1922.
152. J. Ilavsky and P. R. Jemian, Irena: Tool Suite for Modeling and Analysis of Small-Angle Scattering, *Journal of Applied Crystallography*, 2009, **42**, 347-353.
153. W. D. Kim, G. W. Hwang, O. S. Kwon, S. K. Kim, M. Cho, D. S. Jeong, S. W. Lee, M. H. Seo, C. S. Hwang, Y. S. Min and Y. J. Cho, Growth Characteristics of Atomic Layer Deposited TiO_2 Thin Films on Ru and Si Electrodes for Memory Capacitor Applications, *Journal of the Electrochemical Society*, 2005, **152**, C552-C559.
154. J. P. Lange, E. van der Heide, J. van Buijtenen and R. Price, Furfural - A Promising Platform for Lignocellulosic Biofuels, *ChemSusChem*, 2012, **5**, 150-166.
155. Y. Nakagawa, M. Tamura and K. Tomishige, Catalytic Reduction of Biomass-Derived Furanic Compounds with Hydrogen, *ACS Catalysis*, 2013, **3**, 2655-2668.
156. M. A. Tike and V. V. Mahajani, Kinetics of Liquid-Phase Hydrogenation of Furfuryl Alcohol to Tetrahydrofurfuryl Alcohol over a Ru/TiO_2 Catalyst, *Industrial & Engineering Chemistry Research*, 2007, **46**, 3275-3282.
157. B. Zhang, Y. Zhu, G. Ding, H. Zheng and Y. Li, Selective Conversion of Furfuryl Alcohol to 1,2-Pentanediol over a Ru/MnO_x Catalyst in Aqueous Phase, *Green Chemistry*, 2012, **14**, 3402-3409.
158. M. Chia, Y. J. Pagán-Torres, D. Hibbitts, Q. Tan, H. N. Pham, A. K. Datye, M. Neurock, R. J. Davis and J. A. Dumesic, Selective Hydrogenolysis of Polyols and Cyclic Ethers over Bifunctional Surface Sites on Rhodium–Rhenium Catalysts, *Journal of the American Chemical Society*, 2011, **133**, 12675-12689.
159. W. J. Xu, H. F. Wang, X. H. Liu, J. W. Ren, Y. Q. Wang and G. Z. Lu, Direct Catalytic Conversion of Furfural to 1,5-Pentanediol by Hydrogenolysis of the Furan Ring under Mild Conditions over Pt/Co_2AlO_4 Catalyst, *Chemical Communications*, 2011, **47**, 3924-3926.
160. M. Hronec, K. Fulajtarova and T. Liptaj, Effect of Catalyst and Solvent on the Furan Ring Rearrangement to Cyclopentanone, *Applied Catalysis A: General*, 2012, **437**, 104-111.
161. Y. L. Yang, Z. T. Du, Y. Z. Huang, F. Lu, F. Wang, J. Gao and J. Xu, Conversion of Furfural into Cyclopentanone over Ni-Cu Bimetallic Catalysts, *Green Chemistry*, 2013, **15**, 1932-1940.
162. J. Q. Bond, A. A. Upadhye, H. Olcay, G. A. Tompsett, J. Jae, R. Xing, D. M. Alonso, D. Wang, T. Zhang, R. Kumar, A. Foster, S. M. Sen, C. T. Maravelias, R. Malina, S. R. H. Barrett, R. Lobo, C. E. Wyman, J. A. Dumesic and G. W. Huber, Production of Renewable

Jet Fuel Range Alkanes and Commodity Chemicals from Integrated Catalytic Processing of Biomass, *Energy & Environmental Science*, 2014, **7**, 1500-1523.
163. D. C. Elliott, T. R. Hart, G. G. Neuenschwander, L. J. Rotness, M. V. Olarte, A. H. Zacher and Y. Solantausta, Catalytic Hydroprocessing of Fast Pyrolysis Bio-oil from Pine Sawdust, *Energy & Fuels*, 2012, **26**, 3891-3896.
164. D. C. Elliott, G. G. Neuenschwander and T. R. Hart, Hydroprocessing Bio-Oil and Products Separation for Coke Production, *ACS Sustainable Chemistry & Engineering*, 2013, **1**, 389-392.
165. J.-P. Mikkola, H. Vainio, T. Salmi, R. Sjöholm, T. Ollonqvist and J. Väyrynen, Deactivation Kinetics of Mo-Supported Raney Ni catalyst in the Hydrogenation of Xylose to Xylitol, *Applied Catalysis A: General*, 2000, **196**, 143-155.
166. N. Ji, T. Zhang, M. Y. Zheng, A. Q. Wang, H. Wang, X. D. Wang and J. G. G. Chen, Direct Catalytic Conversion of Cellulose into Ethylene Glycol Using Nickel-Promoted Tungsten Carbide Catalysts, *Angewandte Chemie International Edition*, 2008, **47**, 8510-8513.
167. J. He, C. Zhao and J. A. Lercher, Ni-Catalyzed Cleavage of Aryl Ethers in the Aqueous Phase, *Journal of the American Chemical Society*, 2012, **134**, 20768-20775.
168. X. Y. Wang and R. Rinaldi, Exploiting H-Transfer Reactions with RANEY$^{(R)}$ Ni for Upgrade of Phenolic and Aromatic Biorefinery Feeds under Unusual, Low-Severity Conditions, *Energy & Environmental Science*, 2012, **5**, 8244-8260.
169. P. Ferrini and R. Rinaldi, Catalytic Biorefining of Plant Biomass to Non-Pyrolytic Lignin Bio-Oil and Carbohydrates through Hydrogen Transfer Reactions, *Angewandte Chemie International Edition*, 2014, **53**, 8634-8639.
170. J.-P. Mikkola, R. Sjöholm, T. Salmi and P. Mäki-Arvela, Xylose Hydrogenation: Kinetic and NMR Studies of the Reaction Mechanisms, *Catalysis Today*, 1999, **48**, 73-81.
171. J. Lee, D. H. K. Jackson, T. Li, R. E. Winans, J. A. Dumesic, T. F. Kuech and G. W. Huber, Enhanced Stability of Cobalt Catalysts by Atomic Layer Deposition for Aqueous-Phase Reactions, *Energy & Environmental Science*, 2014, **7**, 1657-1660.
172. S. J. Tauster, S. C. Fung and R. L. Garten, Strong Metal-Support Interactions. Group 8 Noble Metals Supported on Titanium Dioxide, *Journal of the American Chemical Society*, 1978, **100**, 170-175.
173. J. Santos, J. Phillips and J. A. Dumesic, Metal Support Interactions between Iron and Titania for Catalysts Prepared by Thermal-Decomposition of Iron Pentacarbonyl and by Impregnation, *Journal of Catalysis*, 1983, **81**, 147-167.
174. D. E. Resasco and G. L. Haller, A Model of Metal-Oxide Support Interaction for Rh on TiO_2, *Journal of Catalysis*, 1983, **82**, 279-288.
175. S. J. Tauster, Strong Metal-Support Interactions, *Accounts of Chemical Research*, 1987, **20**, 389-394.
176. S. A. Stevenson, J. A. Dumesic, R. T. K. Baker and E. Ruckenstein (Eds.), *Metal-Support Interactions in Catalysis, Sintering, and Redispersion*, Van Nostrand Reinhold, New York, 1987.
177. J. A. Dumesic, S. A. Stevenson, R. D. Sherwood and R. T. K. Baker, Migration of Nickel and Titanium-Oxide Species as Studied by *in situ* Scanning-Transmission Electron-Microscopy, *Journal of Catalysis*, 1986, **99**, 79-87.
178. S. Zander, E. L. Kunkes, M. E. Schuster, J. Schumann, G. Weinberg, D. Teschner, N. Jacobsen, R. Schlögl and M. Behrens, The Role of the Oxide Component in the

Development of Copper Composite Catalysts for Methanol Synthesis, *Angewandte Chemie International Edition*, 2013, **52**, 6536-6540.

179. R. Naumann d'Alnoncourt, M. Friedrich, E. Kunkes, D. Rosenthal, F. Girgsdies, B. Zhang, L. Shao, M. Schuster, M. Behrens and R. Schlögl, Strong Metal–Support Interactions between Palladium and Iron Oxide and Their Effect on CO Oxidation, *Journal of Catalysis*, 2014, **317**, 220-228.
180. A. Bruix, J. A. Rodriguez, P. J. Ramírez, S. D. Senanayake, J. Evans, J. B. Park, D. Stacchiola, P. Liu, J. Hrbek and F. Illas, A New Type of Strong Metal–Support Interaction and the Production of H_2 through the Transformation of Water on $Pt/CeO_2(111)$ and $Pt/CeO_x/TiO_2(110)$ Catalysts, *Journal of the American Chemical Society*, 2012, **134**, 8968-8974.
181. L. R. Baker, G. Kennedy, M. Van Spronsen, A. Hervier, X. Cai, S. Chen, L.-W. Wang and G. A. Somorjai, Furfuraldehyde Hydrogenation on Titanium Oxide-Supported Platinum Nanoparticles Studied by Sum Frequency Generation Vibrational Spectroscopy: Acid–Base Catalysis Explains the Molecular Origin of Strong Metal–Support Interactions, *Journal of the American Chemical Society*, 2012, **134**, 14208-14216.
182. G. Melaet, W. T. Ralston, C.-S. Li, S. Alayoglu, K. An, N. Musselwhite, B. Kalkan and G. A. Somorjai, Evidence of Highly Active Cobalt Oxide Catalyst for the Fischer–Tropsch Synthesis and CO_2 Hydrogenation, *Journal of the American Chemical Society*, 2014, **136**, 2260-2263.
183. V. A. de la Peña O'Shea, M. Consuelo Álvarez Galván, A. E. Platero Prats, J. M. Campos-Martin and J. L. G. Fierro, Direct Evidence of the SMSI Decoration Effect: The Case of Co/TiO_2 Catalyst, *Chemical Communications*, 2011, **47**, 7131-7133.
184. C. H. Bartholomew, Mechanisms of Catalyst Deactivation, *Applied Catalysis A: General*, 2001, **212**, 17-60.
185. K. Suriye, P. Praserthdam and B. Jongsomjit, Impact of Ti^{3+} Present in Titania on Characteristics and Catalytic Properties of the Co/TiO_2 Catalyst, *Industrial & Engineering Chemistry Research*, 2005, **44**, 6599-6604.
186. J. Yan, G. Wu, N. Guan, L. Li, Z. Li and X. Cao, Understanding the Effect of Surface/Bulk Defects on the Photocatalytic Activity of TiO_2: Anatase versus Rutile, *Physical Chemistry Chemical Physics*, 2013, **15**, 10978-10988.
187. J. Jiang and L. Li, Synthesis of Sphere-Like Co_3O_4 Nanocrystals via a Simple Polyol Route, *Materials Letters*, 2007, **61**, 4894-4896.
188. P. D. Vaidya and V. V. Mahajani, Kinetics of Liquid-Phase Hydrogenation of Furfuraldehyde to Furfuryl Alcohol over a Pt/C Catalyst, *Industrial & Engineering Chemistry Research*, 2003, **42**, 3881-3885.
189. M. Schlaf, Selective Deoxygenation of Sugar Polyols to α,ω-Diols and Other Oxygen Content Reduced Materials - A New Challenge to Homogeneous Ionic Hydrogenation and Hydrogenolysis Catalysis, *Dalton Transactions*, 2006, 4645-4653.
190. Y. Nakagawa and K. Tomishige, Production of 1,5-Pentanediol from Biomass via Furfural and Tetrahydrofurfuryl Alcohol, *Catalysis Today*, 2012, **195**, 136-143.
191. S. Liu, Y. Amada, M. Tamura, Y. Nakagawa and K. Tomishige, One-Pot Selective Conversion of Furfural into 1,5-Pentanediol over a Pd-Added $Ir-ReO_x/SiO_2$ Bifunctional Catalyst, *Green Chemistry*, 2014, **16**, 617-626.

192. S. Liu, Y. Amada, M. Tamura, Y. Nakagawa and K. Tomishige, Performance and Characterization of Rhenium-Modified Rh-Ir Alloy Catalyst for One-Pot Conversion of Furfural into 1,5-Pentanediol, *Catalysis Science & Technology*, 2014, **4**, 2535-2549.
193. S. J. Tauster and S. C. Fung, Strong Metal-Support Interactions: Occurrence among the Binary Oxides of Group IIA-VB, *Journal of Catalysis*, 1978, **55**, 29-35.